Mid-infrared absorption sensor for CO concentration and temperature measurements for pyrolysis and oxidation behind reflected shock waves

Von der Fakultät für Ingenieurwissenschaften,

Abteilung Maschinenbau und Verfahrenstechnik

der

Universität Duisburg-Essen

zur Erlangung des akademischen Grades

eines

Doktors der Ingenieurswissenschaften

Dr.-Ing.

genehmigte Dissertation

von

Bo Shu

aus

Jiangsu, V. R. China

Gutachter: Prof. Dr. Christof Schulz

Prof. Dr. Ravi Fernandes

Tag der mündlichen Prüfung: 15.03.2018

Table of Contents

Abstract

Due to the increasing energy demand and the related environmental issues, combustion efficiency and reduction of pollutants emission have become a major concern for combustion applications. In combustion, pollutant formation and fuel ignition are controlled by chemical kinetics, therefore, the design and optimization of combustion systems heavily relies on an accurate understanding of the underlying chemical processes. While combustion processes are governed by an interaction of chemical kinetics and transport processes, for gaining fundamental understanding it is beneficial to separate both processes. To this end, shock tubes are frequently applied to generate a uniform gas phase environment for a wide range of temperatures and pressures that is suited for initiating reactions with subsequent time-resolved detection. The combination of shock tube technique and laser absorption spectroscopy provides the platform for accurate chemical kinetic studies. Infrared laser absorption diagnostics have been widely applied in combustion research for example for *in situ*, fast, and sensitive measurements of temperature, pressure, and species concentrations.

In the present study, laser absorption spectroscopy of carbon monoxide (CO) near 4.7 µm has been developed for the sensing of temperature and CO concentration behind the reflected shock wave. The sensor was further developed to enable fiber-based thermometry for more flexible applications in harsh environments. The oxidation of fuel-rich CH_4/O_2 mixtures, the thermal decomposition of anisole ($C_6H_5OCH_3$), and the pyrolysis of acetylene (C_2H_2) and benzene (C_6H_6) were investigated by monitoring the CO concentration and temperature based on two-line absorption thermometry. The experimental data were applied for validation of reaction mechanisms covering different kinetics conditions such as single elementary reaction, partial oxidation, and soot formation.

The oxidation of fuel-rich CH_4/O_2 mixtures was investigated to validate reaction mechanisms for reaction conditions that are important for polygeneration processes where partial oxidation allows to convert natural gas to higher-value chemicals. With the presences of dimethyl ether (DME) and *n*-heptane, the initial reaction temperature is significantly reduced because they promote the production of additional OH radicals.

Anisole has recently been identified as fluorescence tracer for fuel/air mixing studies, but its decomposition kinetics were not yet fully understood. In the investigation of thermal decomposition of anisole at elevated temperatures, the literature model was found to strongly underesti-

mate the CO formation. As main reaction path for CO formation, the unimolecular decomposition of phenoxy radical (C_6H_5O) was investigated independently and new rate constants were determined.

Soot formation from combustion is of high scientific interest. The temperature dependence as well as the influence of H_2, O_2, and CH_4 on soot formation in the pyrolysis of C_2H_2 and C_6H_6 were investigated. The temperature dependence of the soot yield and the particle formation induction time were found to be in a good agreement with literature data. The presence of H_2 led to a depletion of the particle formation in both systems whereas the opposite trend yield was observed in the presence of CH_4 and O_2.

Kurzfassung

Aufgrund des steigenden Energiebedarfs durch die industrielle Entwicklung ist der Schutz der Atmosphäre die wichtigste Aufgabe unserer Zeit. Das Interesse in modernen, umwelt-freundlichen Verbrennungssystemen hat zu Verbesserung der Verbrennungseffizienz und zur Verringerung der Schadstoffemissionen geführt. Das Design und die Optimierung von Verbrennungssystemen beruht auf einer genauen Modellierung elementarer, chemischer Prozesse.

Infrarot-Laserabsorptionsdiagnostik ist eine hochentwickelte Diagnostik in der Verbrennungsforschung für schnelle, hochsensitive *in-situ* Messungen von Temperatur, Druck, und Spezieskonzentrationen. Stoßwellenrohre sind einfache und robuste Instrumente, die eine homogene Gasphasenumgebung in einem großen Temperatur- und Druckbereich erzeugen. Die Kombination aus Stoßwellentechnik und Laserabsorptionsspektroskopie bietet eine Plattform für akkurate, chemische kinetische Untersuchungen.

In der vorliegenden Arbeit wurde die Laserabsorptionsspektroskopie von Kohlenmonoxid (CO) nahe 4.7 µm für die Erfassung von Temperatur und CO-Konzentration hinter den reflektierten Stoßwellen entwickelt. Des Weiteren wurde der Sensor als faserbasiertes Thermometer für flexible und robuste Anwendungen weiterentwickelt. Die Oxidation von fetten Methan (CH_4)/Sauerstoff (O_2) Gemischen, der thermische Zerfall von Anisol ($C_6H_5OCH_3$) sowie die Pyrolyse von Acetylen (C_2H_2) und Benzol (C_6H_6) wurden in der Gasphase im Stoßwellenrohr in Kombination mit der CO-Thermometrie untersucht.

Die experimentellen Daten wurden mit Simulationen auf der Basis ausgewählter Reaktionsmechanismen verglichen. Bei der Oxidation von fetten CH_4/O_2 Mischungen senkten die Additive Dimethylether (DME) und n-Heptan die anfängliche Reaktionstemperatur signifikant, indem sie zusätzliche OH-Radikale erzeugen. Keiner der Mechanismen ist für chemische Umwandlungsreaktionen optimiert. Die CO-Bildung wird beim thermischen Zerfall von Anisol nur schlecht vom Modell wiedergegeben. Die Reaktionsgeschwindigkeit des unimolekularen Zerfalls des Phenoxyradikals (C_6H_5O) wurde experimentell bestimmt.

Bei der Pyrolyse von C_2H_2 und C_6H_6 wurde die Temperaturabhängigkeit der Rußbildung und deren Induktionszeit mittels Laserlicht-Extinktion gemessen und eine gute Übereinstimmung mit der Literatur gefunden. Die Anwesenheit von Wasserstoff (H_2) führte zu einer Reduktion der Partikelbildung in beiden Systemen, wohingegen ein entgegengesetztes Verhalten bei der Rußbildung in Anwesenheit von CH_4 und O_2 bei C_2H_2 und C_6H_6 beobachtet wurde.

Symbols and abbreviations

A	Pre-exponential factor
a	Coefficient of polynomial expression
a	Voigt parameter
a	Absorption
a_v	Absorbance
A_v	Integrated absorbance
b	Coefficient of polynomial expression
c	Speed of light
c	Coefficient of polynomial expression
c_p	Heat capacity at constant pressure
d	Coefficient of polynomial expression
D_λ	Normalized optical density
E	Total internal energy
E''	Lower-state energy
E_a	Activation energy
E_{elec}	Electronic energy
E_{rot}	Rotational energy
E_{vib}	Vibrational energy
FSR	Free spectral region
g_i	Degeneracy of level i
h	Planck constant
h	Enthalpy
I_0	Incident intensity
I_{etalon}	Intensity behind etalon
I_{ref}	Reference intensity
I_t	Transmitted intensity
k	Rate constant
k	Boltzmann constant
k_v	Absorption coefficient
L	Path length
M	Molar mass
m	Mass

M_s	Mach number
N	Total number of molecules
n	Number density
n	Temperature-dependent exponent
n_{air}	Temperature-dependent exponent of air
p	Pressure
R	Univeral gas constant
R	Line strength ratio
$S(T)$	Line strength
S^*	Line strength used in HITRAN
T	Temperature
t	Time
T_0	Reference temperature
T_{trans}	Translational temperature
U	Velocity
$U(x)$	Potential field
V	Velocity
ν_o	Line center
W	Non-dimensional distance from line center
X	Distance
x_{abs}	Mole fraction of absorption species
Z	Partition function
Z_B	Total collision frequency
Z_{elec}	Electronic partition function
Z_{rot}	Rotational partition function
Z_{vib}	Vibrational partition function
γ	Heat capacity ratio
γ	Broadening half width
γ_{air}	Air-broadening half width
γ_{Ar}	Argon broadening half width
γ_{self}	Self-broadening half width
$\Delta\nu$	Full width at half maximum (FWHM)
$\Delta\nu_C$	Collisional FWHM
$\Delta\nu_D$	Doppler FWHM

ε_i	Common energy of level i
λ	Wavelength
ν	Frequency
ρ	Density
σ_v	Frequency-dependent absorption cross section
τ	Transmission
τ	Normalized induction time
E'	Upper state
E"	Lower-state
τ_i	Lifetime of level *i*
ϕ	Equivalence ratio
$\phi(\nu)$	Line shape function
$\phi_C(\nu)$	Collisional line shape function
$\phi_D(\nu)$	Doppler line shape function
$\phi_v(\nu)$	Voigt line shape function
$\psi(t)$	Time-dependent Schrödinger equation
$\tilde{\nu}$	Wavenumber

Acknowledgements

I am sincerely grateful to Prof. Dr. Christof Schulz for his guidance and support during my work. I enjoyed each time meeting with him, presenting my research, discussing the results, and solving the problems. The knowledge and experiences that I learnt from him are remarkably valuable fortune for my future life.

I would like to acknowledge my group leader Dr. Mustapha Fikri for his patience and continuous support on this thesis. I sincerely appreciate his warm encouragement, genuine advices, and countless help. I would like also to thank Prof. Ron Hanson and Dr. Jay Jeffries from Stanford University for the discussions and advices in my research.

Many thanks to my former colleague Dr. Mohammad Aghsaee who shared his knowledge and experience in shock-tube technique and chemical kinetics. I want to acknowledge my colleague Dr. Jürgen Herzler for many valuable discussions and advices during my research. I would like to thank my colleague Siavash Zabeti and Dr. Sebastian Peukert for assisting me in anisole experiments. I want to thank my colleague Lin Shi for sharing his knowledge and experiences in laser diagnostics. Further I want to acknowledge my current and former colleagues in kinetics group: Dr. Oliver Welz, Dr. Metehan Bozkurt, Philip Niegemann, Paul Sela, and Dr. Damien Nativel. Thanks for the nice atmosphere all of them have brought to me.

I deeply thank Ludger Jerig, Dieter Hermanns, Birgit Nelius, Natascha Schlösser, Beate Endres, and Jörg Albrecht for their continuously kind supports in the lab. I sincerely thank Barbara Nota and Barbara Graf for managing the administrative tasks. It is so fortunate for me to work at IVG.

Most of all, I would like to thank my parents for their endless love and supporting of my study in Germany. Special thanks to my wife, Di, for her love, support, and patience. She brings too much happiness into my life. Our first daughter, Emma, brings more joy to our lives.

1. Introduction

1.1. Background and motivation

The major part of the world's energy demand is satisfied by the combustion of fossil fuels. As combustion technology develops, energy efficiency and pollutant emissions have given more attention. Hence, the design and the optimization of modern, environmentally friendly combustion systems relies heavily on accurate modeling of the fundamental chemical processes. Chemical processes can be coupled with the transport models in mathematical algorithms to model the combustion processes. However, these models are incomplete without experimental validation. In general, a reaction mechanism requires a database of accurate chemical reaction rate constants for the temperature and pressure range of interest. The validation of such mechanisms requires care to determine accurate values such as ignition delay times, temperature variations, and species concentration–time histories in reacting or combusting flows with well-defined temperature, pressure, and reaction time.

The vast majority of fuels such as Diesel, gasoline, and natural gas that are consumed in modern combustion devices (engines, gas turbines, and furnaces) are hydrocarbons. The primary products of hydrocarbon fuel combustion such as water vapor (H_2O), carbon dioxide (CO_2), and carbon monoxide (CO) can be interpreted to indicate combustion efficiency. Flexibility between the conversion and storage of energy will be an important aspect in future energy system [1], but optimization of current combustion systems will be an important transition to improve technology. Such improvements are possible through close interaction of simulations and measurements, where the latter provide data on concentrations [2], particle formation [3], flows [4], temperature [5], and pressure [6] inside modern combustion devices.

Shock tubes are widely established as tools to study ultrafast high-temperature gas-phase processes [7-9]. They provide a well-controlled uniform environment with wide range of temperature and pressure after rapid heat-up by a shock wave. The combination with modern diagnostic methods such as laser absorption spectroscopy [10], time-of-flight mass-spectrometer [11], and gas chromatography [12] enables single or multi-species measurements to follow the kinetics of the initial reactants, intermediates, or products.

Tunable diode-laser absorption spectroscopy (TDLAS) is a non-invasive, sensitive, and selective technique that has been developed during the last decades. It plays a major role in the measurement of temperature, concentrations, velocity, density, and pressure in a variety of environments [13-15]. TDLAS has been successfully applied by several groups in the studies of

combustion and propulsion systems [2, 16, 17] and provides *in situ* line-of-sight (LOS) measurements with fast time response.

Most hydrocarbons exhibit absorption spectra in the infrared (IR) region and common combustion products (e.g., H_2O, CO_2, and CO) absorb at wavelength from 1 to 6 µm at a representative combustion temperature of 1600 K. IR-laser-based absorption sensors near 1.5, 2.7, and 2.3 µm for detecting H_2O, CO_2, and CO, respectively, were first designed due to the availability of light sources, transmitting/absorbing materials (fibers), and detectors at these wavelengths [18-21]. These overtone bands (in the near IR, NIR) are orders of magnitude weaker compared to the fundamental bands between 3 and 6 µm (mid IR, MIR). With the development of the quantum-cascade (QC) laser technology, the range of continuous-wave (cw) room-temperature single-mode diode lasers has been extended to 6 µm, allowing for access to stronger absorption bands of CO, CO_2, and other species [22, 23]. The initial development of sensors at these longer wavelengths, which provide fingerprint information of many hydrocarbons, has been reported, demonstrating more selective and sensitive measurements of species concentration and temperature [24-26]. As part of this work, two-line absorption thermometry of CO near 4.7 µm was further developed and has been applied for kinetics studies in this thesis.

The kinetics target of this thesis focusses on three different studies:

- First, speciation of CO concentration during the partial oxidation of fuel-rich methane/air mixtures that are supposed to provide possible high-temperature pathways for polygeneration processes that allow to convert natural gas into higher-value chemicals. Dimethyl ether (DME) and *n*-heptane were used as additives to reduce ignition temperatures.
- Second, the thermal decomposition of anisole ($C_6H_5OCH_3$) which is considered a surrogate for kinetic studies of biomass combustion and recently was identified as an appropriate fluorescence tracer for fuel/air mixing studies based on laser-induced fluorescence (LIF).
- Third, the influence of hydrogen (H_2), oxygen (O_2), and methane (CH_4) on soot formation during the pyrolysis of acetylene (C_2H_2) and benzene (C_6H_6).

The measurements were performed in a shock tube combined with the diode-laser based two-line absorption thermometry which enables simultaneous temperature and CO concentration measurement with microsecond time resolution. Furthermore, detailed kinetics analyses based on relative mechanisms have been implemented for additional information of each investigation, respectively.

The thesis is organized as follows: Chapter 2 describes the fundamental of chemical kinetics, the shock-tube technique, and laser absorption spectroscopy; Chapter 3 introduces the background and the results of validation of the tunable diode laser (TDL) sensor near 4.7 μm for gas-phase temperature and CO-concentration measurements; Chapter 4 presents the results of the kinetics studies: (i) the investigations of oxidation of fuel-rich CH_4/O_2 mixture with additives (DME and *n*-heptane); (ii) the thermal decomposition of anisole; (iii) the soot formation during pyrolysis of C_2H_2 and C_6H_6 with presence of H_2, O_2, and CH_4, Chapter 5 discusses the outlook for the TDLAS measurement in the shock tubes; Chapter 6 summarizes these studies and gives conclusions.

2. Theoretical and experimental fundamentals

2.1. Reaction kinetics

Thermodynamics describe chemical reactions where the initial and final stage of a reaction system is considered and gives the direction of the conversion. The time behavior, however, is subject of chemical kinetics that deals with the rates of chemical reactions and factors that influence the reaction rates. In this chapter, the theory of chemical kinetics is briefly introduced.

2.1.1. Reaction rate constant

A kinetics model is constituted by a series of elementary reactions. For an elementary reaction aA + bB = cC + dD, a reaction rate constant k relates the reaction rate with the concentration terms at a certain temperature

$$R = \mathrm{d[A]}/\mathrm{d}t = k\,[\mathrm{A}]^{a}\,[\mathrm{B}]^{b}\,. \tag{2.1}$$

The rate constant k can be determined by measuring the temporal variation in concentration at known concentrations of the reactants.

Temperature dependence

The temperature dependence of a rate constant can be described by the Arrhenius equation

$$k = A\,\exp\left(-E_a/RT\right), \tag{2.2}$$

here, A is the pre-exponential factor, E_a is the activation energy, and R is the universal gas constant. According to equation (2.2), a plot of ln k versus $1/T$ should be linear with a negative slope of E_a/R. This plot is known as Arrhenius plot. For $T \rightarrow \infty$, the reaction rate constant takes formally the value of A. There are many possible causes of non-Arrhenius behavior such as temperature-dependent activation energy [27].

In the practical measurements, a modified expression of the further temperature dependence is adopted

$$k = A\,T^{n}\,\exp\left(-E_a/RT\right), \tag{2.3}$$

where the exponent n has a particular value depends on the nature of the reaction. When treating the same experimental data with both equations (2.2) and (2.3), the obtained activation energies

may differ from hundreds or thousands of J/mol. It must be noted that the rate constants measured from the Arrhenius equations are only valid in the temperature range where the parameter *A*, *n*, and E_a were determined [28].

Pressure dependence

The pressure dependence of the reaction rate constant was first proposed by Lindemann in 1922 [29] and the theory was further developed by Hinshelwood. The Lindemann theory defined low-pressure and high-pressure limits for the gas-phase unimolecular reactions. According to Lindemann-Hinshelwood mechanism, in the low-pressure limit, a third-body collision from any molecule M (usually the bath gas) is required to provide the necessary energy for the reaction to proceed (molecular activation). The excited molecule can be again deactivated through another collision. With the increase of the pressure, the activation and deactivation of the molecule can reach equilibrium and the reaction rate will no longer change with the concentration, i.e. the rate constant reaches its high-pressure limit (k_∞).

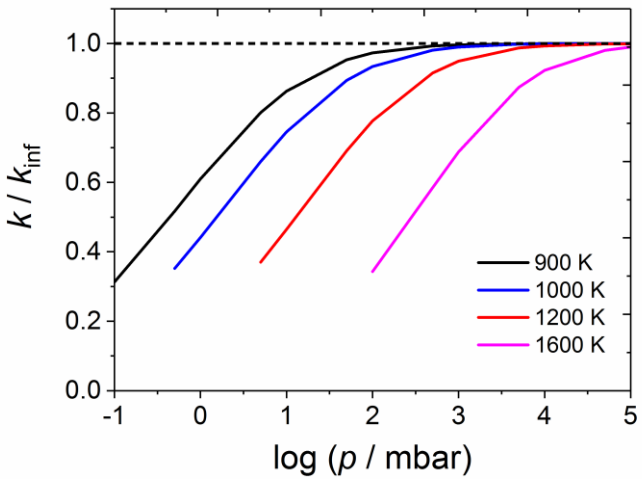

Figure 2.1: Fall-off curves for the unimolecular reaction $C_6H_5O \rightarrow C_5H_5 + CO$

The transition between the low-pressure and the high-pressure limit is defined as fall-off regime (Figure 2.1). To describe the behavior of the associated rate constant in the fall-off regime, a mathematical model was proposed by Lindemann and yields so-called fall-off curves [29]. A more accurate description which involves more complex expression for the broadening factor of fall-off curves was proposed later by Troe in 1974 [30] known as Troe formalism or parametrization is now widely used to describe the pressure dependence of rate constants. The fall-off curves strongly depend on the molecular structure and the temperature. Therefore, the fall-off curves of different reactions are distinct from each other at the same temperature and the

rate constant of the same reaction shows different temperature dependences at different pressures.

2.1.2. Reaction mechanism

Elementary reactions can be distinguished in three types, i.e. unimolecular, bimolecular, and termolecular reactions. In a unimolecular reaction, the reactant either dissociates or isomerizes to produce one or more products. The rearrangement of the molecule in the unimolecular reaction can include the thermal decomposition, ring opening, and racemization [31]. Elementary reactions initiated via collision of two or three different molecules are defined as bimolecular and termolecular reactions, respectively. According to collision theory, the probability of termolecular reactions is negligible and most of these reactions can be broken down into a more fundamental set of bimolecular reactions [31]. Reaction 2.1 and 2.2 represent typical unimolecular and bimolecular reactions of methane, respectively.

$$CH_4 \rightarrow CH_3 + H \quad \text{(R 2.1)}$$

$$CH_4 + H \rightarrow H_2 + CH_3 \quad \text{(R 2.2)}$$

Combustion processes typically include a series of elementary reactions that can exceed thousands of reactions. Accurate rate constants obtained from experiments, theoretical calculation, or empirical estimation for each reaction are necessary. Mechanisms can be validated regarding to global parameters such as flame speed and ignition delay time [31] or specific parameters such as species concentrations.

By analyzing complex mechanism, the rate law for interested species X is calculated by summing the rate laws of all elementary reactions in which the X is involved. One simple example is the H_2/O_2 combustion whose overall process can be described in R 2.3 and detailed reaction steps can be represented by a simple mechanism includes four reactions, i.e. R 2.4–2.7:

$$2H_2 + O_2 \rightarrow 2H_2O \quad \text{(R 2.3)}$$

$$H_2 + O_2 \rightarrow 2OH \quad \text{(R 2.4)}$$

$$OH + H_2 \rightarrow H_2O + H \quad \text{(R 2.5)}$$

$$H + O_2 \rightarrow OH + O \quad \text{(R 2.6)}$$

$$O + H_2 \rightarrow OH + H \quad \text{(R 2.7)}$$

Here, the rate constant of the OH radical is related to all four reactions. More general, equation (2.4) describes the rate law for species X_i in a mechanism that consists of M reactions and N species [32]

$$\frac{d[X_i]}{dt} = F_i(X_1,...,X_N;k_1,\ldots,k_M) = \sum_{i=1}^{m} X_i\left(v_{i,j}^{p} - v_{i,j}^{e}\right)R_j; i = 1,2,...,N \ , \tag{2.4}$$

here, $[X_i]$ is the concentration of species X_i, $v_{i,j}^{p}$ and $v_{i,j}^{e}$ are the stoichiometric coefficients of product and educt, respectively. R_j defines the rate of species conversion in forward and backward direction and is calculated by

$$R_j = k_j \prod_{i=1}^{N}[X_i]^{v_{i,j}^{e}} - k_{-j}\prod_{i=1}^{N}[X_i]^{v_{i,j}^{p}}; i = 1,2,...,N \ , \tag{2.5}$$

where k_j and k_{-j} are rate constants of forward and backward reactions, respectively.

For the combustion of large hydrocarbon fuels, the complexity of the mechanism increases strongly due to their large chain length. Therefore, more elementary reactions are required to represent the whole process. Some of the rate constants can be experimentally determined but more of them can only be estimated using quantum calculations or based on analogies. In the sensitive analysis of an interested species, it is noticed that only few of the reactions are rate determining for the overall process even there are huge number of reactions where the species is involved.

Experimental facilities such as shock tubes, flow reactors, cells, etc. combined with various diagnostics provide the possibility to extract opportunity for determining the underlying rate constants of the elementary reactions experimentally. However, theoretical methods such as Rice-Ramsperger-Kasserl-Marcus (RRKM) and multi-quantum Rice-Ramsperger-Kasser (QRRK) theory [33, 34] based on the transition state theory [35] can also provide the possibility for computational determination of rate constants from a few characteristics of the potential energy surface. Modern chemical kinetics software such as chemical workbench [36] provides a platform to implement fast analysis of a selected kinetics model. By defining the reaction environments, the concentration–time profiles can be obtained and compared with experimental values

2.2. Shock-tube theory

The first shock-tube apparatus and its principles were described in 1899 by Paul Vieille [37]. Nowadays shock tubes are widely used in different research fields like aerodynamics, physics, and chemical kinetics [8, 38, 39]. Test gases in shock tube are typically heated up quasi-instantaneously and homogeneously through the passage of the generated shock wave within a time of 1 µs. Hence, surface effects and transport processes behind reflected shock waves can be generally neglected. Shock tubes can cover typical range of temperatures from 800 to 4000 K and pressures from 0.1 to 1000 bar with test times of few hundred microseconds up to several milliseconds. When coupled with modern diagnostic methods [12] with fast-response and high time resolution, shock tubes become indispensable tools to study fast chemical processes.

Shock tubes are thick wall tubes usually constructed typically of stainless steel and with rectangular or circular cross-section [40]. Diaphragms, normally from aluminum or polymer sheets, with thickness from tens of micrometers up to several millimeters, separate the shock tube into a low-pressure section (e.g., driven section) containing the test gas and a high-pressure section (e.g., driver section). The high-pressure section is filled with driver gas to initiate the experiment. To achieve stronger shocks, the driver gas is usually chosen to have high speed of sound and low ratio of specific heats (γ). Therefore, gases with low molecular weight such as H_2 and He are most frequently chosen. The driver gas is filled into the driver section until the diaphragm ruptures and expands into the driven section. An incident wave will be generated in front of the driver gas and propagates towards the test gas. The incident shock wave passes through the test gas and increases the temperature and the pressure of the test gas behind it. The incident shock wave will be reflected back off the end wall of the driven section towards the driver section. The temperature and pressure of the test gas will undergo a second sudden increase when the reflected shock wave passes through and the velocity of the gas behind the reflected shock wave is zero.

Uniform temperature and pressure conditions of the test gas behind the reflected shock waves can last from hundreds of microseconds up to several milliseconds. These stationary conditions will eventually be interrupted by two disturbances. First, the separation between the driver and driven gases is named as contact surface (CS), the CS moves towards the driven section and will meet the reflected shock wave (RSW). Depending on the properties of the gases, expansion waves or reflected waves will be generated during the interaction of RSW and CS and move towards the end wall of the driven section. Second, immediately after the burst of the diaphragm,

series of expansion waves that propagate towards the driver section are generated. These expansion waves are reflected by the end flange of the driver section and move towards the driven region, and the shock-heated test gas will be then strongly quenched due to the arrival of the expansion waves.

Figure 2.2 represents the schematics of the shock tube. The generation and the propagation of the shock waves are described in the followed distance–time (x–t) diagram with the time of the diaphragm's burst as $t = 0$. There are five regions defined during the whole procedure: Region 1 and 4 denote the initial condition in the driven and driver section before the diaphragm's rupture, respectively. Region 2 and 3 define the condition behind the incident shock wave and the expansion waves (rarefaction), respectively, and are separated by the CS. Region 5 represents the conditions behind the reflected shock wave. The pressure and temperature distribution of the five regions are depicted in the five x–t diagrams in Figure 2.2a–e.

The initial conditions of the test gas in the driven section are T_1 and p_1. Prior to the rupture of the diaphragm the states of the driver gas are T_4 and p_4. T_2 and p_2 denote the temperature and pressure of the test gas behind the incident wave and in front of the CS. T_5 and p_5 referred to the condition behind the reflected shock wave before the RSW meet the CS. The rarefaction waves generated simultaneously with the incident shock wave travel towards the end wall of the driver section and cool down the driver gas behind the rarefactions to T_3 and p_3. The CS that separates the driven and driver gases permanently moves towards to driven section due the initial pressure differences between p_1 and p_4. Test time Δt defines the duration of the steady condition in region 5 and is limited by the arrival of the reflected rarefaction or the interaction between the CS and RSW. In the present study, according to the geometry of the shock tube typical test times are about 1–2 ms (Figure 2.3).

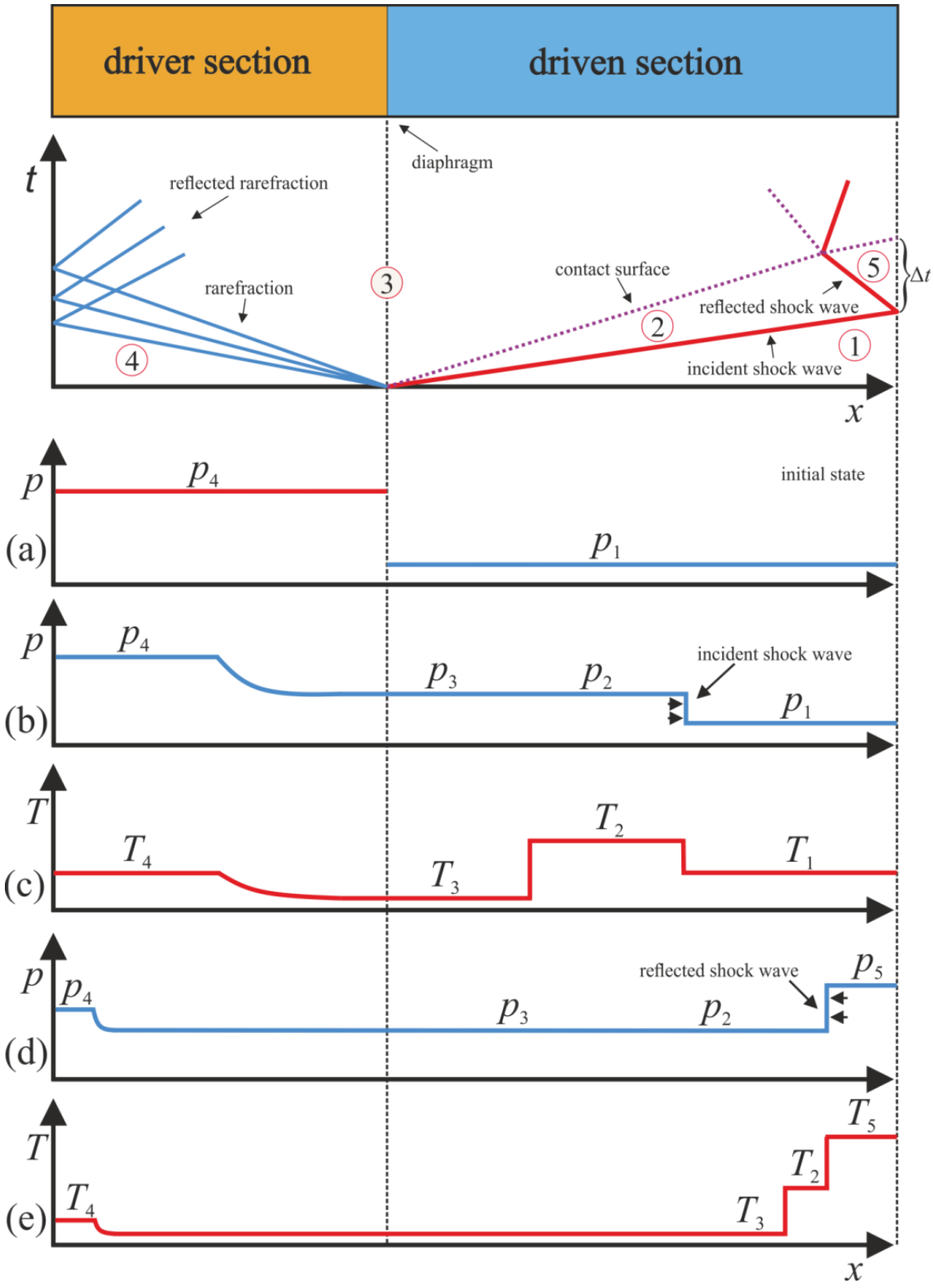

Figure 2.2: *x*–*t* diagram and operation principle of shock tube.

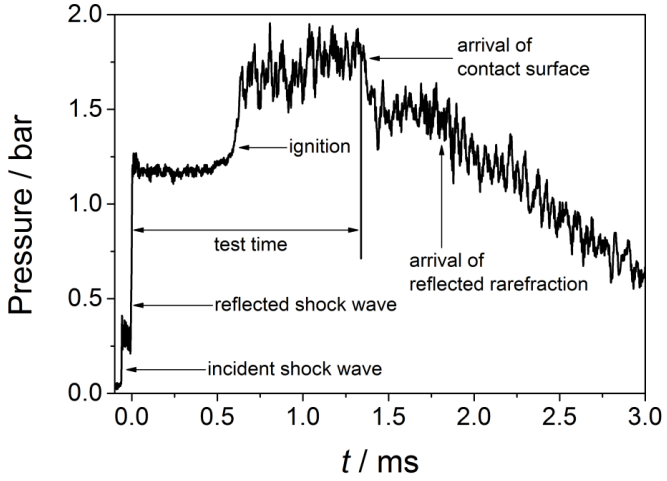

Figure 2.3: Pressure profile and corresponding test time for a typical shock-tube experiment measured in the facility used in this thesis.

The thermodynamic variables temperature (T), pressure (p), and density (ρ) of the test gas behind the shock waves can be calculated using gas dynamic equations based on 1D shock-wave coordinates [41] (Figure 2.4). The transformation of laboratory fixed to shock fixed coordinates makes the calculation mathematically easier. The first step increase in temperature, pressure, and density for an ideal gas behind the incident shock wave are given by the Rankine-Hugoniot equations [42, 43] following the conservation of mass, momentum, and the energy (Eq. 2.6–2.8).

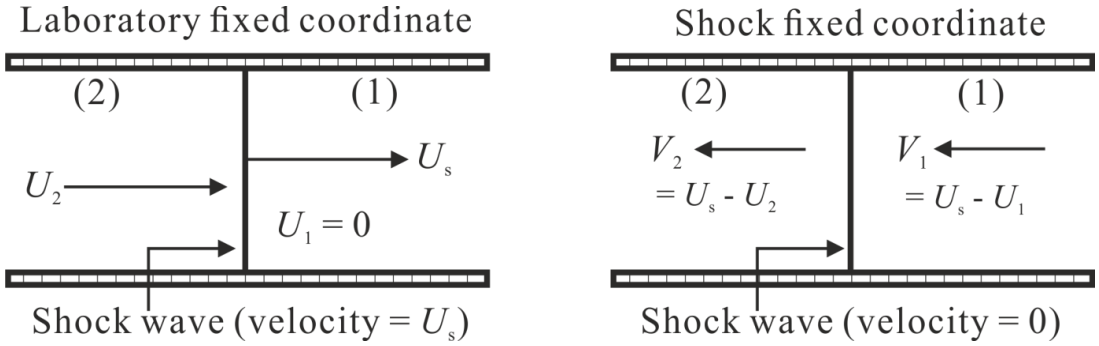

Figure 2.4: One-dimensional shock wave flow coordinates.

$$\rho_1 v_1 = \rho_2 v_2 \tag{2.6}$$

$$\rho_1 v_1^2 + p_1 = \rho_2 v_2^2 + p_2 \tag{2.7}$$

$$\frac{1}{2} v_1^2 + h_1 = \frac{1}{2} v_2^2 + h_2 \tag{2.8}$$

v and *h* define the velocity and enthalpy of the gas on both side of the shock front in the shock-fixed coordinate, respectively, and v_1 is equal to u_s which refer to the velocity of the shock front in the laboratory-fixed coordinate. Assuming the gas to be ideal, thermal and caloric equations of state can be used.

$$p = \rho RT \tag{2.9}$$

$$h = c_p T = \frac{\gamma}{\gamma - 1} RT \tag{2.10}$$

here, c_p is the heat capacity at constant pressure and the γ denotes the heat capacity ratio. By substituting the equation (2.9) and (2.10) into (2.8), the temperature, pressure, and density ratio of the gases can be obtained.

$$\frac{T_2}{T_1} = 1 + \frac{2(\gamma - 1)}{(\gamma + 1)^2} \frac{\gamma \mathrm{M}_s^2 + 1}{\mathrm{M}_s^2} \left(\mathrm{M}_s^2 - 1 \right) \tag{2.11}$$

$$\frac{p_2}{p_1} = 1 + \frac{2\gamma}{\gamma + 1} \left(\mathrm{M}_s^2 - 1 \right) \tag{2.12}$$

$$\frac{\rho_2}{\rho_1} = \frac{(\gamma + 1)\mathrm{M}_s^2}{(\gamma - 1)\mathrm{M}_s^2 + 2} \tag{2.13}$$

here, M_s is the Mach number of shock front which is determined from the velocity of the incident shock wave using

$$M_s = \frac{u_s}{a_s} = \frac{v_1}{\sqrt{\frac{\gamma RT_1}{M}}} \ , \tag{2.14}$$

M is the molar mass of the test gas. The condition of the test gas behind the reflected shock wave can be calculated through the similar derivation and the following expressions are obtained.

$$\frac{p_5}{p_1} = \left[\frac{2\gamma \mathrm{M}_s^2 - (\gamma - 1)}{\gamma + 1} \right] \left[\frac{(3\gamma - 1)\mathrm{M}_s^2 - 2(\gamma - 1)}{(\gamma - 1)\mathrm{M}_s^2 + 2} \right] \tag{2.15}$$

$$\frac{T_5}{T_1} = \frac{\left(2(\gamma - 1)\mathrm{M}_s^2 + (3 - \gamma)\right)\left((3\gamma - 1)\mathrm{M}_s^2 - 2(\gamma - 1)\right)}{(\gamma + 1)^2 \mathrm{M}_s^2} \tag{2.16}$$

$$\frac{\rho_5}{\rho_1} = \frac{p_5}{p_1}\frac{T_1}{T_5} \tag{2.17}$$

2.3. Laser spectroscopy

2.3.1. Quantum mechanics

Laser diagnostic spectroscopy is a non-intrusive method that has gained importance to *in situ* study ultrafast gas-phase reactions with fast time response and high time resolution [13, 44-46]. Spectroscopy, chemical reaction dynamics, statistical thermodynamics, molecular properties, and molecular structure determination are all areas that can be gained from principles of quantum mechanics. The theory quantizes the energy of the atoms and molecules by describing the existences of atoms and molecules in specific quantum states with discrete values of energy and angular momentum [46]. The time-independent Schrödinger equation is used to determine the energy levels for the molecule with mass *m* moving in a potential field by $V(x)$.

$$\frac{d^2\psi(x)}{dx^2} + \frac{8m\pi^2}{h^2}\left[E - V(x)\right]\psi(x) = 0 \tag{2.18}$$

h is Planck's constant, *E* is the total internal energy of the system, which excludes kinetic energy, as the sum of electronic, vibrational, and rotational energy.

$$E = E_{\text{elec}} + E_{\text{vib}} + E_{\text{rot}} \tag{2.19}$$

The discrete values of internal energy lead to discrete transitions in energy when atoms or molecules change quantum states. These energy differences correspond directly with the energy of emitted or absorbed photons in discrete spectra. When radiative transitions between two molecular quantum sates occur, the energy differences, ΔE, of the photon-induced transitions between these two quantum states can be described by the Planck's law.

$$\Delta E = E_{\text{upper}} - E_{\text{lower}} = h\nu = h\frac{c}{\lambda} = h\tilde{\nu} \tag{2.20}$$

Here, *c* is the speed of the light [m/s], ν, λ, and $\tilde{\nu}$ are the frequency [s^{-1}], the wavelength [nm], and the wavenumber [cm^{-1}] of the corresponding electromagnetic wave, respectively.

Equation 2.21 expresses the Eq. 2.20 as sum of the individual changes in rotational, vibrational, and electronic energy and defines the molecular transitions (emission or absorption) into three domains [46].

$$\Delta E = \Delta E_{\text{elec}} + \Delta E_{\text{vib}} + \Delta E_{\text{rot}} \tag{2.21}$$

Where:

ΔE_{rot}: microwave transitions (1000 μm – 1 m)

$\Delta E_{\text{rot}}+\Delta E_{\text{vib}}$: IR transitions (700 nm – 1000 μm)

$\Delta E_{\text{rot}}+\Delta E_{\text{vib}}+\Delta E_{\text{elec}}$: UV / visible transitions (10 – 700 nm)

2.3.2. Boltzmann distribution

The Boltzmann distribution equations describe the temperature-dependent population distribution of molecules or atoms of a single species over its allowed quantum states. The fraction of molecules in energy level *i* is described by [47].

$$\frac{N_i}{N} = \frac{g_i \exp\left(-\frac{\varepsilon_i}{kT}\right)}{Z(T)} \tag{2.22}$$

$$N = \sum_i N_i \tag{2.23}$$

Where k is Boltzmann's constant, N is the total number of molecules, g_i and ε_i are the degeneracy and the common energy of level i, respectively. $Z(T)$ is a specific energy-weighted sum over all levels known as partition function expressed by Eq. 2.24, which can be also written as the product of rotational, vibrational, and electronic partition functions, Z_{rot}, Z_{vib}, and Z_{elec}, respectively.

$$Z = \sum_i g_i \exp\left(-\frac{\varepsilon_i}{kT}\right) = Z_{\text{rot}} Z_{\text{vib}} Z_{\text{elec}} \tag{2.24}$$

2.3.3. Beer-Lambert law

The typical schematics of an absorption spectroscopy measurement is illustrated in Figure 2.5. The incident laser beam passes through a gas medium with concentration n and a length of L, the transmitted laser beam intensity behind the gas medium I_t is then recorded by a detector.

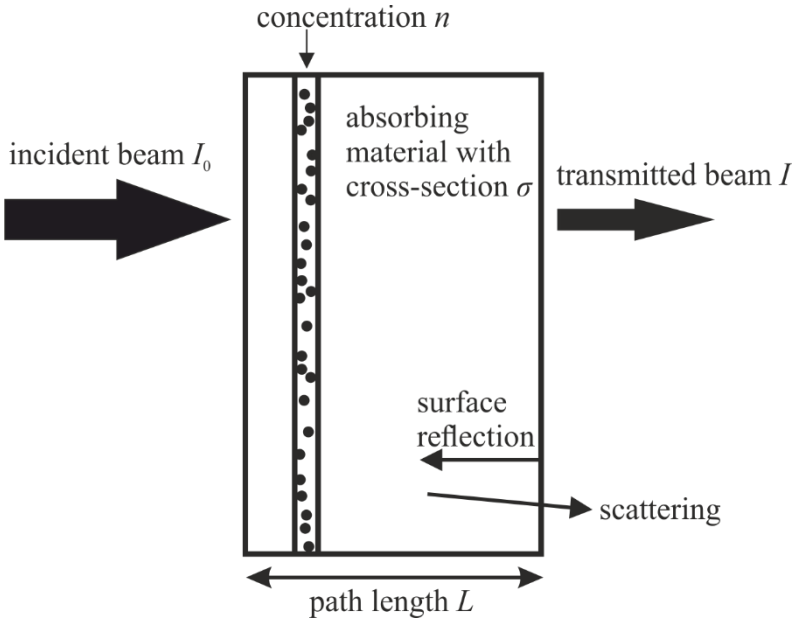

Figure 2.5: Schematics of an absorption measurement.

The fundamental law to describe the absorption spectroscopy is the Beer-Lambert law, the relationship between the I_0, I_t, n, and L can be expressed in the following equation.

$$\tau = \frac{I_t}{I_0} = \exp\left(-n\sigma_\nu L\right) = \exp\left(-k_\nu L\right) \tag{2.25}$$

Where τ is the transmission, n is the number density of the absorbing species [molecules/cm^3], σ_ν [cm^{2}molecules^{-1}] is the frequency-dependent absorption cross-section, and k_ν [cm^{-1}] is the spectral absorption coefficient. For an isolated transition i with frequency ν,

$$k_\nu = S_i p x_{\text{abs}} \phi(\nu) \ , \tag{2.26}$$

where p [bar] is the total pressure of the gas medium, x_{abs} is the mole fraction of the absorbing species of interest, $\phi(\nu)$ is the line shape function, $S_i(T)$ [cm^{-2}bar^{-1}] is the line strength of the transition i and is a function of temperature according to

$$S\left(T\right) = S\left(T_0\right)\frac{Z\left(T_0\right)}{Z\left(T\right)}\left(\frac{T_0}{T}\right)\exp\left[-\frac{hcE''}{k}\left(\frac{1}{T}-\frac{1}{T_0}\right)\right]\frac{1-\exp\left(\frac{hc\nu_0}{kT}\right)}{1-\exp\left(\frac{hc\nu_0}{kT_0}\right)} \ . \tag{2.27}$$

Here k is the Boltzmann's constant, $S(T_0)$ is the line strength at a reference temperature T_0, ν_0 is the center frequency of the transition, E'' is the lower-state energy of the ν_0 and $Z(T)$ is the

partition function of the absorption species of interest. The parameters at the reference temperature T_0 can be measured in a static cell or obtained from the HITRAN database [48]. It should be noted that in the HITRAN the reference temperature is always set to 296 K.

The typical units for line strength is either a pressure-dependent version [$cm^{-2}atm^{-1}$] used in this thesis or a number-density dependent version used in the HITRAN which is denoted as S^* [$cm^{-1}/(mol \cdot cm^{-2})$]. For some transitions that have no absorption spectra at low temperature, the $S(T_0)$ at 296 K is normally obtained from HITRAN and a conversion between S and S^* is necessary [46]

$$S[\mathrm{cm^{-2}atm^{-1}}] = \frac{S^*[\mathrm{cm^{-1}/(mol \times cm^{-2})}] \times n[\mathrm{mol/cm^3}]}{p[\mathrm{atm}]} \ , \tag{2.28}$$

where n is the number density. By applying the ideal gas law and converting the unit of pressure into [Pa], following relationship is obtained

$$S[\mathrm{cm^{-2}atm^{-1}}] = \frac{S^*[\mathrm{cm^{-1}/(mol \times cm^{-2})}] \times 101325[\mathrm{Pa/atm})]}{kT} \ , \tag{2.29}$$

where the Boltzmann constant k has the value of 1.38054×10^{-23} [J/K]. For the line strength at reference temperature of 296 K the conversion can be simplified in form of equation 2.30.

$$S = S^* \times (2.488 \times 10^{19})\,[\mathrm{cm^{-2}atm^{-1}}] \tag{2.30}$$

The partition function Z(T) has been defined in Eq. 2.24 as the product of rotational, vibrational, and electronic partition functions and can be calculated approximately from the following third-order polynomial

$$\mathrm{Z}(T) = a + bT + cT^2 + dT^3 \ . \tag{2.31}$$

The coefficients of the polynomial expression a, b, c, and d are temperature and molecule dependent, i.e. the coefficients are different at different temperatures and the coefficients should be determined separately for each species of interest. Table 2.1 listed the coefficients of the polynomial expression for the partition function of carbon monoxide (CO) [49].

Table 2.1: Coefficients of the polynomial expression for the partition function of CO [49]

Coefficients	70 K < T < 500 K	500 K < T < 1500 K	1500 K < T < 3005 K
a	0.27758×10^{0}	0.90723×10^{1}	0.63418×10^{2}
b	0.36290×10^{0}	0.33263×10^{0}	0.20760×10^{0}
c	-0.74669×10^{-5}	0.11806×10^{-4}	0.10895×10^{-3}
d	0.14896×10^{-7}	0.27035×10^{-7}	0.19844×10^{-8}

The absorption defined by the Beer-Lambert law is described as

$$a_\nu = 1-\tau = 1-\frac{I_t}{I_0} = 1-\exp(-n\sigma_\nu L) = 1-\exp(-k_\nu L)\ . \tag{2.32}$$

In order to investigate the absorption parameters such as line strength and line shape, it is more convenient to convert the transmission or absorption into absorbance, which is proportional to line strength, total pressure, concentration of absorber, line shape function, and path length.

$$a_\nu = -\ln(\tau) = -\ln(\frac{I_t}{I_0}) = -n\sigma_\nu L = -k_\nu L = S_i p x_{\text{abs}} \phi(\nu) L \tag{2.33}$$

Since the line shape function $\phi(\nu)$ is normalized to the frequency as

$$\phi(\nu) = \frac{k_\nu}{\int k_\nu d\nu}\ , \tag{2.34}$$

therefore, its integral over the frequency is unity

$$\int_{-\infty}^{+\infty} \phi(\nu) d\nu = 1\ , \tag{2.35}$$

and the integrated absorbance of a single transition i can be expressed as

$$A_\nu = \int_{-\infty}^{\infty} a_\nu d\nu = S_i p x_{\text{abs}} L\ , \tag{2.36}$$

which is only related to temperature-dependent line strength, partial pressure of the absorber, and path length. For absorption measurements with unknown concentration, the concentration of the gas medium can be inferred from the measured absorbance

$$x_{\text{abs}} = \frac{a_\nu}{S_i p \phi(\nu) L} = \frac{A_\nu}{S_i p L} \quad . \tag{2.37}$$

2.3.4. Line-broadening

The line shape function $\phi(\nu)$ describes the shape of an isolated absorption line as a function of frequency; Figure 2.6 illustrates a typical line shape of an absorption line centered at ν_0. The line shape function has a maximum value of $\phi(\nu_0)$ at the center frequency ν_0. The width of the line can be described by the $\Delta\nu$ which is defined as the full width at half maximum (FWHM). In many references [50, 51], the half width at half maximum (HWHM) is also used to describe the line properties. Note that the integral in equation (2.35) is dimensionless. Since the unit of $d\nu$ is either cm^{-1} or s^{-1}, $\phi(\nu)$ has units of cm or s.

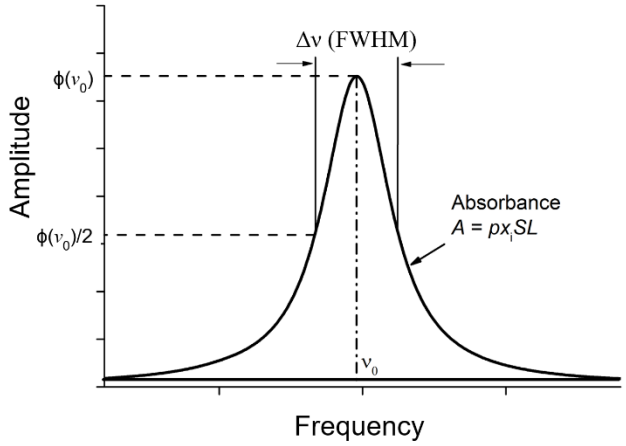

Figure 2.6: Typical line shape as a function of frequency.

When the energy levels of the transition are perturbed by physical mechanisms or the individual atoms or molecules interact with light, the line width broadens. This phenomenon is defined as absorption line-broadening [46]. The line-broadening mechanism can be either homogenous broadening where the effect is the same for all species, or inhomogeneous broadening which affects separate classes or subgroups. There are four important mechanisms that lead to line-broadening, which are natural, collisional, Doppler, and Stark broadening. In this thesis, only the collisional and Doppler broadening are discussed below because the other two mechanisms can be neglected in the gas-phase combustions.

Collisional broadening (pressure broadening)

The energy of optical transitions is the energy difference between two states. In the case of homogeneous broadening [46], the uncertainty of these energy levels can be related to their

lifetimes by the Heisenberg uncertainty principle [52] that limits the certainty in energy level *i* by

$$\Delta E_i \geq \frac{h}{2\pi\tau_i} \ , \tag{2.38}$$

where τ_i is the lifetime of level *i*. The total uncertainty of a transition in units of frequency $\Delta\nu$ can be expressed as a function of upper and lower-states, $\tau'$and τ'', respectively.

$$\Delta\nu = \frac{1}{2\pi}\left(\frac{1}{\tau'} + \frac{1}{\tau''}\right) \tag{2.39}$$

Since the uncertainty is the same for all molecules of the species of interest, the broadening is homogenous. The resulting line shape function $\phi(\nu)$ can be derived as a form of Lorentzian function [53].

$$\phi(\nu) = \frac{1}{2\pi}\frac{\Delta\nu}{\left(\nu - \nu_0\right)^2 + \frac{\Delta\nu^2}{2}} \tag{2.40}$$

The collision of two molecules in a gas can reduce the lifetime of the energy states. According to equation (2.39), the reduced lifetime leads to a broader line shape. Collisions that occur between identical species lead to so-called self-broadening, while the process also takes place between different species is called collisional broadening. The FWHM given by equation (2.39) due to the collisional broadening can be expressed as

$$\Delta\nu_C = \frac{Z_B}{\pi} \ . \tag{2.41}$$

Here, Z_B is the total collision frequency for a variety of different collision partners in the whole system. In a more convenient form, the net uncertainty $\Delta\nu_C$ for the investigated species *i* in a gas system is often modeled as the product of the total pressure and the sum of the mole fraction for each collisional partner *j* multiplied with its collisional coefficient $2\gamma_{i\text{-}j}$.

$$\Delta\nu_C = p\sum_j x_j 2\gamma_{i-j} \tag{2.42}$$

$$2\gamma(T) = 2\gamma(T_0)\left(\frac{T_0}{T}\right)^n \tag{2.43}$$

Here, *n* is the corresponding temperature-dependent coefficient. In the framework of this thesis, the collisional coefficients are either be measured or obtained from literatures. For the species whose collisional broadening values cannot be directly measured, an approximation of $2\gamma_{300K} \approx 0.1\,\mathrm{cm^{-1}bar^{-1}}$ and $n = 0.5$ was used [46]. According to equation (2.42) the FWHM of the collisional broadening is directly proportional to the pressure. Thus, collisional broadening is also known as pressure broadening.

Doppler broadening

Doppler broadening is the dominant inhomogeneous broadening mechanism and results from the so-called Doppler effect. When the direction of a molecule's velocity component is parallel to the light's propagation path, there will be a frequency shift called Doppler shift. The Maxwell velocity distribution function describes the molecules of any gas in constant motion and the distribution of their random velocities. Each group of molecules with the same velocity components is considered as a velocity class. Each velocity class has its own Doppler shift. The Maxwell velocity distribution function describes the fraction of molecules in each velocity class. The distribution function leads to a Doppler line shape function ϕ_D with a Gaussian form

$$\phi_D(\nu) = \frac{2}{\Delta\nu_D}\left(\frac{\ln 2}{\pi}\right)^{1/2} \exp\left\{-4\ln 2\left(\frac{\nu-\nu_0}{\Delta\nu_D}\right)^2\right\}. \tag{2.44}$$

Here, ν_0 is the center of the transition; $\Delta\nu_D$ is the Doppler width (FWHM) and is given by

$$\Delta\nu_D = \nu_0\left(\frac{8kT\ln 2}{mc^2}\right)^{1/2}, \tag{2.45}$$

which can be expressed in a more convenient form

$$\Delta\nu_D = \nu_0\left(7.1623\times10^{-7}\right)\left(\frac{T}{M}\right)^{1/2}, \tag{2.46}$$

where *T* is the temperature and *M* is the molecular mass. The Doppler width becomes broader at higher temperature, thus, the Doppler width can be used to roughly calculate the gas temperature [46].

Voigt profiles

Gaussian and Lorentzian line shape mechanisms describe the inhomogeneous and homogeneous line-broadening, respectively. Figure 2.7 shows the comparison between the Gaussian and Lorentzian line shapes when they have the same half width. The peak height of the Gaussian line shape is about 50% higher than the Lorentzian profile, but it drops off much faster in the wings.

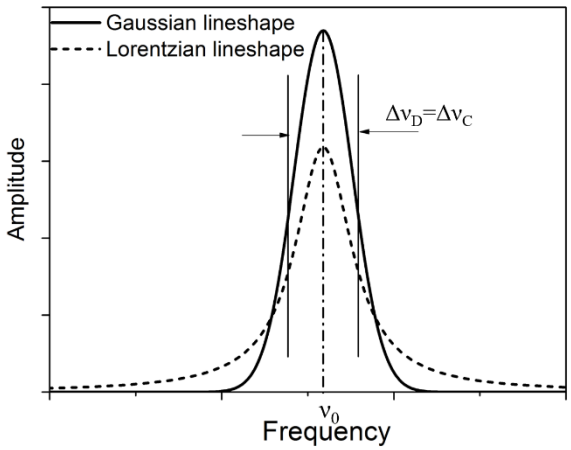

Figure 2.7: Comparison of Gaussian and Lorentzian line shapes with the same FWHM.

In the common case, none of the single broadening mechanism can describe the line shape of the system. Doppler broadening dominates at high temperature while the collisional broadening plays an important role at high pressure. Both mechanisms are significant and neither can be neglected in a combustion environment. Therefore, a function is proposed that combines both effects as a convolution of Doppler and collisional broadening

$$\phi_\nu(\nu)=\int_{-\infty}^{+\infty}\phi_D(u)\phi_C(\nu-u)\,du \ . \tag{2.47}$$

This convolution is called Voigt profile and can also be expressed as

$$\phi_\nu(\nu)=\phi_D(\nu_0)V(a,w) \ . \tag{2.48}$$

Here, $\phi_D(\nu_0)$ is the peak amplitude at the line center of the Doppler line shape

$$\phi_D(\nu_0)=\frac{2}{\Delta\nu_D}\left(\frac{\ln 2}{\pi}\right)^{1/2} \ . \tag{2.49}$$

a is the Voigt parameter that indicates the relative significance of Doppler and collisional broadening

$$a = \frac{\Delta\nu_C \sqrt{\ln 2}}{\Delta\nu_D} \tag{2.50}$$

and *w* is the non-dimensional distance from the line center that is proportional to the Doppler half width

$$w = \frac{2\sqrt{\ln 2}\left(\nu - \nu_0\right)}{\Delta\nu_D} \ . \tag{2.51}$$

$V(a, w)$ is the well-known "Voigt function" and can be calculated using standard mathematical routines [46]. In this study, the applied laser is set to the line center for each transition, the Voigt function can be reduced to

$$V(a,w) = V(a,0) = \exp(a^2)\mathrm{erfc}(a) \ . \tag{2.52}$$

2.3.5. Direct absorption spectroscopy

Direct absorption spectroscopy is the simplest method of the laser diagnostics and is widely applied in the measurements of many combustion parameters such as temperature, pressure, and species concentration. There are two typical experimental methods for direct absorption spectroscopy, i.e. fixed- and scanned-wavelength absorption spectroscopy.

Fixed-wavelength absorption spectroscopy

In fixed-wavelength absorption spectroscopy, the wavelength of the laser beam is fixed at the center of the absorption line, or a proper position if the absorption region is broad. The intensities of the laser beam before and after entering the investigated gas medium are acquired and the information during the acquisition time period can be evaluated. By applying sensors with high bandwidths in the order of several MHz, the acquisition of highly transient events such as in IC engines can be monitored. This method is easy to design whereas several aspects should be noticed.

First, since the accuracy strongly depends on the chosen wavelength, the correct line position should always be checked prior to each measurement. Modern laser techniques provide much stable laser sources where the wavelength can be fixed by certain combination of operating temperature and current, however, the shift of the wavelength can occur on long times (e.g.,

over hours) of operation. Therefore, instruments such as wavemeters or calibration cells are needed to identify the chosen wavelength.

Second, fixed wavelength lasers normally provide constant output power, but some disturbance in the measurement environment such as temperature and humidity changes will lead to some intensity variations. Such disturbances normally occur in long time scales and can be calibrated easily. In some cases, such as bad alignment of the line-of-sight, dirty optics, and fluctuating detector background, the change of the beam intensity may occur on short time scales, which leads to unreliable measurement results. Hence, highly stable detectors and averaging optics (e.g., integrating spheres) can be used to improve the signal qualities.

Third, by selecting absorption sensors, stronger transitions with known spectroscopic parameters such as line strength and line shape can bring high signal-to-noise ratios and save the time for line characterization. However, considering different application environments, weak absorption lines are also preferred in many cases, e.g., if target species have much higher concentration, to avoid non-linearity of the absorption.

Scanned-wavelength absorption spectroscopy

Contrary to the fixed-wavelength method, in scanned-wavelength absorption spectroscopy the wavelength of the light source is tuned over a certain range. The wavelength tuning can be achieved either by varying the operating temperature or the current of a diode laser. The scanned wavelength range can be monitored via a Fabry-Perot interferometer (etalon) with a known free spectral region (FSR). For quantum cascade lasers, the scanning range of the wavelength is normally smaller than 1 cm^{-1} and depends strongly on the scanning frequency, i.e. the scanning range decreases with increasing frequency. Some alternative methods such as intra-pulse strategy [54] can be applied to achieve wider scanning range under high scanning frequency. Figure 2.8 shows a typical setup of the scanned-wavelength method. Normally, three signals are needed, the reference, the transmitted, and the etalon signal (Figure 2.9). By selecting proper frequency and range, the whole line shape of an absorption line of a gas-phase species at pressure below ~ 20 bar can be obtained during the scan with high time resolution. The scanned profile line shape provides more accurate information of the absorbing species in comparison to the fixes-wavelength method; with the help of a reference signal, an accurate baseline can be obtained and intensity fluctuation of the laser source can be taken into account. Generally, the scanned-wavelength method can compensate for some drawbacks that affect the fixed-wavelength method. On the other hand, it loses its advantages for the measurements which required

high time resolution due to the limited scanning frequency. Furthermore, in some extreme cases such as measurements at high pressure (40 bar) and high temperature (2000 K) the scanned-wavelength method will lose the detailed feature of line shape due to strong line-broadening and shows no advantages compared to the fixed-wavelength method.

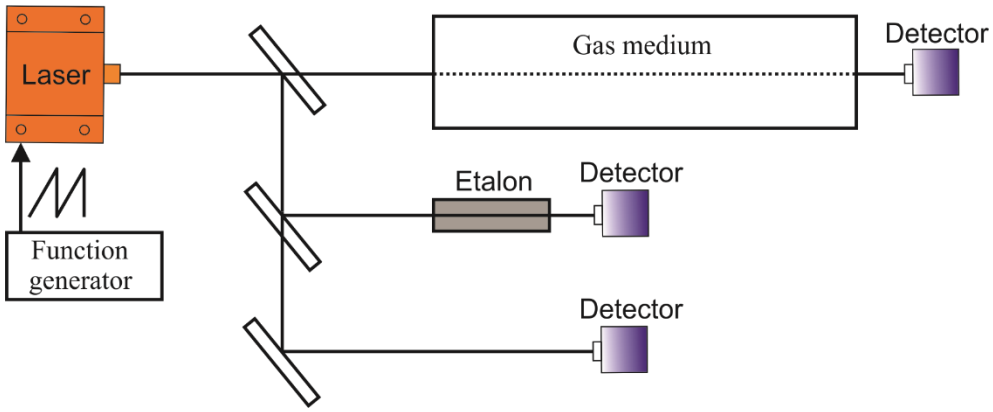

Figure 2.8: Schematics of a typical scanned-wavelength absorption experiment.

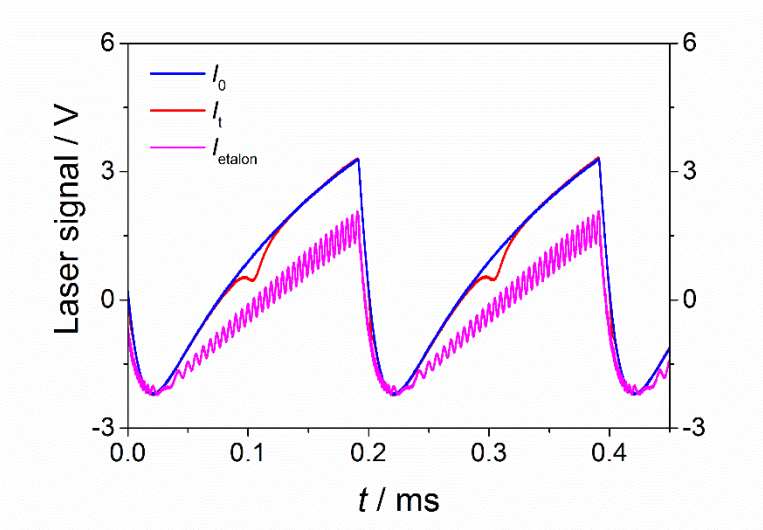

Figure 2.9: Signals of typical scanned-wavelength absorption experiment. The etalon signal allows to correlate time scale to absolute wavelength.

Absorbance-ratio-based thermometry

Temperature is a fundamental parameter in combustion processes. A variety of methods was applied to determine gas-phase temperature in combustion system [55-57]. In the past decades, spectra-based temperature measurements such as spectrum-line reversal [58] and laser induced fluorescence [59] have been widely used because they are non-intrusive and exhibit fast time response. Recently, absorbance-ratio-based thermometry with tunable diode-laser absorption

spectroscopy (TDLAS) has proved its capability for sensitive and accurate temperature sensing with high time resolution (several micro seconds) [60, 61]. Thus, the temperature information for many fast combustion processes such as in IC engines, shock tubes, and scramjet burners can be determined. By selecting two different transitions with different temperature-dependent line strengths, the temperature can be determined by rationing the line strengths without pre-requisite of background attention (or correction for it).

To infer temperature, the fixed-wavelength absorption technique is applied where the laser wavelengths are fixed at the center of two transition lines. The peak absorbance a_1 and a_2 at the line center of both transitions can be measured (Figure 2.10). According to the Beer-Lambert law (cf. equation (2.33)), the ratio R can be expressed as

$$R = \frac{a_1}{a_2} = \frac{k_{v1} L}{k_{v2} L} = \frac{p x_{abs} S_1(T) \phi(\nu_1) L}{p x_{abs} S_2(T) \phi(\nu_2) L} = \frac{S_1(T) \phi(\nu_1)}{S_2(T) \phi(\nu_2)} \quad . \tag{2.53}$$

By selecting two transitions that are located near to each other, the difference between both line shapes is very small and can be neglected. Hence, equation (2.53) can be simplified as the line strength ratio of two transitions. By substituting equation (2.27) into (2.53), the following expression is obtained

$$R(T) = \frac{a_1}{a_2} \approx \frac{S_1(T)}{S_2(T)} = \frac{S_1(T_0)}{S_2(T_0)} \exp\left[-\frac{hc}{k} \left(E_2'' - E_1'' \right) \left(\frac{1}{T} - \frac{1}{T_0} \right) \right] \quad . \tag{2.54}$$

Here, the absorbance ratio is only temperature dependent and the temperature can be calculated as

$$T(R) = \left[\ln \frac{R(T)}{R(T_0)} \cdot \frac{k}{hc} \cdot \frac{1}{E_2'' - E_1''} + \frac{1}{T_0} \right]^{-1} \quad . \tag{2.55}$$

$R(T_0)$ is the line strength ratio at the reference temperature T_0. In order to achieve maximum sensitivity of the temperature measurement, the relative sensitivity of the absorbance ratio to temperature can be analyzed by

$$\left| \frac{dR/R}{dT/T} \right| = \left(\frac{hc}{k} \right) \frac{\left| E_2'' - E_1'' \right|}{T} \quad . \tag{2.56}$$

It can be seen that by selecting a line pair with a large difference in the lower-state energies, the sensor will have a high temperature sensitivity. In practical applications, the sensitivity is preferred to be larger than 1 in the interested temperature range.

In the scanned-wavelength absorption technique, the absorbance is obtained from the integrated areas of the two transitions (Figure 2.11). The ratio of the absorbance is therefore independent of the line shape and is directly proportional to the line strength ratio. Moreover, the background absorbance can be measured simultaneously. Therefore, the uncertainty of the obtained temperature in this case is smaller than that of the fixed-wavelength technique.

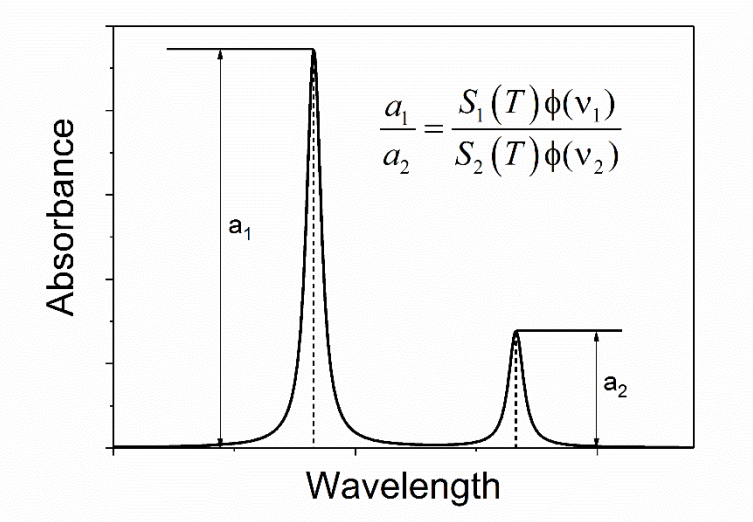

Figure 2.10: Absorbance ratio for two-line thermometry using fixed wavelength method.

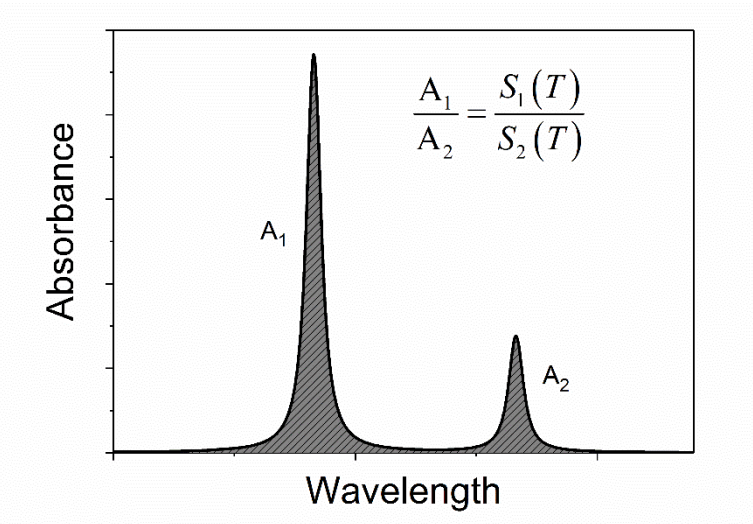

Figure 2.11: Absorbance ratio for two-line thermometry using scanned wavelength method.

3. Experiments

3.1. Shock tubes

In the framework of this thesis, experiments were conducted in two stainless-steel diaphragm-type shock tubes. Figure 3.1 shows the schematics of the two shock tubes (A, B) used in this study.

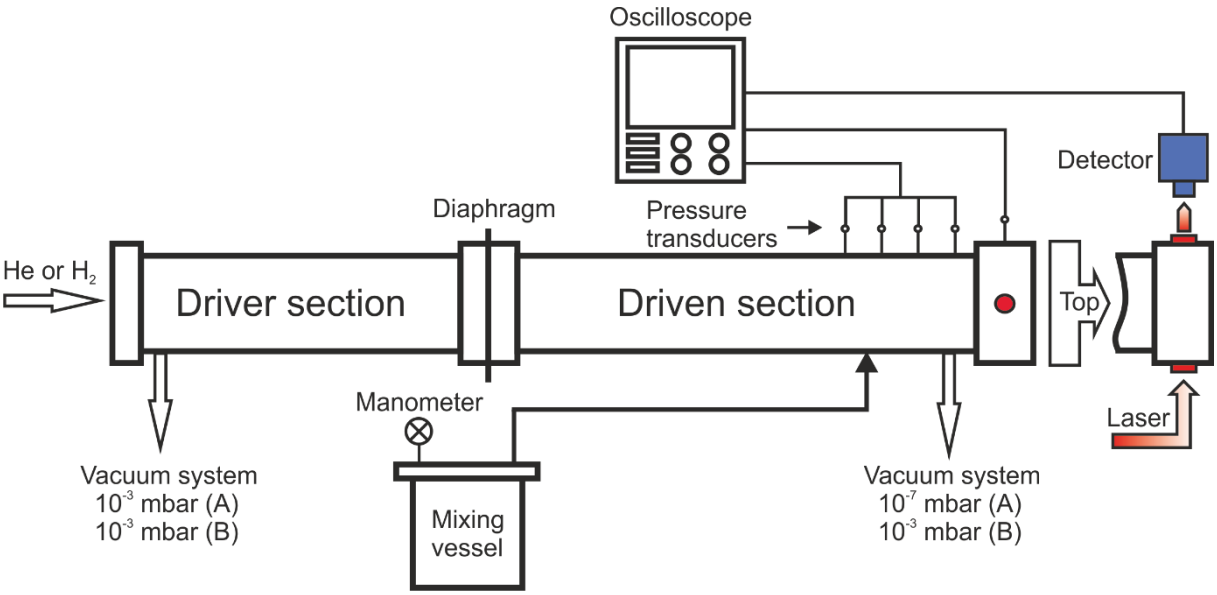

Figure 3.1: Schematics of the shock tube with laser absorption spectroscopy.

Shock tube A has a 3 m driver section and a 5.5 m driven section with an overall inner diameter of 80 mm. Aluminum diaphragms with 50–70 μm thickness were used to separate the driver from the driven sections. The sealing between the two parts of the shock tube is realized by using two Viton O-rings on both sides of the aluminum sheet guaranteeing a leakage rate of 10^{-6} mbar·l/s in the driven section. For the investigation of highly diluted ultra-pure test mixtures, a turbo molecular pump (Leybold Tobo361) is used for the evacuation of the driven section down to 2×10^{-7} mbar. The driver section is pumped by an oil pump (Pfeiffer, Duo 012A) down to 4×10^{-3} mbar.

To perform the experiment, the driven section is filled first with the test gas up to the pre-defined pressure p_1 and then the driver section is filled with driver gas through a magnetic valve until the diaphragm bursts. p_1 and the burst pressure p_4 of the diaphragm can be measured via a capacitance pressure gauge (Edwards NW35) near the end wall of the driven section and a manometer (Keller Mano 2000) at the end wall of the driver section, respectively. To generate

faster shock waves, lighter driver gases and thicker diaphragms can be applied. By using hydrogen as driver gas and 70 μm thick diaphragm, the test gas behind the reflected shock wave can reach post-shock conditions up to 2500 K and 2 bar.

To follow the thermodynamic states behind the shock wave, the driven section is equipped with an equidistant set of four pressure transducers (PCB model 112A03) with a distance of 150 mm between the transducer centers. The last transducer of this set is located 150 mm from the end plate of the driven section. The signals of the transducers are amplified with charge amplifiers (Kistler 5073) and recorded. By measuring the time interval between each adjacent transducer signal the shock wave velocity can be determined. One additional pressure transducer (Kistler 603A) is installed 20 mm upstream of the end wall to follow the pressure variation in the reaction zone. Two sapphire windows with 8 mm diameter are installed at 20 mm upstream of the end wall at opposite side of the driven section as accesses for optical diagnostics in the reaction zone, e.g., laser absorption spectroscopy in this study.

After each experiment, the shock tube is evacuated to 10^{-1} mbar and filled with nitrogen to atmospheric pressure before replacing the diaphragm. High-vacuum conditions in the shock tube can be reached again within one hour after reset.

Setup and operation of shock tube B are similar to shock tube A. A detailed description of this shock tube can be found in [12]. In brief, shock tube B has a 2.5 m driver section and 6.3 m driven section with an overall inner diameter of 80 mm. This tube is designed for investigations that possibly involve particle formation during the experiment, therefore a particle-tolerant pump is used. Both sides of the tube can be evacuated down to 1.8×10^{-3} mbar through a combination of a dry vacuum pump (Edwards QDP80) and a booster pump (Edwards, EH 500A).

Each shock tube is equipped with a 50-liter mixing vessel that can be evacuated down to 10^{-7} mbar before use. All the mixtures investigated in this work were prepared manometrically and allowed to homogenize over night before use. The mixture is filled into the respective driven section of the shock tube through a 6 mm inner diameter stainless-steel line connected near the end plate. To rule out uncertainties in the concentration due to adsorption of large molecules such as anisole and allyl phenyl ether on the metal surfaces, UV absorption measurements were carried out to determine the initial mixture concentrations in the shock tube for each experiment by dissolving the mixtures filled in the shock tube in *n*-hexane or ethanol. The gases (CO, H_2, He, Ar, etc.) used in the measurements were from Air Liquide and have purities > 99.99%. The

liquid chemicals (3 pentanone, anisole, benzene, etc.) used in the experiments come from Sigma-Aldrich and the purities are > 99.95%.

The triggering of the data acquisition for the whole experiment is accomplished by a pulse generator that releases TTL signal when the shock wave passes at the first pressure transducer downstream of the diaphragm section. All acquired signals are recorded in one 14-bit 4-channel oscilloscope (PicoScope 5442A). Figure 3.2 shows a data set obtained from a typical shock-tube experiment in combination with two-line absorption data. Time zero is set to the arrival of the reflected shock wave at the Kistler pressure transducer located 20 mm upstream of the end flanch of the driven section.

The acquired data in this thesis were post-processed using OriginLab. The calculation of the conditions behind incident and reflected shock waves as well as the simulation of the chemical kinetics were done with the software Chemical Workbench (Kintech Lab.).

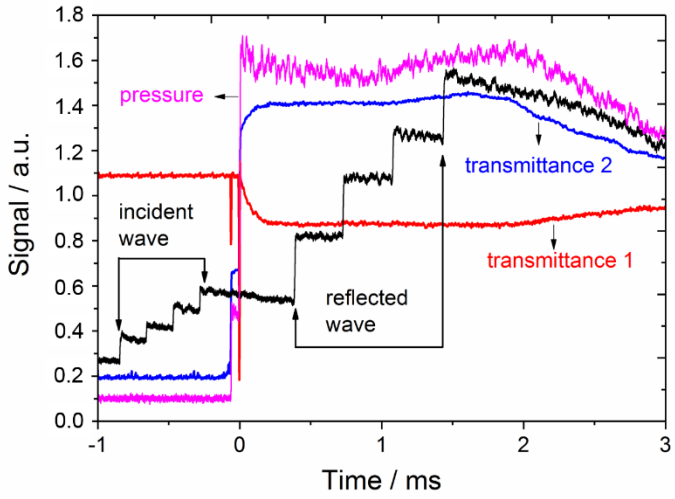

Figure 3.2: Data acquisition of pressures and laser signals during a typical shock-tube experiment.

3.2. Mid-IR CO sensor and validation of the two-line temperature measurement

Carbon monoxide (CO) is a main intermediate and product of hydrocarbon combustion. Its concentration can be interpreted to indicate the efficiency of the combustion system. The diatomic structure of CO leads to one rotational and one vibrational mode, and shows strong absorption in the infrared region. The absorption line strengths (from HITRAN database [62]) of the CO transitions are plotted as a function of the wavelength in the range 1.5–5.5 µm at 1 bar and 1600 K in Figure 3.3. The three strongest absorption regions of CO correspond to its different rovibrational bands, i.e. the fundamental band near 4.7 µm, the first overtone band near 2.3 µm, and the second overtone band near 1.55 µm. Many works have used transitions in both

overtone bands [21, 63]. In comparison to the first and second overtone bands, the absorption strength of the fundamental band is stronger by approximately two and four orders of magnitudes, respectively, and is thus providing improved sensitivity at 4.7 µm for many applications where the respective concentration of CO is too low or/and the path length is too short for measurements at 1.5 or 2.3 µm.

Recent works demonstrated the advantage of quantum cascade (QC) lasers that can provide high output power, narrow line-width, and single-mode operation [64]. By extending the accessible wavelength range up to 6 µm, transitions in the strong fundamental band of CO can be assessed. Ren et al. [24] demonstrated the first application of a temperature and CO concentration measurement for kinetics study of methyl formate by cw DFB-QC laser-based mid-IR absorption spectroscopy. The reported line pairs showed high temperature sensitivity up to 3000 K and tens of ppm detection limit for the CO concentration. In this work, new line pairs of CO transitions have been selected and validated because higher CO sensitivity is required at 900–1100 K. Under the high demand of flexibility and mobility of the new absorption measurement strategy, a fiber-based thermometry system has been further developed within the frame of this thesis.

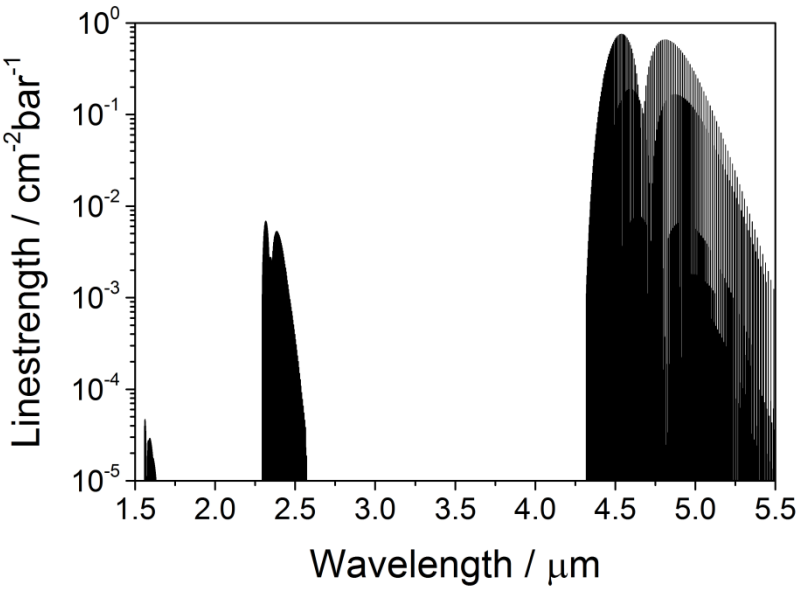

Figure 3.3: Absorption line strengths of CO transitions as a function of wavelength at 1.5–5.5 µm at 1 bar and 1600 K (from HITRAN 2004 database [62]).

3.2.1. Line selection

A molecule can have several thousands of absorption transitions. Even if the wavelength range for the selection can be limited to a certain vibrational band, there still exist hundreds of rotational candidate lines. In order to choose proper line pairs for the environment to be investigated, selection rules need to be considered.

First, the selection of candidate lines should be limited to the spectral region provided by the emission of the laser. For the fundamental band of CO, QC laser technology provides access to the range between 4.5 to 5.0 μm.

Second, in order to obtain sufficient signal-to-noise ratio (SNR) during the measurement, the candidate lines should have line strengths that are strong enough over the interested temperature range. However, since transitions in the fundamental band of CO show overall strong absorption, too strong lines should not be chosen to avoid signal saturation. Generally, the ideal absorbance over the interested temperature range of the candidate lines is between 0.01 to 2.

Third, according to equation (2.56), larger difference in the lower-state energies of both lines leads to an increased temperature sensitivity. However, transitions with high E'' provide weak absorbance and thus result in small SNR. In order to obtain the optimum measurements, the SNR and the temperature sensitivity must be carefully balanced for a given situation

Fourth, H_2O and CO_2 cause strong absorption near the 4.7 μm region as well. To maintain the accuracy of the measurements, interferences from transitions of H_2O and CO_2 have to be avoided when line pairs for CO are selected. Furthermore, at high pressure, interferences of neighboring transitions from CO should also be minimized.

For the identification of candidate transitions, absorption parameters such as line strength and lower-state energy provide the necessary input. Also, the line shape and the broadening characterizations of the transitions must be known. In the initial step of the selection, HITRAN [65] and HITEMP [66] databases are used. The HITRAN (high-resolution transmission) molecular absorption database is a compilation of spectroscopic parameters from various molecules that can simulate the transmission and emission of the light in the atmosphere. It provides common spectroscopic parameters of the transitions including the line strength S [$cm^{-1}/(mol \cdot cm^{-2})$], the air-broadening half width γ_{air} [$cm^{-1}atm^{-1}$], the self-broadening half width γ_{self} [$cm^{-1}atm^{-1}$], the temperature-dependent exponent n_{air}, and the lower-state energy E'' [cm^{-1}]. More than 7 mil-

lion spectral lines for 47 different molecules and 120 isotopologues are contained in the HITRAN 2012 database [65]. However, most of the spectroscopic parameters in the HITRAN database are measured at 296 K because they were compiled for atmospheric purposes, for some special transitions, the temperatures are varied in the range 200–350 K. Many spectral lines that appear at high temperatures are missing and these are pre-requisite for e.g., high temperature applications such as combustion processes, exhaust plumes, etc. The HITEMP (high temperature molecular) database, however, contains more spectral lines at higher rotational levels for many intermediates and products in combustion such as H_2O, CO_2, CO, NO, and OH. As a comparison, the HITEMP 2010 database [66] contains 113,631 CO lines while the HITRAN 2012 database contains only 4,606 lines.

In this study, three QC lasers providing the frequency ranges of 2052.80–2061.90 cm^{-1}, 2103.49–2113.27 cm^{-1}, and 2188.06–2191.79 cm^{-1} were acquired from Alpes Lasers SA, Adtech Optics, and Hamamatsu Photonics, respectively. Candidate absorption lines of P(20) from Alpes laser and R(21) from Hamamatsu laser are centered at 2059.91 and 2191.50 cm^{-1}, respectively, and have been suggested in Ref. [24] for fixed-wavelength absorption spectroscopy. The simulated absorption spectral of a 0.1% CO/1% H_2O/1% CO_2 mixture based on the HITRAN 2012 database [65] for both P(20) and R(21) under typical condition for combustion at 1 bar and 1600 K are plotted as a function of the frequency in Figure 3.4a. The line-broadening of both lines at 1600 K and pressures of 1, 2, and 3 bar of in a mixture that contains 0.1% CO are compared in Figure 3.4b. The calculated line strengths at the center of both transitions are plotted versus temperature from 300 to 3000 K and the inferred temperature sensitivity from the line strengths ratio at 1000–3000 K are shown in Figure 3.5 a and b, respectively.

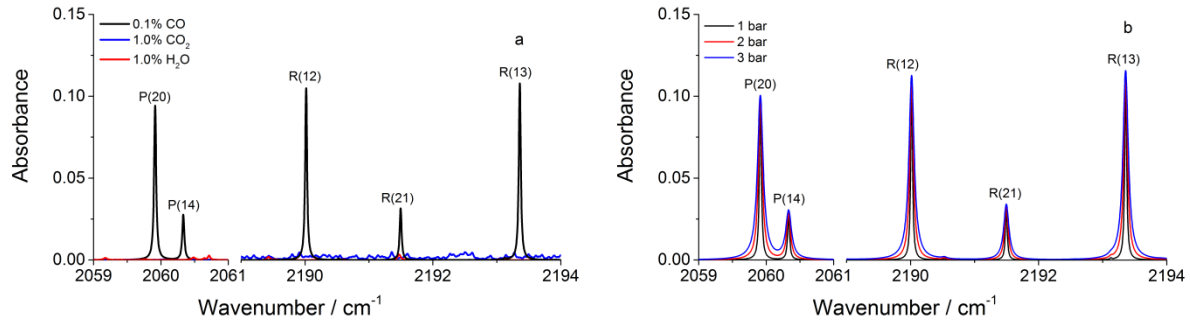

Figure 3.4: a) Simulated absorption spectra near P(20) and R(21) in a mixture with 0.1% CO, 1% H_2O, and 1% CO_2 in air under typical shock tube conditions of 1600 K and 1 bar; b) simulated absorption spectra of 0.1% CO at 1600 K and 1–3 bar (L = 10 cm).

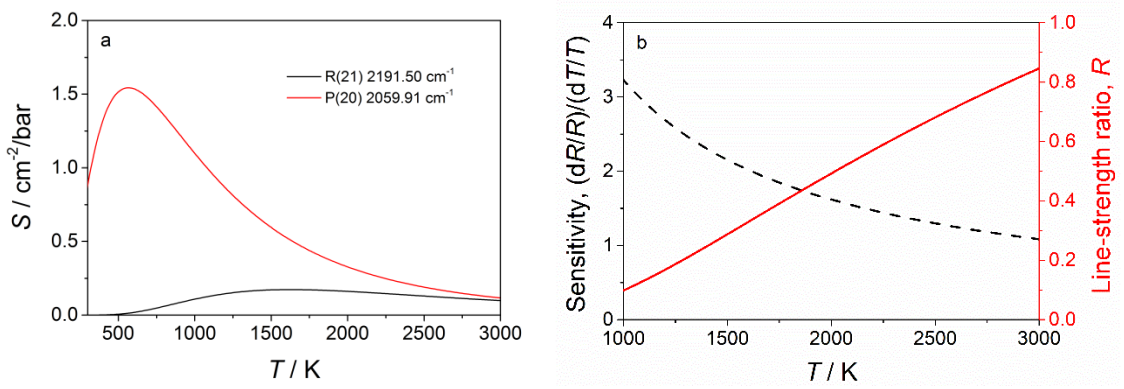

Figure 3.5: a) Calculated line strengths of lines P(20) and R(21) at 300–3000 K; b) temperature sensitivity and line strength ratio of line pair P(20)/R(21) between 1000 and 3000 K.

Both lines P(20) and R(21) show strong absorption for a mixture contains 0.1% CO, 1% H_2O, and 1% CO_2. The simulation shows that the interferences from H_2O and CO_2 are negligible. P(20) has a neighboring CO line P(14) that centers at 2060.33 cm^{-1} that is very close to 2059.91 cm^{-1}, the pressure broadening of P(14) shows notable influence on the absorption of P(20) at 3 bar. For measurements at pressure higher than 3 bar, the interference from P(14) must be considered and subtracted from the obtained absorption of P(20). R(21) also has an adjacent CO absorption line R(12) that centered at 2190.02 cm^{-1}, the broadening effect of R(12) on the R(21) can be neglected up to 8 bar due to their relative larger $\Delta\nu$.

As shown in Figure 3.5a, the line strength of P(20) is relative strong at room temperature and reaches its peak value at 600 K. R(21) has its first noticeable absorption strength at 500 K and reaches its peak value at 1600 K. The temperature sensitivity inferred from the line strength ratio of P(20) and R(21) shows a value higher than 1 up to 3000 K which infers that this line pair can be used for accurate temperature sensing at elevated temperatures e.g., between 1000 and 3000 K. However, the "interference free" absorption measurement of P(20) due to the line-broadening of P(14) is limited up to 3 bar and the relative weak line strength of R(21) at temperature below 1000 K can lead to low SNR of absorption especially with low CO concentration. Hence, a new candidate line that compensates for these limitations is provided by the Adtech laser, which enables the access of a different frequency range.

The absorption of candidate CO lines in the tuning range of the Adtech laser at 1600 K and 1 bar near 2108 cm^{-1} is simulated based on HITRAN 2012 [65] and illustrated in Figure 3.6. Absorption lines of H_2O and CO_2 are also simulated and compared at the same conditions. There are three $v'' = 0$ transitions of CO, i.e. P(8), P(9), and P(10) that are centered at 2111.54, 2107.42, and 2103.27 cm^{-1}, respectively, and two $v'' = 1$ transitions of CO, i.e. R(9) and P(2)

that are centered at 2105.26 and 2109.13 cm^{-1}, respectively. All the five CO lines are well isolated from each other with an average $\Delta\nu$ of 2 cm^{-1}. However, by considering the absorption lines of H_2O and CO_2 in the same region, P(8) is the most convenient line that has negligible interference from neighboring transitions. To evaluate the potential line pair using P(8), the spectroscopic parameters of line P(8) as well as P(20) and R(21) from HITRAN 2012 [65] are summarized in the table 3.1.

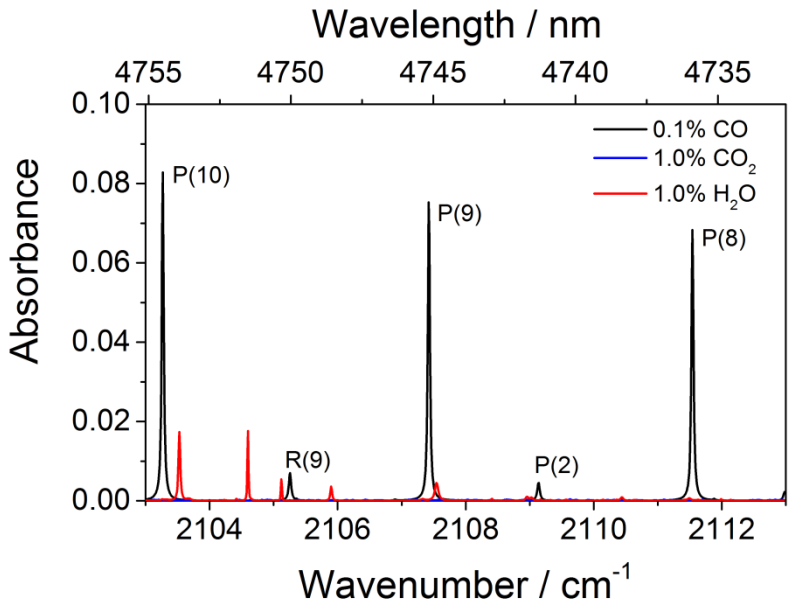

Figure 3.6: Simulated spectra near P(8) transition of 0.1% CO, 1.0% H_2O, and 1.0% CO_2 in air under typical shock-heated condition for 1600 K and at 1.0 bar (L = 10 cm).

Table 3.1: Spectroscopic parameters from HITRAN 2012 database [65] of the candidate lines for the measurements of temperature and CO concentration

Laser	Line	Wavelength [nm]	Wavenumber [cm^{-1}]	S(296K) [cm^{-2}/atm]	E" [cm^{-1}]
Alpes	P(20)	4854.58	2059.91	0.876	806.38
Hamama-tsu	R(21)	4563.08	2191.50	4.32×10^{5}	3022.09
Adtech	P(8)	4735.88	2111.54	9.225	138.4

The line strength of P(8) at room temperature is about an order of magnitude stronger than that of P(20) and the lower-state energy of P(8) is lower than both P(20) and R(21). According to equation (2.56), the large differences of lower-state energies between P(8) and P(20) as well as

P(8) and R(21) would be beneficial for two potential line pairs for sensitive temperature measurement. The line strength of P(8) over the temperature range of 300–3000 K is calculated and compared to those of P(20) and R(21) in Figure 3.7a, the inferred temperature sensitivities of both line pairs based on the line strength ratios are illustrated in Figure 3.7b.

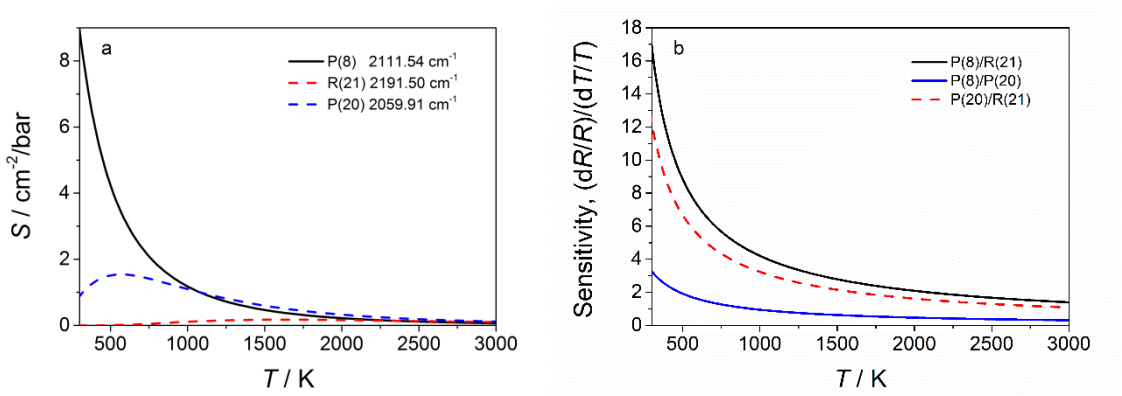

Figure 3.7: a): Calculated line strength of P(8) transitions compared with P(20) and R(21) in the temperature range between 300–3000 K; b): calculated temperature sensitivities of line pairs P(8)/R(21) and P(8)/P(20) in comparison to P(20)/R(21).

P(8) exhibits a decreasing line strength with increasing temperature. The line strength of P(8) is stronger than P(20) at temperatures between 300 and 1100 K but becomes weaker/similar than P(20) and R(21) from 1100 to 2340 K, respectively. Therefore, P(8) can provide more sensitive detection of CO compared to P(20) at temperatures below 1100 K. The temperature sensitivity of the line pair P(8)/P(20) and P(8)/R(21) was also evaluated and reveals that the line pair P(8)/P(20) is optimal for low-temperature measurements between 300 and 950 K ($(dR/R)/(dT/T)>1$) while the P(8)/R(21) has a much broader temperature sensitivity up to 3000 K. The line pair P(8)/R(21) is suitable for most high-temperature processes whereas the P(8)/P(20) is more practical for the target gases at relative low temperature such as exhaust gas of gas turbines and internal combustion engines. In this study, line pairs P(20)/R(21) and P(8)/R(21) were applied in different gas-phase kinetics studies in the shock tubes.

3.2.2. Line characterization

The HITRAN database [62, 65, 67] provides the fundamental spectroscopic parameters for many relevant molecules. However, the broadening coefficients and the corresponding temperature-dependent coefficients provided in HITRAN are obtained only in air. In most gas-phase kinetics studies in shock tubes, however, argon instead of air is usually used. Therefore, argon broadening coefficients for each selected line must be investigated. Furthermore, the line

strengths at elevated temperatures also need to be validated as the accuracy of inferred temperature and concentration dependent strongly upon it.

Relaxation time

The rapid temperature increase in a shock tube initially increases the translational temperature (T_{trans}), the new distribution of molecular velocities may instantaneously no longer follow the Maxwell-Boltzmann law. To re-establish the Boltzmann distribution in all degrees of freedom (i.e. thermal equilibrium at the new temperature), the energies of the rotational and the vibrational degrees of freedom have to be redistributed. The procedure results in a further temperature of the respective degrees of freedom change due to the energy transfer between translation, rotation, and vibration. These equilibration processes are named as rotational and vibrational relaxation. Rotational relaxation usually takes place in a very short time normally about 10^{-9} s and can be neglected in shock-tube experiment whereas the time of vibrational relaxation depends strongly on the molecular structure and can be up to several milliseconds which is the typical observation time for many gas-phase kinetics investigations.

CO can be considered as an anharmonic oscillator due to its diatomic molecular structure. The vibrational energy E_v of rapidly heated CO molecule is much higher than the vibrational energy E_v^* at T_{trans} and results in a very inefficient vibrational equilibrium process. The relaxation time of an excited CO molecule is relatively long. One common solution to reduce the relaxation time is to introduce an efficient collisional partner into the gas mixture. By using a molecule-specific empirical correlation and a mixing rule that is developed by Millikan and White [68], the relaxation time of CO/Ar mixtures with different amount of H_2 or He can be calculated following Eqs. 3.1–3.2 and is shown in Figure 3.8.

$$(\tau_{mix})^{-1} = \phi(\tau_{B-B})^{-1} + (1-\phi)(\tau_{B-A})^{-1} \tag{3.1}$$

$$p\tau_v = \exp\left[A(T^{-\frac{1}{3}} - 0.015\mu^{\frac{1}{4}}) - 18.42 \right] \tag{3.2}$$

Here, τ is the vibrational relaxation time, ϕ is the mole fraction, p is the pressure, A is the pre-factor, and μ is the reduced mass of the collision pair.

The relaxation time generally decreases with increasing temperature. The long relaxation time of CO can be strongly reduced by the addition of small amount of H_2 or He. H_2 exhibits a more efficient acceleration to the relaxation time compared to the same amount of He. To achieve

the same efficiency as H_2, the concentration of He need to be increased by a factor of 10. The relaxation time decreases also with increased concentration of the collider. With 20% He in the gas mixture, the relaxation time of CO can be reduced to 100–10 µs over the temperature range from 1000–2000 K.

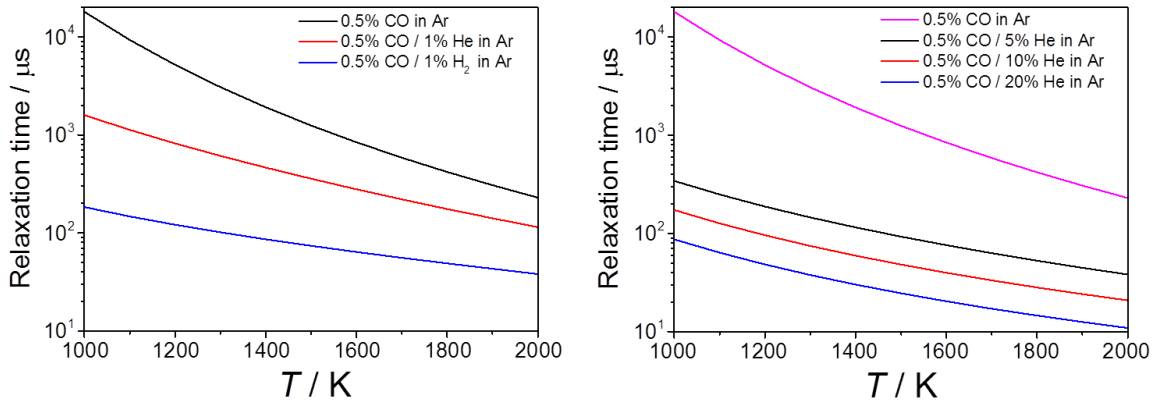

Figure 3.8: Calculated vibrational relaxation time at p = 1.5 bar for CO/Ar, CO/H_2/Ar, and CO/He/Ar mixtures.

Line strength and argon broadening coefficient

In this study, the line strengths of P(8), P(20), and R(21) were measured within temperatures of 900–2400 K and compared to the calculated values based on the HITRAN 2012 database [65]. The argon broadening coefficient of P(8) was also measured at temperature between 900 and 1700 K while that of P(20) and R(21) have been validated by Ren et al. [24]. The scanned-wavelength absorption spectroscopy was used for these measurements. To determine the argon broadening coefficient and the line strengths accurately, non-reactive CO/Ar mixtures were used. Due to the short observation time in shock tubes (~2 ms) and the long induced vibrational relaxation for CO, small amount of 2% H_2 was added into the mixture to lessen it.

A schematic of the experimental setup is depicted in Figure 3.9. The QC lasers are thermoelectrically cooled and housed with collimation optics in a sealed laser housing (HHL). Additionally, a water-cooled heat sink is installed to the HHL housing to achieve additional stable laser performance. The wavelength of the laser is tuned by varying the operating temperature or/and current which are controlled by a combined temperature-current controller (Arroyo 6350). A function generator is connected to the laser controller to generate a linear ramp of current which can rapidly tune the laser wavelength to cover the desired absorption feature. Three CaF_2 beam splitters are used to split the collimated laser beam (20–100 mW) into four arms before the light goes through the shock tube. The first beam passes through a 10 cm long solid germanium

etalon that has a free spectral space (FSR) of 0.016 cm^{-1}, The signal I_{etalon} behind the etalon is used for converting the received signals from time domain into frequency domain. The second beam goes through the ambient air and serves as reference intensity I_{ref}, which is used later to calculate the baseline of the scanned waveform. The third beam is directed into a reference cell that is filled with a 100 mbar 0.1% CO/Ar mixture, the desired line feature can be checked prior to each measurement. For P(8) and P(20) which strongly absorbs at room temperature, a 10 cm stainless-steel cell is used; for R(21) that barely absorbs at room temperature, a multi-pass White cell [69] with effective absorption path length of 20 m was used and heated to 70°C to obtain a strong enough absorption signal. The last beam propagates through the test gas with a 8 cm path length in the shock tube with transmitted intensity I_t. All the signals are received by TE-cooled IR photovoltaic detectors (VIGO) with 1 MHz bandwidth. A narrow bandpass filter (NBP) (FWHM < 200 nm) was installed in front of each detector to block the unwanted interferences from ambient light and the emissions from the shock-heated gases during the experiments.

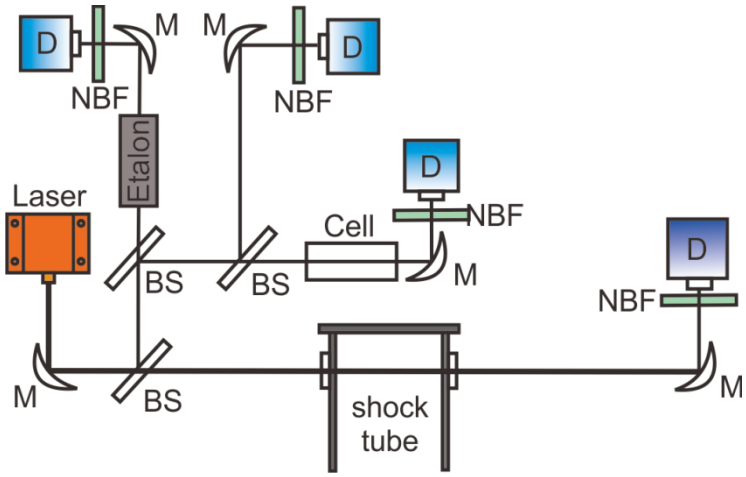

Figure 3.9: Experimental setup for the measurement of spectroscopic parameters of selected lines in the shock tube; M: mirror; BS: beam splitter; NBF: narrow bandpass filter.

Typically, the lasers are tuned at a frequency of 5 kHz to obtain sufficient points for the data evaluation. A scanned wavelength range of 0.5 cm^{-1} can be achieved and interested line feature can be covered. The data acquisition is triggered by the first pressure transducer located 58 cm from the endwall of the driven section. For each measurement, the signals of the laser, i.e. I_{ref}, I_t, and I_{etalon} and the signals of the pressure transducers, are recorded for the analysis of the spectroscopic parameters. To increase SNR each measured point I_t is usually averaged three times.

Figure 3.10a shows the raw data of a typical experiment for a high-temperature line-strength and argon-broadening measurement of CO. The laser is scanned over the R(21) line at 2191.50 cm^{-1} at 1768 K and 1.65 bar with a mixture of 0.5% CO/2% H_2/Ar. The absorbance of each scanned I_t is calculated from Eq. 2.33 with a baseline I_0 generated from I_{ref}. The spectral absorbance was then plotted as a function of wavenumber calibrated using the etalon trace I_{etalon} in Figure 3.10b. A best-fit Voigt profile of the measured spectral is also plotted, and excellent agreement with the measurement was found. The peak-normalized residual values are less than 0.5% over the entire absorption feature.

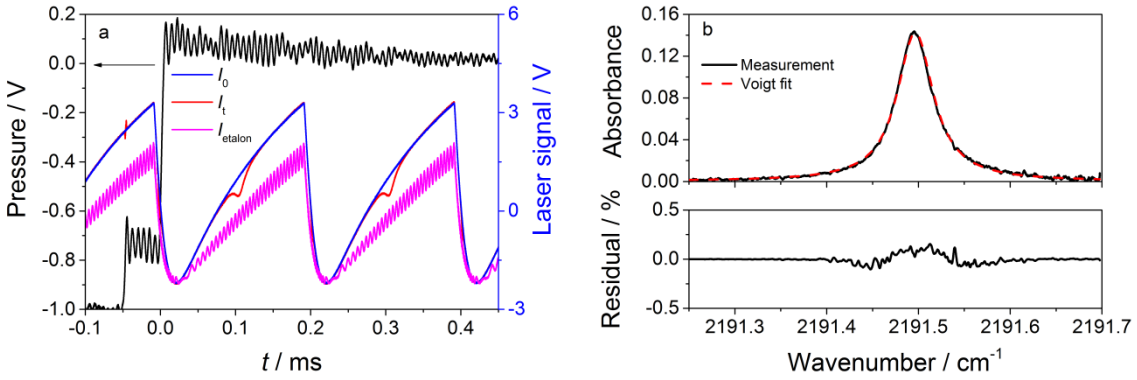

Figure 3.10: a) Measured raw-data traces (pressure, incident and transmitted laser intensity, etalon) of R(21) transition at 2191.50 cm^{-1} with 0.5% CO/2% H_2/Ar mixtures at 1768 K and 1.65 bar, scanning frequency is 5 kHz; b) the inferred absorbance line shape of R(21) transition and its best-fit Voigt profile with overall residual less than 0.5%.

The line strength at a selected temperature for the corresponding line can be then inferred from the integrated absorbance area of the fitted Voigt profile using Eq. 2.36. The measured values for the line strengths of P(8), P(20), and R(21) at temperature of 900–2400 K behind the reflected shock waves are summarized in Figure 3.11a. The calculated line strengths using Eq. 2.27 with the values for S_{296K} and E'' from the HITRAN 2012 database [65] are also plotted for comparison. Excellent agreements are found between the measurements and the calculations with a maximum deviation of 2%.

The argon broadening coefficient for P(8) can be subsequently calculated from the obtained line strength using Eq. 2.33 assuming that the self- and H_2-broadening of the CO are negligible due to their relative low concentrations of 0.5% and 2%, respectively, compared to the concentration (97.5%) of Ar. Figure 3.11b illustrates the measured argon broadening of P(8) as a function of temperature at 900–1700 K. The $2\gamma_{CO\text{-}Ar}(296K)$ can be measured at room temperature prior to the arrival of incident shock and the corresponding temperature dependent coefficient

n of P(8) can be then calculated by the best fit procedure following Eq. 2.43. The measured $2\gamma_{\text{CO-Ar}}(296\text{K})$ and *n* of P(8) are summarized in Table 3.2 together with the values of P(20) and R(21) obtained from Ren et al. [24]. The measurements show good agreement with the literature values from Sinclair et al. [51].

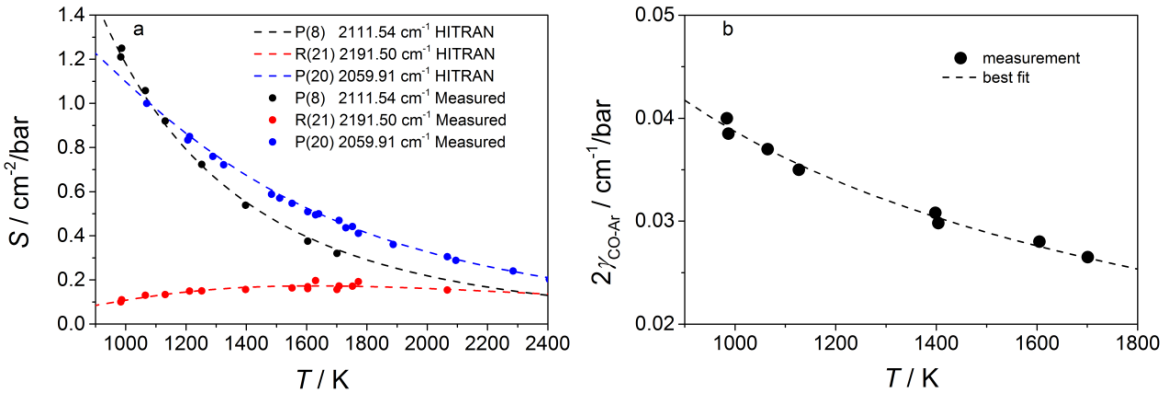

Figure 3.11: Summary of the measured line strengths and argon broadening coefficient for the selected CO transitions; a): comparison of the measured line strength of P(8), P(20), and R(21) at high temperatures with HITRAN database [66]; b) measured argon broadening coefficient of P(8), dashed line is the two-parameter best fit following Eq. 2.43.

Table 3.2: Line strengths and argon-broadening coefficients for the selected CO lines. P(8) was measured in this study, R(21) and P(20) were taken from Ren et al. [24]. Uncertainties of the measured values are given in parentheses. Argon-broadening coefficients of P(8) are extrapolated based on the experimental data over the temperature range of 900–1800 K.

Line	$S_{296\text{K}}$ / $\text{cm}^{-2}\text{atm}^{-1}$		$2\gamma_{\text{CO–Ar}}(296\text{K})$ / $\text{cm}^{-1}/\text{atm}$		*n*
	HITRAN [65]	Measured	Sinclair et al. [51]	Measured	Measured
R(21)	4.32×10^{-5} (2–3%)	–	0.078 (8%)	0.072±0.007 [24]	0.571±0.012 [24]
P(20)	0.867 (2–3%)	0.872 (2.5%) [24]	0.089 (10%)	0.083±0.011 [24]	0.639±0.024 [24]
P(8)	9.225 (2–3%)	9.259 (3%)	0.094 (8%)	0.092 (5%)	0.71 (5%)

3.2.3. Sensor setup

As discussed in section 3.1, the line pairs P(20)/R(21) and P(8)/R(21) were selected for gas-phase kinetics investigations at elevated temperature. The spectroscopic parameters of the selected lines were determined using the scanned-wavelength direct absorption spectroscopy; however, this method is unable to capture the rapid change of gas properties in chemical reactions due to its limited scanning frequency. Hence, fixed-wavelength direct-absorption spectroscopy was set up and adapted to the shock-tube facilities to precisely capture the kinetics information.

Two-line absorption thermometry

Figure 3.12 shows a schematic of the sensor setup coupled to the shock tube. In order to obtain optimal beam performance, the lasers are placed on either side of the tube and both laser beams share sapphire windows with 8 mm diameter on the horizontal level of the driven section. Light beam emitted from the laser at the wavelength of P(20) is focused into the center of the shock tube through a concave mirror and then collimated again by a second concave mirror having the same focal length that is placed symmetrically at the opposite side of the shock tube. The collimated light beam is then separated into two unequal parts by a CaF_2 beam splitter; 10% of the original beam is focused into the TE-cooled IR photovoltaic detectors (VIGO) to avoid saturation of the detector. A bandpass filter (4.855 µm±88 nm) was installed in front of the detector to discriminate the signal against thermal emission from the shock-heated gases. The other part (90%) of the beam is guided through a 10 cm long well-sealed stainless-steel cell filled with 100 mbar of a 1% CO/Ar mixture at room temperature to identify the peak absorption of CO. The optical arrangement of the light beam emitted from the laser at the wavelength of R(21) is similar to P(20), besides that for the wavelength adjustment, the light beam was guided through a White cell that is set to 20 m path length and filled with pure CO. Moreover, a bandpass filter of 4.565 µm±200 nm is installed in front of the detector for R(21).

Due to limited space on the optical table, it was not possible to place and operate a third QC laser for simultaneous measurements. To apply the measurements using the line pair P(8)/R(21), the laser for P(20) was therefore replaced by the laser that emits light at the wavelength of P(8) and the corresponding bandpass filter was changed to 4.736 µm±100 nm. Furthermore, due to the geometric restrictions of the optical access mentioned before, the beams of both lasers were not perfectly perpendicular to the longitudinal axis of the shock tube, which, resulted in broader schlieren. This effect becomes critical for measurements involving ultra-fast reactions, because

the information in the first 0–50 µs cannot be fully captured. Moreover, slight deviation (~1 mm) in the path lengths in comparison to the inner diameter of the shock tube are present, and this uncertainty in the path length must be taken into account for data evaluation.

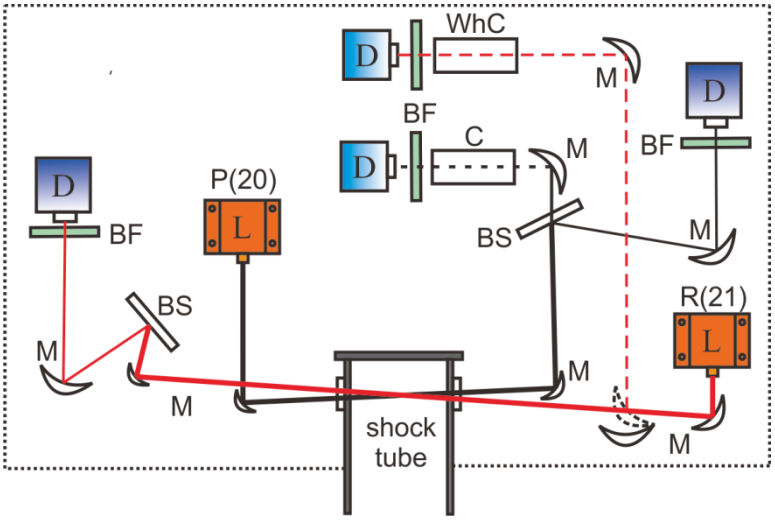

Figure 3.12: Experimental setup of the free space two-line absorption thermometry coupled with the shock tube for time-resolved CO and temperature measurements; L: laser, D: detector, M: mirror, BS: beam splitter, BF: bandpass filter, C: cell, WhC: White cell.

Fiber-based multi-line spectrometry

To improve the performance and flexibility of the setup for two-line absorption thermometry and to overcome the complexities of the setup showed in Figure 3.12, a fiber-based multi-line spectrometry was designed and constructed. A schematic of the improved experimental setup is shown in Figure 3.13. The optical arrangement of the spectrometry is divided into two parts, i.e. the sender and the receiver. Both parts are placed on opposite sides of the shock tube. On the sender side, one 3-to-1 InF_3 optical fiber combiner (Thorlabs) with 95% transmission in the 0.5–5 µm region was used to couple the beams from the three QC lasers into one fiber. The combined beam is then directed through the shock tube via collimation lenses. The outcoming laser beam was then detected by the detectors on the receiver side. Before that, the merged beam is first separated into three directions through two beam splitters (CaF_2, 50/50) and then, each beam is detected by a VIGO detector. Bandpass filters at 4.855 µm±88 nm, 4.526 µm±80 nm, and 4.736 µm±100 nm for P(20), R(21), and P(8), respectively, are installed in front of each detector to cut-off perturbing wavelengths. To tune the laser wavelength to the desired transitions prior to each experiment, the wavelength of each laser beam is monitored either by directing the incident beams into a free-space mid-IR wavelength meter (Bristol 721) installed on the sender side or into a cell containing diluted CO on the receiver side.

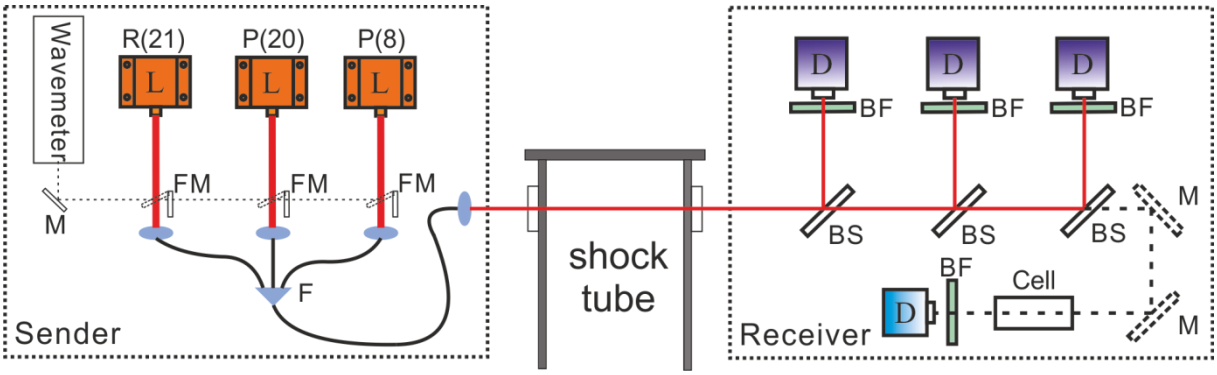

Figure 3.13: Schematics of the fiber-based multi-line spectrometer coupled with the shock tube for time-resolved CO and temperature measurements; L: laser, D: detector, M: mirror, FM: flip mirror, F: fiber, BF: bandpass filter, BS: beam splitter.

The fiber-based multi-line spectrometry provides higher flexibility in comparison to the free space setup. Once the desired line pair is set, the third laser can provide additional measurement combinations. On the one hand, multiplex can help to identify for example background due to broadband signal attenuation during soot formation or non-resonance interference from unknown molecule near the transition of interest. In practice, the third laser can be tuned to an off-line position where no CO absorption occurs. On the other hand, the setup can be used to monitor other species of interest such as CO_2, H_2O, and CH_4 near 2.7, 1.5, and 3.39 µm, respectively. Moreover, the output beam out of the InF_3 fiber can be precisely collimated with the same set of lenses without further alignment to obtain optimal and consistent path lengths for all laser beams.

3.2.4. Sensor validation in the shock-tube experiment

The CO concentration and temperature measurements using the fixed-wavelength method with the line pair P(8)/R(21) were first validated with non-reactive shock-heated gases. A test mixture of 0.5% CO/2% H_2/Ar was used. The test gases were shock-heated to temperatures between 900 and 1800 K at pressures between 1.0 and 1.6 bar. Figure 3.14 shows an example time-history of absorbance signals during a typical shock-tube experiment at 1252 K and 1.1 bar. The three plateau values of the P(8) signal indicate the absorbances at conditions in front of the incident shock wave, behind the incident shock wave, and behind the reflected shock wave, respectively. The two large spikes are due to the schlieren effect as a result of the passage of the shock wave through the measurement plane. With the addition of H_2, the CO is fully relaxed within ~0.1 ms after the arrival of the reflected shock wave. As the vibrational temperature equilibrates, the absorbance of P(8) decreases while that of R(21) increases from zero to its plateau value because both lines have an inverse temperature dependence of their line strengths.

The temperature of the shock-heated gases can be inferred from the ratio of the laser absorbance following the Eq. 2.55 and the absolute CO concentration can be subsequently determined using Eq. 2.37. A typical measured temperature–time history is plotted in Figure 3.15. The average measured temperature over 0.1–1.5 ms is 1237K with a standard deviation of 15 K that shows excellent agreement with the calculated value of 1252 K. Additional detailed temperature measurements can be found in Appendix 8.1. Figure 3.16 summarizes the measured temperatures behind reflected shock waves for a wide range of conditions compared with the calculated ones from shock wave velocities, the inferred CO concentrations are also compared to the known values. The measured and calculated temperatures show very good agreement (within 1.8%) over the tested temperature range 900–1800 K, and the measured CO mole fractions agree with the known value within 2%. The results demonstrate the feasibility and the accuracy of the pair P(8)/R(21) for temperature and CO concentration measurements at practical conditions.

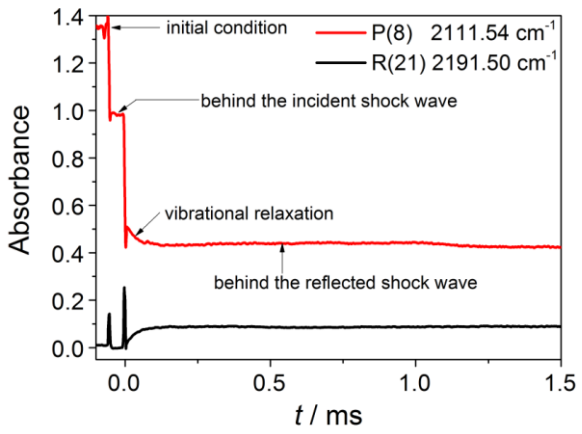

Figure 3.14: Typical absorbance-time histories of P(8) and R(21) of 0.5% CO/2% H_2/Ar mixture at T_5 = 1252 K and p_5 = 1.1 bar.

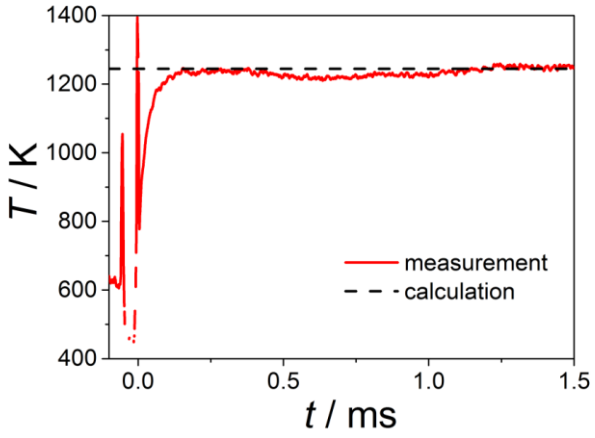

Figure 3.15: Typical measured temperature–time history compared with the calculated T_5.

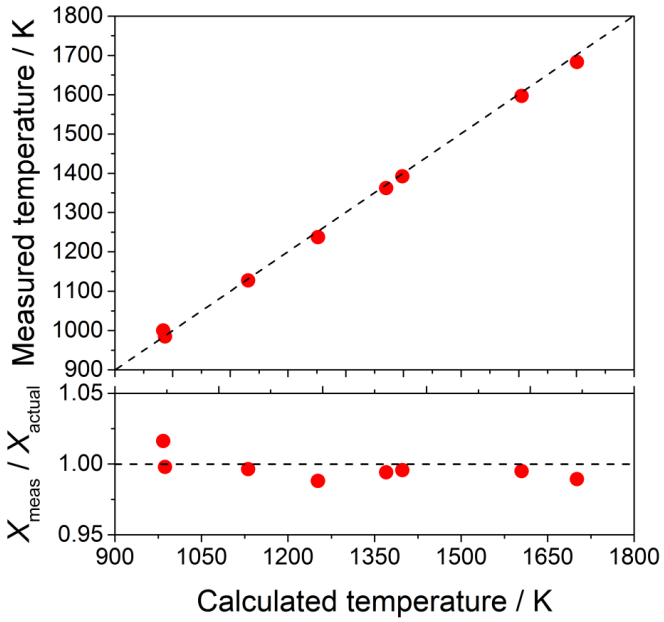

Figure 3.16: Validation measurements for the CO absorption line pair P(8)/R(21) using fixed-wavelength direct absorption with a mixture containing 0.5% CO/2% H_2/Ar; points: measurements, dashed lines: ideal values.

Decomposition of 3-pentanone

Amongst other ketones (e.g., acetone) 3-pentanone ($C_5H_{10}O$) has gained a large importance as a promising fluorescence tracer in fuel/air mixing studies based on laser-induced fluorescence (LIF) and as a component of next-generation biofuels. The use of 3-pentanone in both applications (tracer and fuel) depends critically on the knowledge of its pyrolysis and oxidation kinetics. The temperature and pressure dependence of the LIF signal from the tracer has been studied in detail [70]. Moreover, several chemical kinetics mechanisms were developed to describe the oxidation and pyrolysis of 3-pentanone by different groups [71-73].

The main pathway of 3-pentanone decomposition is $C_2H_5COC_2H_5(+M) = C_2H_5 + C_2H_5CO(+M)$, where the propionyl radical (C_2H_5CO) decomposes subsequently into C_2H_5 radical and CO. Therefore, the time-dependent CO concentration profile during 3-pentanone pyrolysis as well as oxidation can provide an excellent target to constraint the mechanism validation [71, 72]. In previous studies [71-73], mechanisms were validated first against ignition delay times of $C_5H_{10}O/O_2$ mixtures measured in a shock tube in the temperature range 1250–1850 K at 1 bar and for equivalence ratios of 0.5–2.0. Laminar flame speeds of $C_5H_{10}O/O_2$ mixtures at 1 bar over an equivalence ratio range from 0.75 to 1.45 were also measured in a spherical bomb and compared to the modeling. Good agreements were found for both ignition delay time and laminar flame speeds [73]. Furthermore, time-dependent OH, CO, CH_3, and H_2O mole fractions

have been measured behind shock waves over a temperature range of 1277–1678 K at 1.6 bar for equivalence ratios of 0.5, 1.0, and 1.5. The validation against the mechanism from [71] was utilized to develop an improved model containing 13 species and 61 reactions that predicts the CO mole fraction excellently [72]. However, there is no time-resolved temperature measurement for the mechanism validations. Therefore, the high-temperature pyrolysis and oxidation of 3-pentanone was selected as a benchmark to demonstrate the feasibility of thermometry based on the CO line pair P(8)/R(21) in a kinetics study.

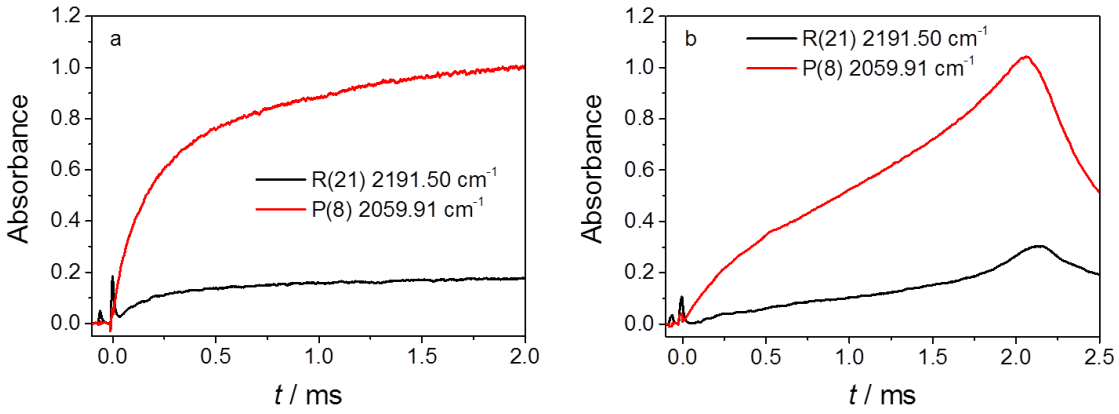

Figure 3.17: Typical absorbance–time histories of CO from P(8) and R(21) in test mixtures a): 1% $C_5H_{10}O$/Ar at T_5 = 1275 K and p_5 = 1.25bar, b): 0.285% $C_5H_{10}O$/2% O_2/Ar at T_5 = 1214 K and p_5 = 1.25 bar.

The experimental setup was the same as shown in Figure 3.12. A mixture of 1% $C_5H_{10}O$ / Ar was applied for the pyrolysis study. No vibrational relaxation of CO was observed in the calibration measurements, therefore, no H_2 or He was added to the studied mixture. Typical absorbance–time histories of CO from P(8) and R(21) during the pyrolysis and oxidation of 3-pentanone are plotted in Figure 3.17 a and b, respectively. In the pyrolysis measurements, both lines show increasing absorbance during the observation time. In the oxidation measurements, the absorbance of each line reaches a maximum value and then decreases till the end of the test time. The temperature of the test gases was inferred from the measured absorbance ratio and decreases by 100 K during the pyrolysis (Figure 3.18a) due to the endothermicity of the reaction. The experimental results are compared with a chemical kinetics simulation based on the mechanism proposed by Dames et al. [72] using constrained-volume assumption. The simulated temperature shows excellent agreement in comparison to the measurement. Absorbance profiles of both lines can be used to infer the absolute CO mole fraction. The measured CO concentration is then compared to the simulated one for the pyrolysis in Figure 3.18b. An excellent agreement was also found between measurement and simulation.

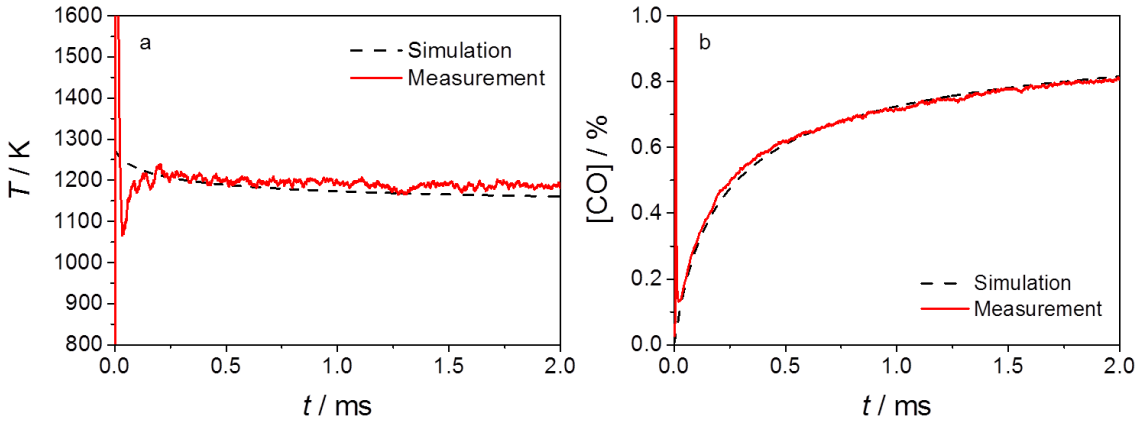

Figure 3.18: Measured temperature and CO concentration profiles of 1% $C_5H_{10}O$/Ar mixture at T_5 = 1275 K and p_5 = 1.25 bar, simulation was performed under constant volume using the mechanism of Dames et al. [72].

Similar measurements were performed for the $C_5H_{10}O$ oxidation behind reflected shock waves using a mixture of 0.285% $C_5H_{10}O$/2% O_2/Ar (ϕ = 1). The measured temperature and CO mole fractions are plotted in Figure 3.19 and compared to the simulation based on the model of Dames et al. [72]. The measurement and the simulation show overall good agreement within the 2.5 ms observation time. The measurement captures the slow increase of temperature during the induction time up to 1.8 ms and followed by an accelerated increase due to heat release after ignition. The measured CO mole fraction showed excellent agreement to the simulation during the induction time, the measured peak value of CO at the time of ignition is slightly lower (8%) than the simulated one which is attribute to the insufficient time resolution of the measurement. Furthermore, the CO consumption after the ignition observed in the measurement is slightly slower compared to the model's prediction.

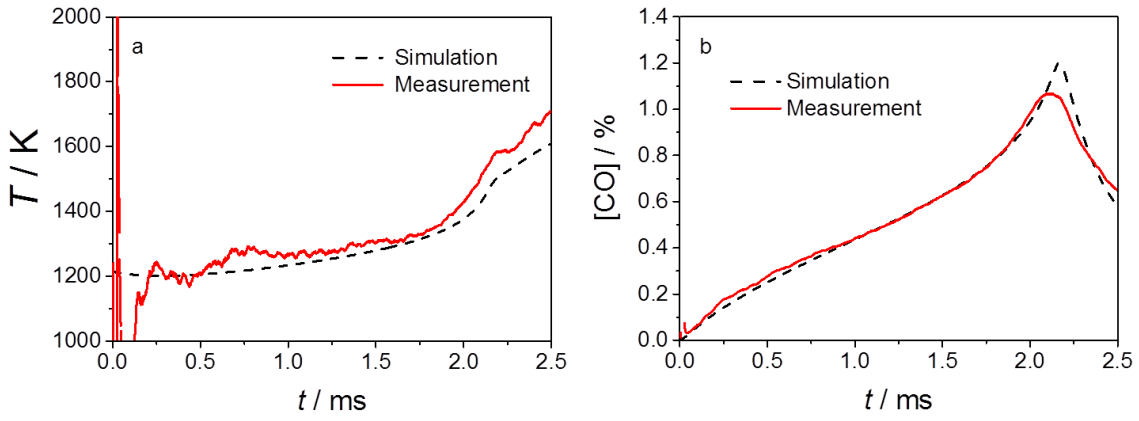

Figure 3.19: Measured temperature and CO concentration–time histories of 0.285% $C_5H_{10}O$/2% O_2/Ar mixture at T_5 = 1214 K and p_5 = 1.25 bar, simulation is based on the mechanism of Dames et al. [72].

Overall, the measurements have proven that the CO absorption line pair P(8)/R(21) is sensitive and reliable for temperature and CO mole fraction determination in reactive systems. Small temperature changes can be well followed with high time resolution and accuracy. The strong absorption line strength of P(8) allows a detection limit of CO down to 10 ppm. In the following chapters, either the line pair P(20)/R(21) or P(8)/R(21) will be applied for gas sensing in reactive systems.

3.3. Uncertainty analysis

An uncertainty analysis was applied to estimate the measurement accuracy in this work. The gas-dynamic states behind the shock wave such as temperature, pressure, and density determined by the approach described in section 2.2 have an overall uncertainty of <1%. Here, the uncertainty of the gas composition, the initial state, and the shock velocity are considered.

The uncertainty of the spectroscopic parameters of the applied absorption lines depends on the states of the test gases and the performance of each laser. The accuracy of the two-line absorption thermometry relies on the line strengths of the absorption lines as well as the stability of laser intensities. The uncertainty of inferred absolute mole fraction of CO depends on the state variables, the spectroscopic parameters, and the intensity of the applied wavelength. Equations 3.3–3.6 describe the estimation of the uncertainties of line strength, argon broadening coefficient, temperature, and CO mole fraction, respectively, which were found to be less than 2.5%, 5%, 1.87%, and 4%, respectively.

$$\sigma_s = \sqrt{\sigma_p^2 + \sigma_T^2 + \sigma_x^2 + \sigma_L^2 + \sigma_{I_0(\upsilon)}^2 + \sigma_{I_t(\upsilon)}^2} \tag{3.3}$$

$$\sigma_\phi = \sqrt{\sigma_p^2 + \sigma_s^2 + \sigma_T^2 + \sigma_x^2 + \sigma_L^2 + \sigma_{I_0(\upsilon)}^2 + \sigma_{I_t(\upsilon)}^2} \tag{3.4}$$

$$\sigma_T = \sqrt{\sigma_s^2 + \sigma_{I_0(\upsilon_1)}^2 + \sigma_{I_t(\upsilon_1)}^2 + \sigma_{I_0(\upsilon_2)}^2 + \sigma_{I_t(\upsilon_2)}^2} \tag{3.5}$$

$$\sigma_x = \sqrt{\sigma_p^2 + \sigma_s^2 + \sigma_L^2 + \sigma_\phi^2 + \sigma_{I_0(\upsilon)}^2 + \sigma_{I_t(\upsilon)}^2} \tag{3.6}$$

4. Results and Discussion

4.1. Partial oxidation of fuel-rich CH_4/O_2 mixtures enhanced by additives

This chapter mainly represents the contents of the peer-reviewed publication 1 (cf. list of own publications), coauthored by Sen et al. As my own contribution, a shock-tube study about the partial oxidation of fuel-rich CH_4/O_2 mixtures enhanced by dimethyl ether and *n*-heptane at elevated temperatures was performed using time-resolved CO and temperature measurements. The experimental data were applied for validation of the chemical kinetics mechanisms in the context of polygeneration processes. Additionally, a kinetics modeling study related to the CO formation was performed to understand the chemistry in detail.

4.1.1. Motivation

Flexibility between the conversion and storage of energy is an important aspect in future energy systems, especially when considering the fluctuating availability of renewable energies. In times of low demand but high availability of energy, an interesting concept is the use of external mechanical or electrical energies in gas turbines to convert "cheap" chemicals (e.g., natural gas) into higher-value chemicals (e.g., H_2/CO) so that most exergy of the cheap fuel is maintained [1]. However, considering the much smaller size and lower cost of the internal combustion engines (ICEs), such polygeneration concept may be more flexible applied in the ICEs [74].

Far away from typical operating regimes of ICEs, the production of chemicals through partial oxidation is normally operated under fuel-rich conditions. In order to implement such polygeneration processes successfully, a fundamental understanding of the chemical kinetics under fuel-rich conditions and the availability of validated reaction mechanisms are necessary. However, most of the reaction mechanisms published in literature have been validated typically for lean and stoichiometric mixtures only [75] because these conditions are important in the standard operation of ICEs and gas turbines. To further understand and develop the kinetics schemes for unusual conditions required for polygeneration processes, this study contributes experimental data that serves as validation data for detailed mechanisms.

In partial oxidation, a frequent challenge is to achieve high total conversion and species specificity at the same time since both are influenced by the reaction conditions. The Glarborg group has reported several investigations on partial oxidation of neat methane in a flow reactor

up to 100 bar [76-79]. Along with high methane conversion, the yield of, e.g., methanol decreases [80]. Neat methane shows only low reactivity resulting in a need for high conversion temperatures. The addition of additives or co-reactants can reduce the temperatures required to start the conversion [81]. Dimethyl ether (DME) has been demonstrated to promote the ignition of methane in HCCI engines [82] and is therefore of interest as an additive in the framework of polygeneration conversion processes at high pressure. An earlier study of methane ignition at high pressure [83] has shown that *n*-heptane enhances the reactivity of methane even more effectively than DME. Therefore, in this study the effects of DME and *n*-heptane as activating agents were examined under fuel-rich conditions.

4.1.2. Results of the CO measurements

Validation of reaction mechanisms always needs experimental data of fundamental chemistry experiments. In this study, a shock tube was applied as homogeneous reactor to investigate the validity of reaction mechanisms for fuel-rich conditions using methane as benchmark. The two-line absorption thermometry using the CO line pair P(20)/R(21) and the fixed-wavelength method provides precise time-resolved information of the CO formation as well as the temperature within the observation time. Temperatures were evaluated as described in section 2.3.5 and absolute CO mole fractions were inferred from the absorbance of P(20) using Eq. 2.37.

Shock-tube experiments were performed at high temperature behind reflected shock waves for fuel-rich mixtures of CH_4 /(DME or *n*-heptane)/O_2 ($\phi = 2$) highly diluted in argon and helium between 1400 and 2000 K at pressures of 1–2 bar. The experimental results are interpreted by comparison with simulations using elementary reaction mechanisms from literature. The simulation of the shock-tube data in the framework of this investigation was performed using Chemical Workbench [36] for a homogeneous reactor at constant volume. The data output time increment was set to 1 μs adapt to the time resolution of the laser spectroscopy.

To complement the experimental finding in the shock tube, measurements in a plug-flow reactor (PFR) were performed in a parallel study by Sen et al. [84] under the conditions that are not accessible by the shock tube for example at low/intermediate temperatures and for longer reaction times.

The experimental conditions for the shock-tube experiments are summarized in Table 4.1, along with mixtures, temperatures, and pressure. Details are described below.

Table 4.1: Reaction conditions for shock tube measurements

Case	CH_4 / mol%	O_2 / mol%	DME / mol%	*n*-heptane / mol%	Ar/He / mol%	*p* / bar	*T* / K	ϕ
A	1.90	2.05	0.10	-	75.95/20	1–1.6	1650–2050	2
B	1.80	2.10	0.20	-	75.90/20	1–1.6	1700–2000	2
C	1.90	2.45	-	0.10	75.55/20	1–1.6	1600–1900	2

Figures 4.1 and 4.2 show measured CO mole-fractions (a) and temperatures (b) compared to simulations for mixtures A and B (Table 4.1) at 1600–2100 K and 1.0–1.6 bar. Because the formed CO is not vibrationally thermalized, helium was added to accelerate the vibrational relaxation. In CO/Ar mixtures without added He, the relaxation times range between 70 and 300 µs for 2100–1700 K. These values are used as a rough estimate to describe relaxation times for thermally-excited CO which is formed by the oxidation of CH_4 or DME. Because the oxidation is accompanied by a large temperature increase within the test time (~400 K), the line strength variations of both selected lines within the test time must be taken into account for the calculation of the absolute CO mole fraction. Moreover, pressure broadening was taken into account by using the measured temporal variation of the pressure.

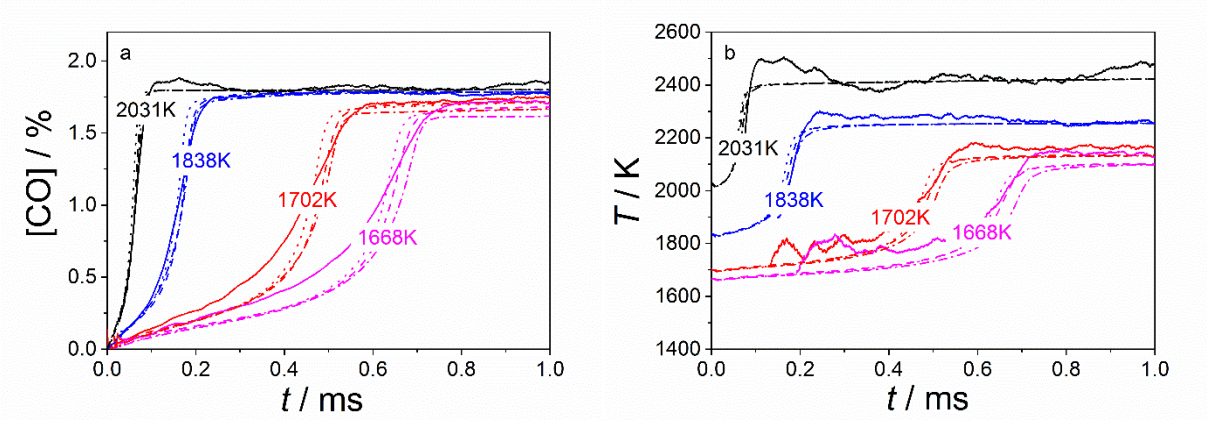

Figure 4.1: CO mole fraction (a) and temperature (b) as a function of time during the oxidation of mixture A (CH_4/DME/O_2(1.9/0.1/2.05%) balanced in 75.95% Ar and 20% He) at four temperatures between 1668 and 2031 K and ~1.5 bar. Simulations with the Yasunaga et al. mechanisms [85]: dashed line, Burke et al. [86]: dotted line, Zhao et al. [87]: dash-dotted line.

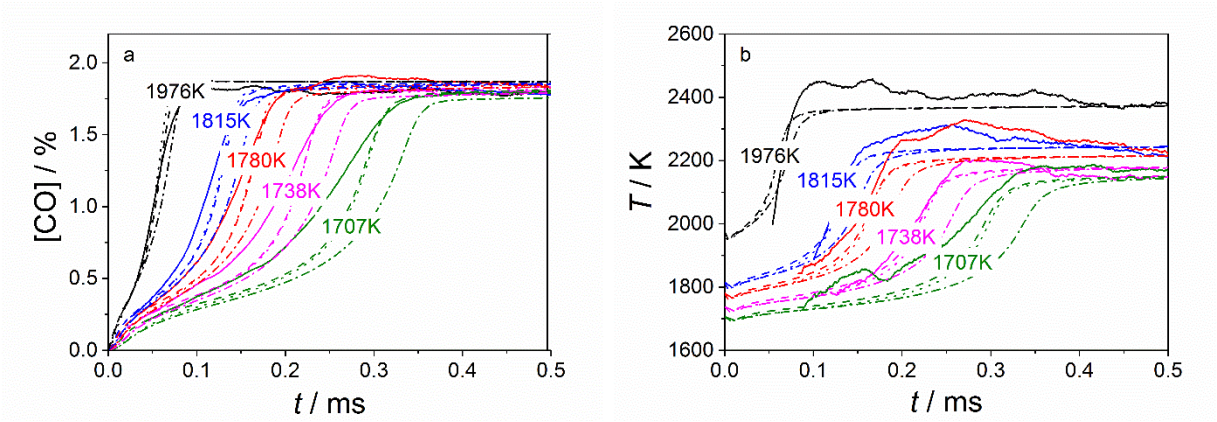

Figure 4.2: CO mole fraction (a) and temperature (b) during the oxidation of mixture B (CH_4/DME/O_2(1.8/0.2/2.1%) balanced in 75.90% Ar and 20% He) at five temperatures between 1707 and 1976 K and at ~1.5 bar. Simulations with the Yasunaga et al. mechanisms [85]: dashed line, Burke et al. [86]: dotted line, Zhao et al. [87]: dash-dotted line.

The simulations in Figs. 4.1 and 4.2 were performed based on the mechanisms from Yasunaga et al. [85], Zhao et al. [87], and Burke et al. [86] under constant volume using the calculated temperatures and pressures behind the reflected shock waves as initial conditions.

Yasunaga et al. [85, 88] developed their mechanism for diethyl ether that was originally validated against ignition delay times and concentration–time profiles measured in a shock tube. In a later paper, the same methodology was followed to assemble a reaction mechanism of a series of ethers such as ethyl-methyl, methyl-tert-butyl, and ethyl-tert-butyl ether [85]. To simulate the experimental results, the complete mechanism of Yasunaga et al. was applied that contains a sub-mechanism of DME.

Zhao et al. [87] developed their model first based on the experimental data of pyrolysis of DME in a variable-pressure flow reactor. The model was then extended to describe the high-temperature oxidation chemistry. The high-temperature mechanism was then further combined with a mechanism for low-temperature oxidation chemistry adapted from Ref. [89].

Burke et al. [86] developed their mechanism for CH_4 /DME blends that was validated against ignition delay times measured in a shock tube and a rapid compression machine for a wide range of conditions. Like the former studies, this work also covers gas turbine-relevant conditions and therefore is mainly combustion oriented with a high DME content (20–100%).

Overall, the agreement between the measured and simulated temporal CO mole-fraction profiles and the temperature profiles is good. There are slight deviations in the temperature levels at

short times but this is mainly attributed to the limited precision of the two-line absorption thermometry in this early phase, where CO mole fractions are low. The plateau values of temperature and CO mole fraction are predicted well compared to the experimental data. All the mechanisms predict the trends of CO concentration and temperature profiles similarly well. However, the mechanism of Zhao et al. [87] predicts a slower temperature increase and CO formation compared to Yasunaga et al. [85] and Burke et al. [86]. The differences became stronger when the DME concentration in the mixture is increased from 0.1 to 0.2% (mixture A to B). In the mixture B, the simulations from Yasunaga et al. [85] and Burke et al. [86] almost overlap with each other whereas the Zhao et al. [87] predicted 50–20 µs delay of reaching the plateau values of temperature and CO concentration at 1701–1976 K.

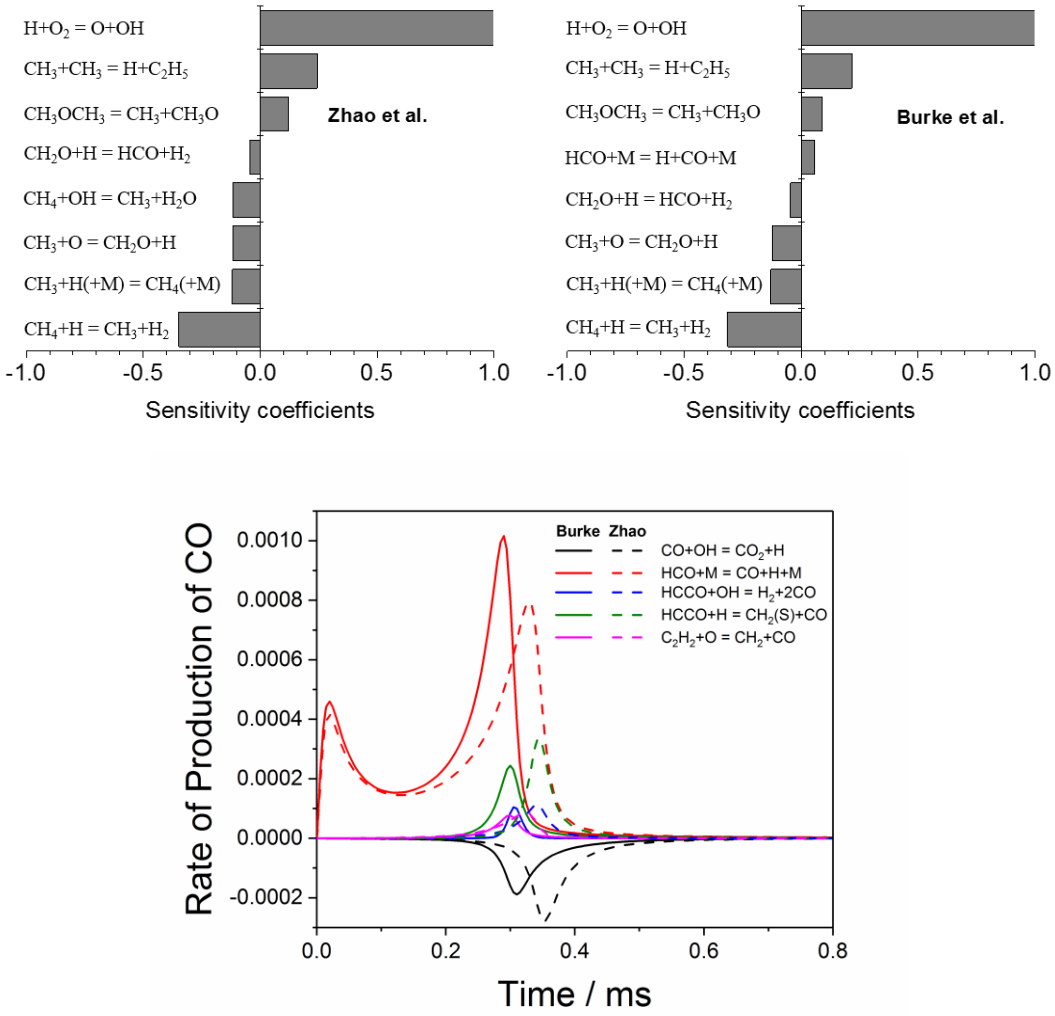

Figure 4.3: Top: Sensitivity analysis for the most important elementary reactions with respect to the influence of CO on the reaction using the mechanisms of Zhao et al. [87] and Burke et al. [86] at 1707 K (mixture B). The analysis is performed for the fastest CO formation. Bottom: Simulated rate of production of CO at 1707 K (mixture B) based on the mechanisms of Burke et al. (full lines) and Zhao et al. (dashed lines).

Sensitivity and rate of production (ROP) analyses were applied based on the mechanism of Zhao et al. and Burke et al. to identify the important elementary reactions that are sensitive to CO formation and CO consumption under the conditions of mixture B at 1707 K. The timing for the sensitivity analysis was chosen at the steepest increase of the CO which is also related to the ignition delay time. Figure 4.3 (top) shows the comparison of the sensitivity coefficients and both mechanisms show very similar results. By comparing the ROP from both mechanisms (Figure 4.3 bottom), the reaction HCO+M = H+CO+M shows a higher rate on CO formation in the Burke et al. mechanism in comparison to the Zhao et al. mechanism, but this reaction is identified as the main CO-formation channel in both mechanisms. Moreover, the rate constants of other CO formation reactions (e.g., HCCO+H = CH_2(S)+CO and HCCO+OH = H_2+2CO) applied by Burke and co-workers are all faster than by Zhao et al. Larger differences between both mechanisms are that the formation as well as the consumption of HCO from DME in the Burke et al. mechanism are faster than in the Zhao et al. mechanism, and the DME consumption in the Burke et al. mechanism is also faster. Furthermore, the reaction CO+OH = CO_2+H in both mechanisms is found to be the key reaction of CO consumption that also determines the time when CO reaches its peak value (Figure 4.3 bottom), Burke and co-workers used faster rate constants for this reaction in comparison to Zhao et al. As result, the Zhao et al. mechanism predicts slower CO formation compared to Burke et al, and the difference is growing with increasing DME concentration.

Additionally, analysis of the species profiles and of the reaction fluxes show no significant differences between the mechanisms. Species concentration profiles of educts, intermediate species like H, CH_3, C_2H_2, C_2H_4, and C_2H_6, and products like CO, CO_2, H_2, and H_2O are quite similar regarding their absolute values and their temporal behavior. The Zhao et al. mechanism predicts also a higher importance of the formation of CH_3OCH_2 compared to the other mechanisms. These differences have no significant importance for the further reaction progress. The most significant difference in the formation of important intermediates can be observed for acetylene consumption after the ignition. The Zhao et al. mechanism predicts a slower consumption of C_2H_2 compared to the other two mechanisms. The simulated product concentration profiles differ significantly only for CO_2. The detailed chemical conversions are studied in detail by Sen et al. in the plug-flow reactor experiments for DME [84] at 532–992 K and 4.5–8.4 bar.

The CO and temperature measurements during the oxidation of mixture C were compared to the simulations based on Mehl et al. mechanism [90] and are shown in Figure 4.4. Mehl and co-workers developed their model first for describing the experimental data of different fuel

compositions in a HCCI engines [91], the model was then extended for several components relevant to gasoline surrogate formulation investigated under a wide range of conditions in shock-tube, rapid compression machine, and jet stirred reactor experiments [90].

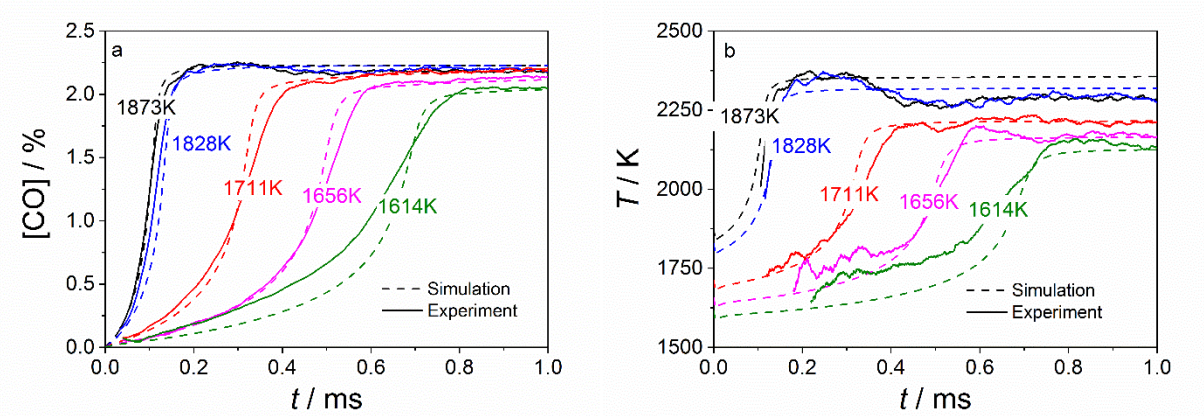

Figure 4.4: CO mole fraction (a) and temperature (b) during the oxidation of mixture C (CH_4/*n*-heptane/O_2(1.9/0.1/2.45%) balanced in 75.95% Ar and 20% He) at five temperatures between 1614 and 1873 K at ~1.4 bar. The dashed lines are simulations with the Mehl et al. mechanism [90].

Figure 4.4 shows good agreement between measured and simulated CO mole fractions and temperature. The measured temperature at 1828 and 1873 K show a temperature decrease after ~0.4 ms which is attributed to gas-dynamic cooling, possibly due to a weak interaction of the reflected shock wave with the contact surface. The CO-concentration time histories were simulated using a gas-dynamic model assuming constant pressure. Interestingly, a large deviation in the final temperature was seen between the simulation and the experiment under the assumption of constant pressure which is evidence that post-shock conditions can be considered as uniform and near-constant volume.

The additive DME increases the reactivity of methane in the shock-tube experiments and thus helps to reduce auto-ignition temperatures in ICE polygeneration. The experiments using *n*-heptane addition indicate that *n*-heptane is another promising additive which requires further attention in future work.

Mechanisms of Burke et al. and Zhao et al. were analyzed to interpret the enhancement of CO formation during the conversion of CH_4 in the presence of DME. $CH_4+H = CH_3+H_2$ was identified as the key reaction for methane depletion in both mechanisms and is followed with $CH_4+OH = CH_3+H_2O$ as second important reaction. The initiation of DME consumption is its unimolecular decomposition $CH_3OCH_3 = CH_3+CH_3O$ that is followed immediately by $CH_3O = H+CH_2O$, where the H radical is the initiator of methane consumption as well as the OH formation $H+O_2 = OH+O$; and CH_2O is the precursor of HCO that produces CO. It can be seen

that the presence of DME does not open new methane oxidation pathways, instead, DME conversion supplies the radicals needed to start the methane oxidation. Since DME conversion occurs at relatively low temperature, methane oxidation is enhanced towards lower temperature with presence of DME.

An increase of the DME concentration from 0.1 to 0.2% increases the formation of OH by a factor of two at 1738 K in the mechanism of Burke et al. [86]. As an overall result of OH formation from increasing DME concentration the CH_4 conversion is shifted about 100 K lower (Figure 4.5) when increasing the amount of DME (cf., Figs. 4.1 and 4.2, left) and keeping the same equivalence ratio, the CO build-up increases at the same temperature (e.g., 1700 K) which is a clear indication for the enhancement of CH_4 oxidation by DME.

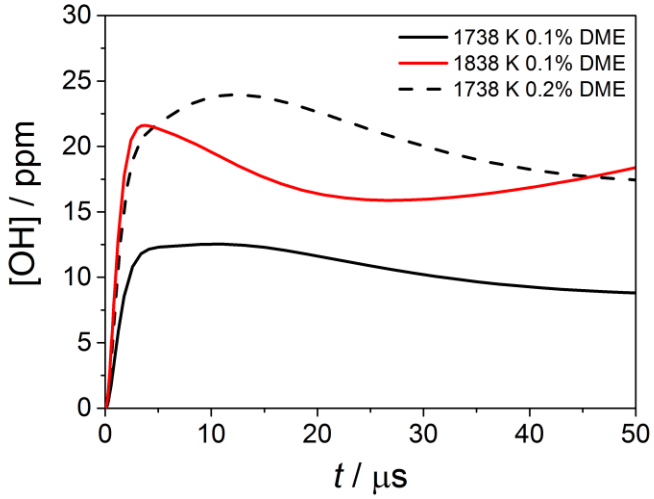

Figure 4.5: Simulated OH mole fractions over time at 1738 and 1838 K with 0.1–0.2% DME addition using the mechanism of Burke et al. [86].

The activating effect of DME was also investigated by other groups [92-94], where DME was studied as a fuel additive in Diesel engines or as an ignition enhancer for methanol in Diesel engines. Fischer et al. [89] reported that the most important initiation reaction for DME is the unimolecular decomposition to form methoxy (CH_3O) and methyl (CH_3) radicals. Methoxy radicals then react mainly to formaldehyde [89].

Sen et al. [84] investigates the CH_4 and CH_4/DME reactions in a flow reactor at 6 bar and 532–992 K for mixtures at $\phi = 2$ to complement the experimental finding in the shock tube. The mole fractions of main species such as O_2, CO, and H_2O are well predicted by all mechanisms. However, the DME mole fraction profile was better predicted by the mechanism of Zhao et al. The analysis shows that the Zhao et al. mechanism predicts higher OH mole fractions at lower

temperature than the mechanism of Burke et al. because of differences in the implementation of the DME oxidation schemes.

A direct comparison between the shock-tube and flow-reactor data [84] is not straight forward because of the different temperature ranges investigated. However, both shock-tube and flow-reactor results confirm CO as main product of the partial oxidation for the fuel-rich conditions and that DME strongly reduces the reaction temperature. The results demonstrate that the combination of methane and DME can be applied for polygeneration processing for the production of synthesis gas under engine conditions. Overall, the results of both experiments are well predicted by all mechanisms considered here for the low- and high-temperature range. These mechanisms are therefore a good starting point for the development of a mechanism that specializes in the prediction of chemical conversion processes.

4.1.3. Conclusions

Partial oxidation of rich CH_4/air mixtures with DME and *n*-heptane as additives was studied in a wide range of temperature conditions in a shock tube. Reactions of fuel-rich mixtures ($\phi = 2$) of CH_4 with DME (1.9% CH_4/0.1% DME/2.05% O_2/20% He/Ar) and *n*-heptane (1.9% CH_4/ 0.1% *n*-heptane/2.45% O_2/20% He/Ar) were investigated behind reflected shock waves at 1600–2000 K in a pressure range of 1.3–1.6 bar. CO mole fractions and temperature were measured with quantum cascade laser MIR laser absorption spectroscopy with microsecond time resolution. The measurements were compared to simulations based on the mechanisms of Yasunaga et al. [85], Zhao et al. [87], and Burke et al. [86] for the CH_4/DME mixture and Mehl et al. [90] for the CH_4/*n*-heptane mixture. Good agreement was found with all models.

In summary, the data of shock-tube experiments are reproduced satisfactorily by the tested mechanisms. However, none of mechanisms is optimized for chemical conversion reactions and even small deviations in the kinetics schemes can influence the formation of potential product species. A mechanism that is suited for reaction planning therefore needs to be sensitive to such subtleties and needs to be validated by experiments under typical conversion reaction conditions.

4.2. Thermal decomposition of anisole

This chapter mainly represents the contents of the peer-reviewed publication 3 (cf. list of own publications), coauthored by Peukert et al. As my own contribution, an experimental and modeling study about anisole pyrolysis was performed using time-resolved CO absorption measurement. Main result of this work is the experimentally determined reaction rate of the unimolecular decomposition of the phenoxy radical between 970 and 1170 K at ~1.4 bar. Additionally, a sensitivity analysis was performed to investigate the most important elementary reactions on the CO formation in the anisole pyrolysis. The co-author S. Peukert provided the *ab initio* calculation of the potential energy surface for the phenoxy radical dissociation at the G4 level of theory, this content is briefly described below for a direct comparison between the measured and calculated rate constants.

4.2.1. Motivation

Anisole ($C_6H_5OCH_3$) has recently been identified as a promising fluorescence tracer for fuel/air mixing studies based on laser-induced fluorescence (LIF) [95]. For reliable and quantitative application of anisole LIF, the photophysical properties of anisole have been investigated [95-98] in detail. However, when used as tracer, the kinetics of anisole decomposition should be known to derive reliable and quantitative quantities. It is necessary to assess the temperature/time range where it can be used without decomposition.

Anisole decomposition has been widely investigated [99-101]. It is assumed that the first step (R 4.1) occurs via homolytic cleavage of the O-CH_3 bond. This is consistent with anisole bond strengths of 405.4 and 264.4 kJ/mol for CH_2-H and C_6H_5O-CH_3 [102], respectively.

$$C_6H_5OCH_3 \rightarrow CH_3 + C_6H_5O \qquad \text{(R 4.1)}$$

The decomposition of the resonance-stabilized phenoxy radical (C_6H_5O) produces CO and cyclopentadienyl (C_5H_5), the latter is assumed to be an important intermediate towards soot formation [103]. The dissociation of the C–O bond of anisole was first measured by Paul and Back [104] using toluene scavenging at 720–795 K and at 5–12 mbar. The decomposition of anisole was studied in a glass vacuum apparatus using toluene/anisole mixtures (30–45:1 pressure ratio). The rate constant k_1 of reaction R 4.1 was measured by monitoring the produced methane concentration via gas chromatography. A C–O bond dissociation energy of 238.5±8 kJ/mol was reported. Lin and Lin [99] applied the shock-tube technique to study phenoxy pyrolysis at 1000–1580 K and 0.4–0.9 bar. Anisole and allyl phenyl ether were used as phenoxy radical

precursors. The CO concentration was monitored by IR laser absorption with a 1→0 P(10) transition. A rate constant expression of $k_1 = 1.2\pm0.3\times10^{16}\,\exp(-275.3\ \text{kJ mol}^{-1}/RT)\text{s}^{-1}$ was proposed by fitting the observed initial CO concentration profiles at temperatures lower than 1200 K. Mackie et al. [100] also studied anisole pyrolysis at 850–1000 K and 16–120 mbar in a perfectly stirred reactor and determined a rate constant of $2.9\pm1.0\times10^{15}\,\exp(-267.8\pm2.5\ \text{kJ mol}^{-1}/RT)\text{s}^{-1}$ for R 4.1. By extrapolating the data of Mackie et al. [100] up to 1200 K, the proposed rate constants from Lin and Lin [99] and Mackie et al. [100] show excellent agreement within their reported uncertainties. Suryan et al. [105] studied the thermal decomposition of anisole and three isomeric hydroxy-anisoles and methoxy-anisoles in a low-pressure ($p < 1.3\times10^{-3}$ mbar) pyrolysis apparatus and reported a high-pressure rate expression of $k_1 = 10^{15.5}\,\exp(-265.7\ \text{kJ mol}^{-1}/RT)\text{s}^{-1}$ between 720 and 795 K. Arends et al. [106] extended the study of anisole thermolysis in H_2 atmosphere in a tubular flow reactor at 793–1020 K. The rate constants k_1 were separately determined between 790 and 875 K and an Arrhenius expression of $k_1 = 10^{15.3\pm0.2}\,\exp(-266.1\pm2.9\ \text{kJ mol}^{-1}/RT)\text{s}^{-1}$ was reported, which was in very good agreement with the data of Mackie et al. [100] and Suryan et al. [105].

The phenoxy radical from reaction R 4.1 can then undergo two types of reactions. They can either decompose to cyclopentadienyl (C_5H_5) and CO, where C_5H_5 is assumed to be a main precursor of benzene, naphthalene, and heavier PAHs [103, 107], or it can react with H atoms or CH_3 radicals to yield phenol (C_6H_5OH) or ortho- and para-cresol ($C_6H_4CH_3OH$), respectively.

$$C_6H_5O \rightarrow CO + C_5H_5 \qquad \text{(R 4.2)}$$

$$C_6H_5O + H \rightarrow C_6H_5OH \qquad \text{(R 4.3)}$$

$$C_6H_5O + CH_3 \rightarrow C_6H_4CH_3OH \qquad \text{(R 4.4)}$$

There are only three experimental investigations on reaction R 4.2. Colussi et al. [108] performed the first study of phenoxy decomposition using a low-pressure Knudsen flow setup (very low-pressure pyrolysis, VLPP). A rate constant k_2 of $10\pm5\ \text{s}^{-1}$ at 1000 K was reported. In a shock-tube study, Lin and Lin [99] obtained a rate expression $k_2(T) = 2.51\times10^{11}\,\exp(-183.7\pm3.7\ \text{kJ mol}^{-1}/RT)\text{s}^{-1}$. Here, relatively high initial concentrations of anisole (0.108–0.758 % in argon) were used. The decomposition was modeled using a four-step assumption considering the secondary reactions of R 4.4 and the recombination of methyl radicals towards ethane, which were assumed to affect the deficiency in final CO concentration. k_2 and k_4 were varied simultaneously to obtain the best fit to the measured CO profiles. Frank et al. [109]

performed shock-tube measurements covering the 1020–1190 K range at 1.3–2.5 bar. CO concentrations were measured using sensitive molecular resonance absorption spectroscopy (MRAS) and an Arrhenius expression of $k_2(T) = 7.5\times10^{11}\ \exp(-183.7\ \text{kJ mol}^{-1}/RT)\text{s}^{-1}$ was proposed, which is faster than the one found by Lin and Lin with a factor of three. Various theoretical studies [110-112] have also been conducted to study the thermal decomposition of phenoxy radicals. Colussi et al. [108] proposed a bicyclic intermediate for reaction R 4.2 that ring-opens to the 2,4-cyclopentadienyl carbonyl radical and subsequently decomposes to CO and cyclopentadienyl (Figure 4.6).

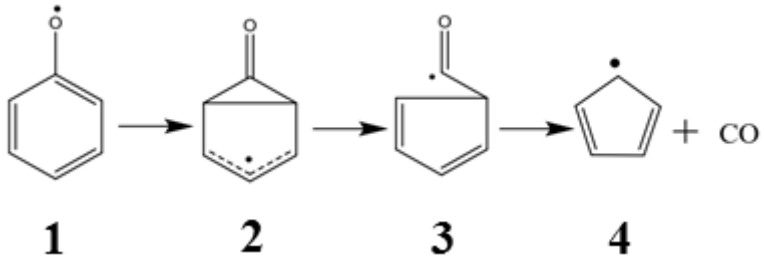

Figure 4.6: Schematic pathway of unimolecular decomposition (R 4.2) of the phenoxy radical [108, 112].

Studies of Olivella et al. [110] and Liu et al. [111] supported this pathway and Carstensen and Dean [112] indicated that while the theoretical and experimental studies agree on the mechanism, the theoretical studies suggest a substantially higher (higher by 41.8 kJ/mol) overall barrier than the one found in the experimental studies of 183.7 kJ/mol. Carstensen and Dean [112] performed electronic structure calculations at CBS-QB3 and CBS-QB3//QCISD/6-31G(d) levels of theory to construct the relevant portion of the C_6H_5O potential energy surface (PES) and proposed a high-pressure rate constant $k_2 = 2.5\times10^{14}\ \exp(-229.3\ \text{kJ mol}^{-1}/RT)\text{s}^{-1}$.

Phenoxy radical reactions with H atoms and CH_3 were also extensively discussed [113, 114]. Pecullan et al. [114] proposed a kinetics model for pyrolysis of anisole that contains 66 reversible reactions involving 31 species. This mechanism was validated against experimental data from an atmospheric-pressure flow reactor coupled with gas chromatography and mass spectrometry. They recognized that the oxidation of anisole at atmospheric pressure near 1000 K did not differ significantly from its pyrolysis at the same nominal conditions [114] and that even in the presence of O_2, anisole depletion follows first-order kinetics. Recently, Nowakowska et al. [101] developed a detailed kinetics model for anisole pyrolysis and oxidation containing 303 species and 1922 reactions. The model was validated against an experimental study performed in a jet-stirred reactor operated at constant temperature and pressure. Because of long residence

times, the determination of the initial reaction rates during the decomposition of anisole is complicated by the influence of secondary reactions.

However, neither mechanism from Pecullan et al. [114] nor Nowakowksa et al. [101] have been validated by time-resolved species concentration measurements at elevated temperatures. The CO concentration–time histories in anisole pyrolysis can provide strong constraint of mechanism validation since R 4.2 is the most important pathway for CO formation. To minimize the effect of secondary reactions, the initial concentrations must be kept as low as possible.

4.2.2. Results and discussion

Pyrolysis of four mixtures of anisole (5000, 1000, 500, and 200 ppm anisole in Ar) was studied behind reflected shock waves at 1000–1270 K and 1.3–1.6 bar. Absorption measurements were applied to monitor time-resolved CO concentrations within the 2 ms test time with 1 μs time resolution. In total, 30 experiments were performed.

Additional experiments using allyl phenyl ether ($C_6H_5OC_3H_5$) as a source of pure phenoxy were performed to determine k_2 without the influence of bimolecular phenoxy reactions. The rate constants of unimolecular phenoxy decomposition with allyl phenyl ether as phenoxy source were determined at 970–1170 K and ~1.4 bar. Experimental data of anisole and allyl phenyl ether pyrolysis were then compared to simulations based on the kinetics model of Nowakowska et al. [101]. The simulations were conducted using Chemical Workbench [36] assuming a homogeneous constant-volume reactor.

In order to rationalize the experimental findings reported in this work, the potential-energy surface (PES) for the phenoxy radical decomposition presented by Carstensen and Dean [112] has been re-evaluated by conducting electronic structure calculations at the G4 level of theory. Like CBS-QB3, which was applied by Carstensen and Dean, G4 is also a composite method in which a sequence of *ab initio* calculations is performed to get the total energy of a molecular compound. Geometries and frequencies are calculated using B3LYP density functional theory with the 6-31G (2df,p) basis set. The frequencies are scaled by a factor of 0.9854 prior to their use to calculate zero-point energies (ZPE). The electronic structure calculations were performed using the Gaussian09 program package [115]. Master equation calculations were carried out with Unimol [116] using the *ab initio*-based rovibrational properties and energetics of the minima and transition states to obtain theoretical rate constants. Lennard Jones parameters of the phenoxy radical were taken from the study of Carstensen and Dean [112]. Modified Arrhenius

fits to the theoretical rate constants for the decomposition of the phenoxy radical are provided in the appendix 8.3.

Figure 4.7a shows a typical absorbance–time history of the transmitted light at both laser wavelengths behind a reflected shock wave at 1223 K and 1.26 bar with mixture of 5000 ppm anisole in argon. The inferred temperature shows a quasi-constant temperature value during the decay of anisole so that it was not necessary to consider the temperature dependence of the absorption line strengths for calculations of the absolute CO mole fraction. The measured and calculated temperature using the model of Nowakowska et al. [101] show a very good agreement (Figure 4.7b).

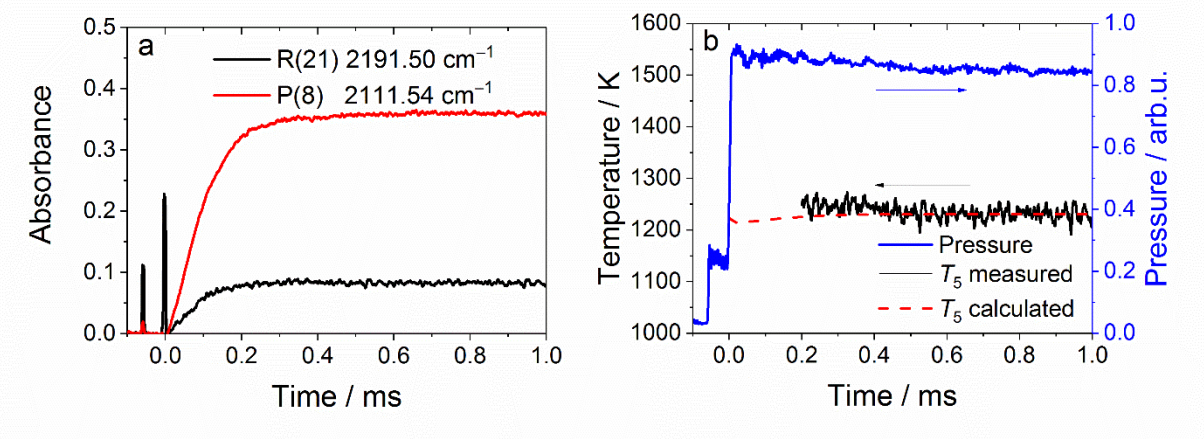

Figure 4.7: (a) Absorbance–time histories of CO P(8) and R(21) during the pyrolysis of anisole for mixture of 0.5% anisole / Ar at 1223 K and 1.26 bar; (b) measured temperature and pressure profiles and calculated temperature based on the Nowakowska et al. [101] mechanism.

In this work, the absorbance of P(8) was used to inferred the absolute CO mole fraction due to its strong line strength at the investigated temperatures. Figure 4.8 shows measured CO mole fractions for 5000 ppm anisole/Ar mixtures at 1033–1262 K and 1.3–1.6 bar together with simulation results using the model of Nowakowska et al. [101]. Overall, the simulations predict a slower formation of CO in comparison to the measurements at all temperatures. In addition, the simulated plateau values of CO from 1179 to 1262 K are 20–30% lower than those from the measurements. The measurements show that at temperatures above 1180 K, only about 70–80% of the O atoms in anisole were converted to CO. One simulation was implemented to analyze the O atom content in the products of 5000 ppm anisole/Ar mixture decomposition at 1223 K and 1.26 bar using model of Nowakowska et al. and the results are shown in Figure 4.9. The simulation predicts that the missing O atoms are contained mainly in phenol and cresol that were produced by bimolecular reactions of phenoxy with H and CH_3, respectively. On the other hand, the simulated content of O atoms indicates that the formation of phenol and cresol

strongly depleted the formation of CO and resulted in a much lower plateau value of CO. Lin and Lin [99] observed similar trends in oxygen mass balance in their work in a similar temperature range. Frank et al. [109] reported a 100% conversion of anisole to CO at all conditions using highly diluted mixtures (20, 36, and 55 ppm anisole in Ar). To further mitigate the effect of secondary reactions, three additional highly diluted mixtures of anisole (1000, 500, and 200 ppm in Ar) were prepared for CO concentration measurements. Figure A8 shows the results of CO concentration time-histories at 1040–1240 K and 1.3–1.6 bar together with the predictions from the model of Nowakowska et al. [101]. The comparison shows also similar discrepancies as in the measurements with high initial concentrations. In the experiments at ~1200 K, an increase of the fraction of O atoms in CO ([CO]/[$C_6H_5OCH_3$]) from 0.76 to 0.8 and 0.85 were observed when the anisole concentrations were varied from 1000 to 500 and 200 ppm, respectively. The model of Nowakowska et al. predicted corresponding values of 0.5, 0.6, and 0.65 at the same temperature. The mechanism thus indicates a stronger influence of secondary reactions on the CO production than observed in the measurements.

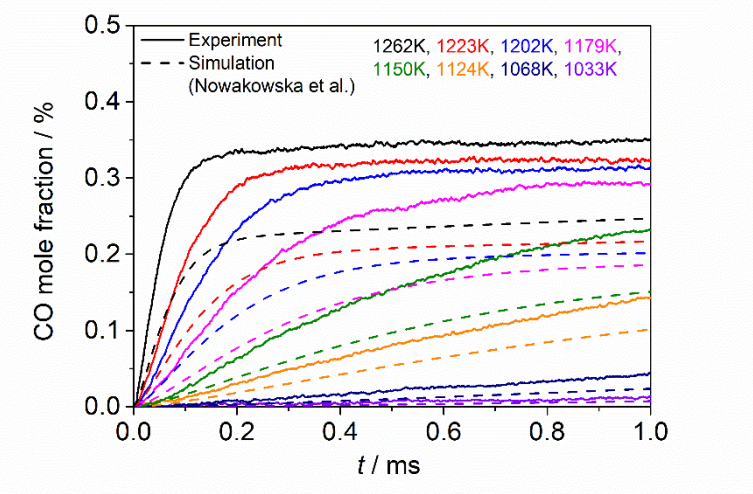

Figure 4.8: CO mole fractions during the pyrolysis of a 5000 ppm anisole/Ar mixture at eight temperatures between 1033 and 1441 K at ~1.3 bar. The dashed lines are simulations using the Nowakowska et al. mechanism [101].

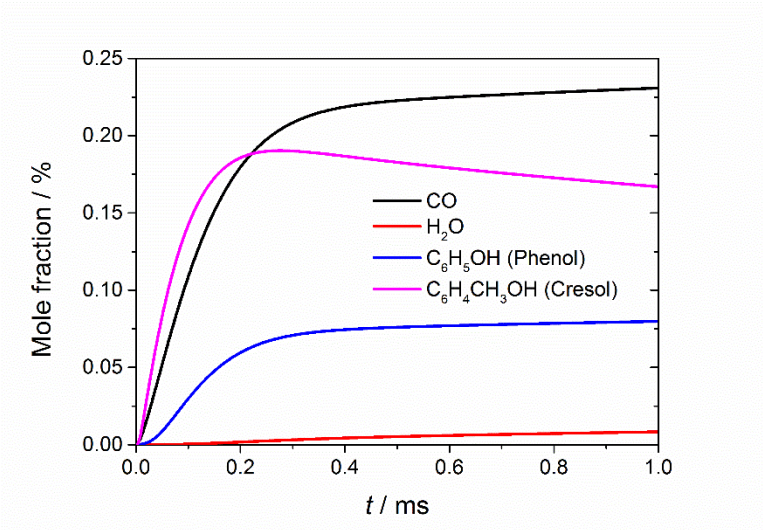

Figure 4.9: Simulated distribution of O atoms in the product species of a 5000 ppm anisole/Ar mixture at 1223 K and 1.26 bar using the Nowakowska et al. Mechanism.

To further support the experimental findings of anisole pyrolysis described in the previous section, allyl phenyl ether ($C_6H_5OC_3H_5$) was used as a source of pure phenoxy to prevent the influence of secondary reactions when determining k_2 because of the low reactivity of the allyl radical [108]. k_2 can be therefore determined independently [109]. The kinetics of allyl phenyl ether is described in Ref. 108. In an analogous way as in the case of anisole, ally phenyl ether decomposes to phenoxy and allyl:

$$C_6H_5OC_3H_5 \rightarrow C_3H_5 + C_6H_5O \qquad \text{(R 4.5)}$$

For this investigation, time-resolved CO mole fraction measurements were performed during the pyrolysis of three allyl phenyl ether mixtures (200, 250, and 400 ppm $C_6H_5OC_3H_5$ in Ar) behind reflected shock waves at 970–1170 K and ~1.4 bar. k_2 was then inferred through the mass balance $1-([CO]_t / [C_6H_5OC_3H_5]_0)$ versus time assuming first-order kinetics.

Figure 4.10a shows CO concentration–time histories during the pyrolysis of a 400 ppm $C_6H_5OC_3H_5$/ Ar mixture at 1045–1154 K and ~1.4 bar. Figure 4.10b shows the corresponding analysis for the first-order kinetics, where $-\ln(1 - [CO]_t / [C_6H_5OC_3H_5]_0)$ is plotted versus time. In contrast to anisole, the measured CO concentration from allyl phenyl ether shows almost complete conversion at 1154 K. The linearity of the plot in Figure 4.10b indicates the absence of secondary reactions so that the rate k_2 can be isolated.

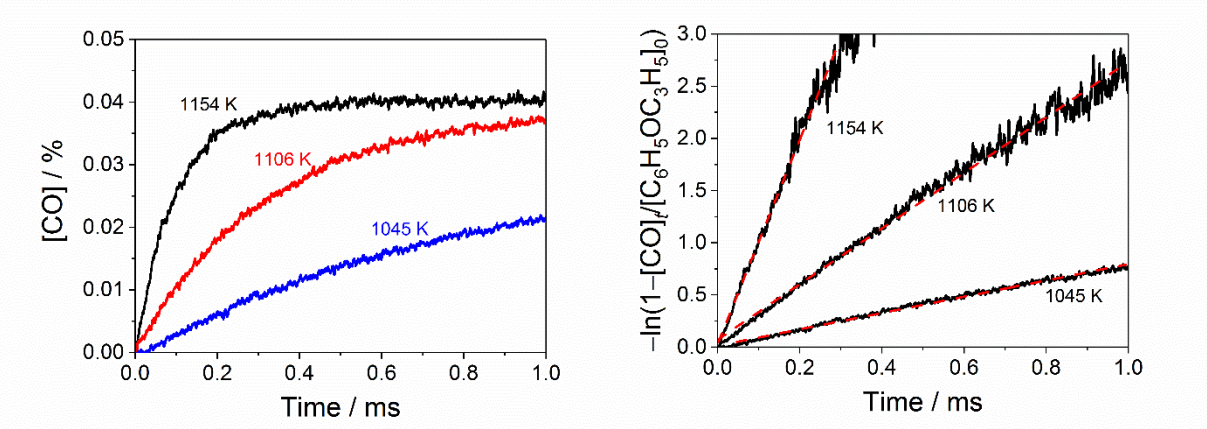

Figure 4.10: (a) CO mole fraction time histories of pyrolysis of allyl phenyl ether mixture (400 ppm $C_6H_5OC_3H_5$/Ar) and (b) rate constants determination under first-order assumption at temperatures 1045–1154 K and ~1.4 bar, black line: measurements; red line: linear fit.

Table 4.2: Summary of the rate constant measurements for reaction R 4.2.

T / K	p / bar	k / s^{-1}
400 ppm allyl phenyl ether in Ar		
1160	1.37	11854
1154	1.41	9456
1106	1.40	2964
1062	1.39	1017
1045	1.43	819
250 ppm allyl phenyl ether in Ar		
1151	1.36	8724
1139	1.40	8930
1112	1.47	3506
1100	1.49	3469
1017	1.37	478
200 ppm allyl phenyl ether in Ar		
1169	1.44	14106
1118	1.41	4209
1071	1.37	1715
975	1.42	161

The results of the first-order evaluations are summarized in Table 4.2 and plotted in Figure 4.11. Experimental data from Lin and Lin [99] and Frank et al. [109], theoretical study from Carstensen and Dean [112], and theoretical re-evaluations by S. Peukert for the present work are also included. A more detailed comparison between all the experimental data sets within the temperature range between 950–1250 K can be found in Figure A9 in the appendix. Lin and Lin [99] determined the rate constants using different anisole concentration (0.1–0.75%) and one allyl phenyl ether mixture (0.336%) at 1000–1580 K and 0.4–0.9 bar, while Frank et al. [109] applied mixtures with very low precursor (anisole and allyl phenyl ether) concentration (20–56

ppm) at 1020–1190 K and 1.3–2.5 bar. The high-concentrations used by Lin and Lin [99] can be responsible for an increased influence of subsequent reactions on the phenoxy radical decomposition, therefore, the measured rate constants of Lin and Lin were lower by approximately a factor of three than those obtained by Frank et al. However, both studies agreed on the activation energy of reaction R 4.2, 183.7 kJ/mol.

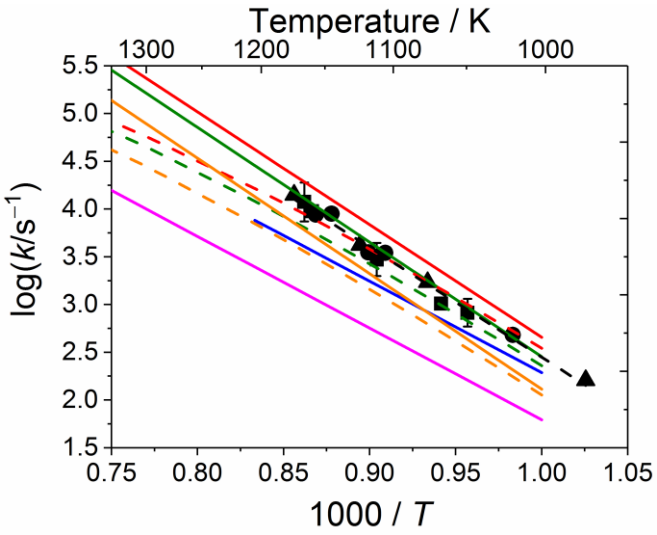

Figure 4.11: Measured rate constant for phenoxy decomposition (R 4.2) compared to values from literature [99, 109, 112]. Squares: 400 ppm $C_6H_5OC_3H_5$ in Ar, circles: 250 ppm $C_6H_5OC_3H_5$ in Ar, triangles: 200 ppm $C_6H_5OC_3H_5$ in Ar, black dashed line: Arrhenius fit of this study, red full line: theoretical calculation at G4 level of theory at 100 bar [118], red dashed line: theoretical calculation at G4 level of theory at 1.4 bar [118], pink full line: Lin et al. [99], blue full line: Frank et al. [109], green full line: Carstensen et al. [112] CBS-QB3 at 100 bar, green dashed line: Carstensen et al. [112] CBS-QB3 at 1.4 bar, orange full line: Carstensen et al. [112] CBS-QB3//QCISD-6-31-G(d) at 100 bar, orange dashed line: Carstensen et al. [112] CBS-QB3//QCISD-6-31-G(d) at 1.4 bar The least-squares analysis of k_2 led to the expression: $k_2(T)=9.1\times10^{13}\exp(-220.3\ \text{kJ mol}^{-1}/\text{RT})\text{s}^{-1}$, with an uncertainty of ±25%.

In the first theoretical study, reported by Olivella et al. [110], the calculated activation energy, i.e. 231.8 kJ/mol in the temperature range 1000–1200 K, was higher than that derived from experimental data. Recently, Carstensen and Dean [112] calculated the PES of phenoxy radical decomposition at the CBS-QB3 and at the CBS-QB3//QCISD/6-31-G(d) level of theory. The molecular properties of the stationary points along the PES were used to derive theoretical rate constants by applying unimolecular rate theory. The pressure and temperature dependence has been obtained by employing different master equation programs like Unimol [116] and Multiwell [117]. In the present work, CBS-QB3 and CBS-QB3//QCISD/6-31-G(d) based rate constant predictions were reproduced by Unimol-calculations using the parameter sets and high-pressure limits, k_{inf}, provided by Carstensen and Dean [112]. The theoretical rate constants ob-

tained from CBS-QB3 calculations (Figure 4.11) are two times lower than the present experimental rate constants. Larger deviations apply for the CBS-QB3//QCISD/6-31-G(d) based rate-constant predictions.

Carstensen and Dean [112] used a value of 200 cm^{-1} for the energy-transfer parameter $<\Delta E>_{down}$. In order to reach a good agreement between the present experimental rate constants and the CBS-QB3-based predictions, it would be necessary to increase the value for this energy parameter to 350 cm^{-1}, which is also a reasonable value. Besides CBS-QB3, also the G4 composite approach has been widely used for calculations of energetic profiles of chemical processes [119-121]. Most recently, Simmie and Sheahan reported that among the composite methods CBS-QB3, CBS-APNO, G3, and G4, the G4 approach is the most accurate one for calculating enthalpies of formation via the atomization procedure [122]. Therefore, the PES obtained by Carstensen and Dean was re-evaluated at the G4-level of theory. The molecular properties from the G4-calculations of the phenoxy radical and the transition state structure **2** → **3** of the PES are described in Ref [118]. Figure 4.12 shows that the G4-based energetics of the stationary points slightly differs by 8–12 kJ/mol compared to the CBS-QB3 based calculations, but qualitatively the PES does not show any significant difference.

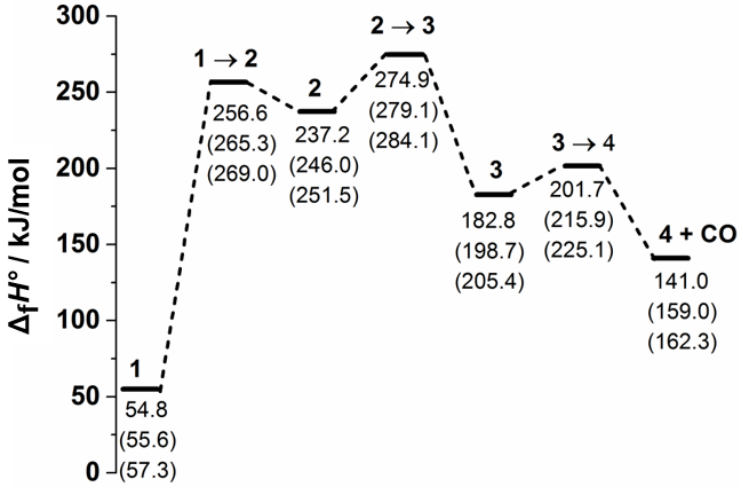

Figure 4.12: Stationary point energies for the thermal decomposition reactions of the phenoxy radical calculated at the G4 level of theory [118]; values in parentheses refer to calculations at the CBS-QB3//QCISD/6-31-G(d) and CBS-QB3 levels of theory obtained from Carstensen and Dean [112].

However, using the same value for $<\Delta E>_{down}$ as Carstensen and Dean [112], 200 cm^{-1}, the G4 based rate constant predictions differ from the CBS-QB3 based calculation. Figure 4.11 includes CBS-QB3, CBS-QB3//QCISD/6-31-G(d) and G4-based high-pressure rate constants and rate constants calculated for 1.4 bar. Without further adjustment, the present theoretical rate constants are within ±20% of the experimental values.

Carstensen and Dean [112] pointed out that the results of their rate constant calculations are very sensitive on the applied method of electronic structure calculation and this is also reflected in the present results. The differences between the calculated rate constants are due to small differences in barrier heights, ~3 kJ/mol between G4 and CBS-QB3 and nearly 9 kJ/mol between G4 and the modified CBS-QB3 method. Therefore, the differences in these sets of theory-based rate constants are well within the anticipated uncertainty in the potential energy surfaces. Within the uncertainties from experimental measurements and theoretical calculations, the results of the current work are therefore in good agreement with both calculations. However, the deviation from the experimental results from Frank et al. [109] cannot be clearly explained.

Since additional experiments with allyl phenyl ether as another precursor for C_6H_5O were conducted in the present work, it seems plausible that these differences are not related to the impact of secondary reactions. The CO-MRAS method applied in study of Frank et al. [109] as well as the laser spectroscopic method applied in this work are of high accuracy for determining CO concentrations. The CO sensor employed has been validated section in 3.2.4. The spectroscopically determined concentrations were in excellent agreement with the actual CO concentrations (see also Figure 3.16). Therefore, the observed differences might arise from uncertainties in temperature measurements. The typical error for temperature measurements in shock tubes is ±1% and by taking into account this level of inaccuracy in the derived rate constant, the differences between Frank et al. [109] and this study are within the corridor of experimental uncertainty. A more detailed comparison between the experimental data sets from Frank et al. [109] and this study are illustrated in Figure A9 (cf. appendix) at temperature between 950–1250 K. The measured rate constants from both studies are very close to each other, the difference between the derived activation energies is attributed to the larger deviation between data points at higher temperature, but still within the corridor of experimental uncertainty.

Analysis

In the mechanism of Nowakowska et al. [101] the reaction R 4.2 is described as a two-step reaction where a bicyclic intermediate was assumed ($C_6H_5O \rightarrow$ bicyclic $\rightarrow CO+C_5H_5$) according to the theoretical calculations [123]. Since the decomposition of 'bicyclic' into CO is much faster than the conversion of phenoxy into "bicyclic", the formation of CO from phenoxy radical is strongly limited by the reaction rate of the conversion step to "bicyclic". The rate constants of both reaction steps were not determined by direct measurements. Simulations based on the Nowakowska model and the measurements showed large discrepancy in CO concentration below 1300 K, therefore the two-step reactions ($C_6H_5O \rightarrow$ bicyclic $\rightarrow CO+C_5H_5$) adopted

in the model of Nowakowska was substituted by the measured rate constants for reaction R 4.2 in the current work.

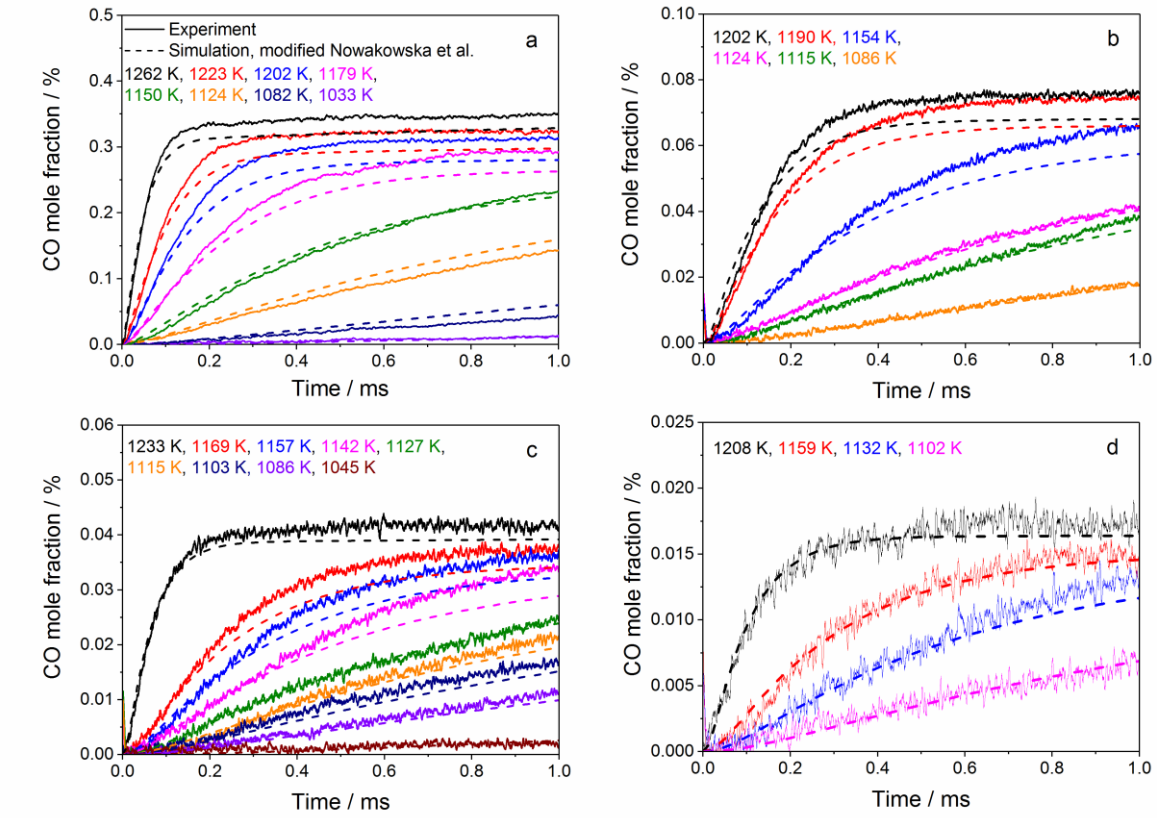

Figure 4.13: CO mole fraction measurements during pyrolysis of anisole at four initial concentrations compared to the simulation using the modified Nowakowska et al. mechanism[101]. (a) 0.5%, (b) 0.1%, (c) 500 ppm, (d) 200 ppm anisole in Ar.

Figure 4.13 shows the comparison between the predictions from modified model and the measurements of four anisole mixtures. The modified mechanism predicts faster CO formation than the original and yields good agreement with the measurements of 0.5% anisole / Ar mixture at temperature below 1150 K. At higher temperatures (1179–1262 K), good agreement was achieved only for early reaction times, at longer reactions times, lower CO concentrations are predicted. The CO plateau concentration matches also much better in comparison to the original model but the simulations still predict about 10% lower concentrations compared to the measurements at temperatures between 1179 and 1262 K. With decreased initial concentration (Figure 4.13 c and d), the consensus between the experiment and the model becomes better which is a clear indication of the influence of secondary reactions.

A sensitivity analysis based on the modified Nowakowska et al. mechanism [101] was performed to investigate the most important elementary reactions for CO formation. The result of

the analysis for a 500 ppm anisole/ Ar mixture at 1169 K is shown in Figure 4.14. The sensitivity profiles indicate that the reactions R 4.1 and R 4.2 have the strongest positive contributions to the CO formation. Reaction R 4.4 shows the strongest negative influence on CO formation from the beginning of the decomposition and reaction R 4.3 as well as the reaction of C_5H_5 towards naphthalene exhibits a negative influence several tens of microseconds later and about 50% weaker than R 4.4 at the respective reaction time. Besides the reactions R 4.1 and R 4.2, reactions of $C_5H_6 = C_5H_5+H$, $CH_3+CH_3 = C_2H_6$, and $C_5H_5+CH_3$ = methylcyclopentadiene (MCPD) also show positive influence on the CO formation at longer reaction times. These reactions lead to a reduced H-atom production leading to a reduced formation of phenol.

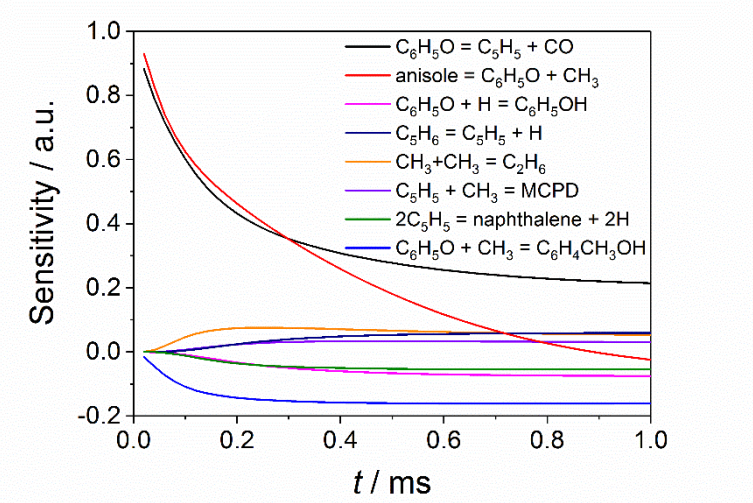

Figure 4.14: Sensitivity of the reactions towards the formation of CO in pyrolysis of 500 ppm anisole/Ar at 1169 K.

The rate constants of the reactions listed in Figure 4.14 in the modified Nowakowska et al. mechanism [101] were varied to investigate their influences on the CO formation. Sensitivity tests of reactions R 4.1–R 4.4 for 1169 and 1103 K are presented in Figure 4.15 and 4.16, respectively, while other reactions showed very minor influences on the CO formation. Table 4.3 lists the rate constants k_1–k_4; k_1 corresponds to a value of the first-order decomposition of anisole at the upper limit in the uncertainty range of the rate constant proposed by Mackie et al. [100], k_2 is measured from this work and agrees to the proposed high-pressure value from Carstensen and Dean [112], k_3 and k_4 were obtained by theoretical calculations in the study of He et al. [113] and Pecullan et al. [114], respectively, to obtain a best fit to their experimental data. CO formation shows high sensitivity towards k_1 and k_2. k_1 strongly controls the first CO rise whereas k_2 influences the overall CO concentration and the formation rate. The final plateau values are sensitive to k_3 and k_4. The simulated CO profiles achieve the best fit to the measurements at both 1169 and 1103 K with 0.5 k_4. Pecullan et al. [114] already reported an over-

prediction of cresol formation by a factor of two compared to their experimental data performed in an atmospheric pressure flow reactor using the proposed k_4 in their mechanism, which is consistent with this study.

Table 4.3: Rate constants for reactions R 4.1–R 4.4 used in modified Nowakowska et al. mechanism. Rate constants are given in the form $k = A\,T^n \exp(-E_a/RT)$ where A has units of cm, mol, and s. T has unit of K, and E_a has unit of kJ/mol.

Reaction	A	N	E_a	Ref
(1) $CH_3 + C_6H_5O = C_6H_5OCH_3$	5.0×10^{12}	0	0	[100]
(2) $C_6H_5O = CO + C_5H_5$	9.1×10^{13}	0	220.3	this work
(3) $C_6H_5O + H = C_6H_5OH$	2.0×10^{14}	0	0	[113]
(4) $C_6H_5O + CH_3 = C_6H_4CH_3OH$	2.31×10^{73}	–17.37	162.3	[114]

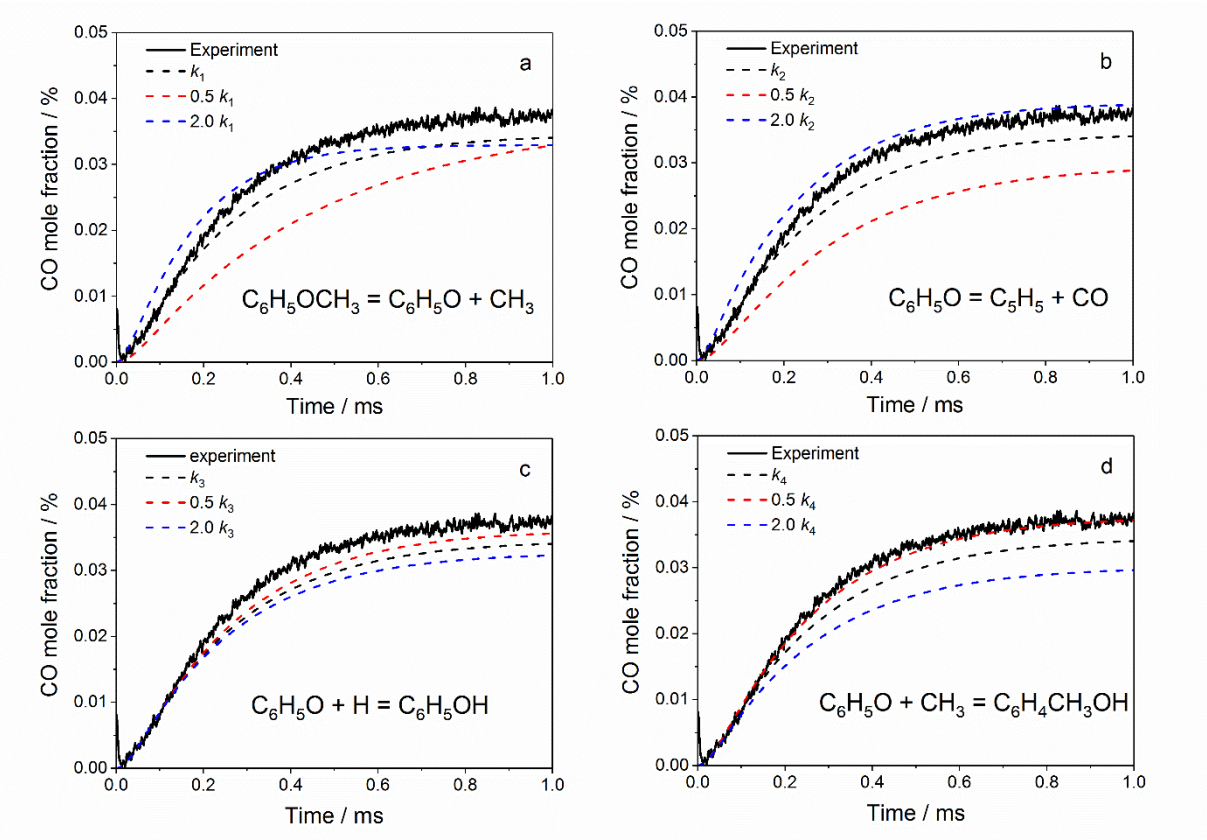

Figure 4.15: Sensitivity analysis of mixture 500 ppm anisole/Ar at 1169 K and 1.38 bar by varying the rate constants of reaction R 4.1–R 4.4 (k_1–k_4) by a factor 0.5 and 2.

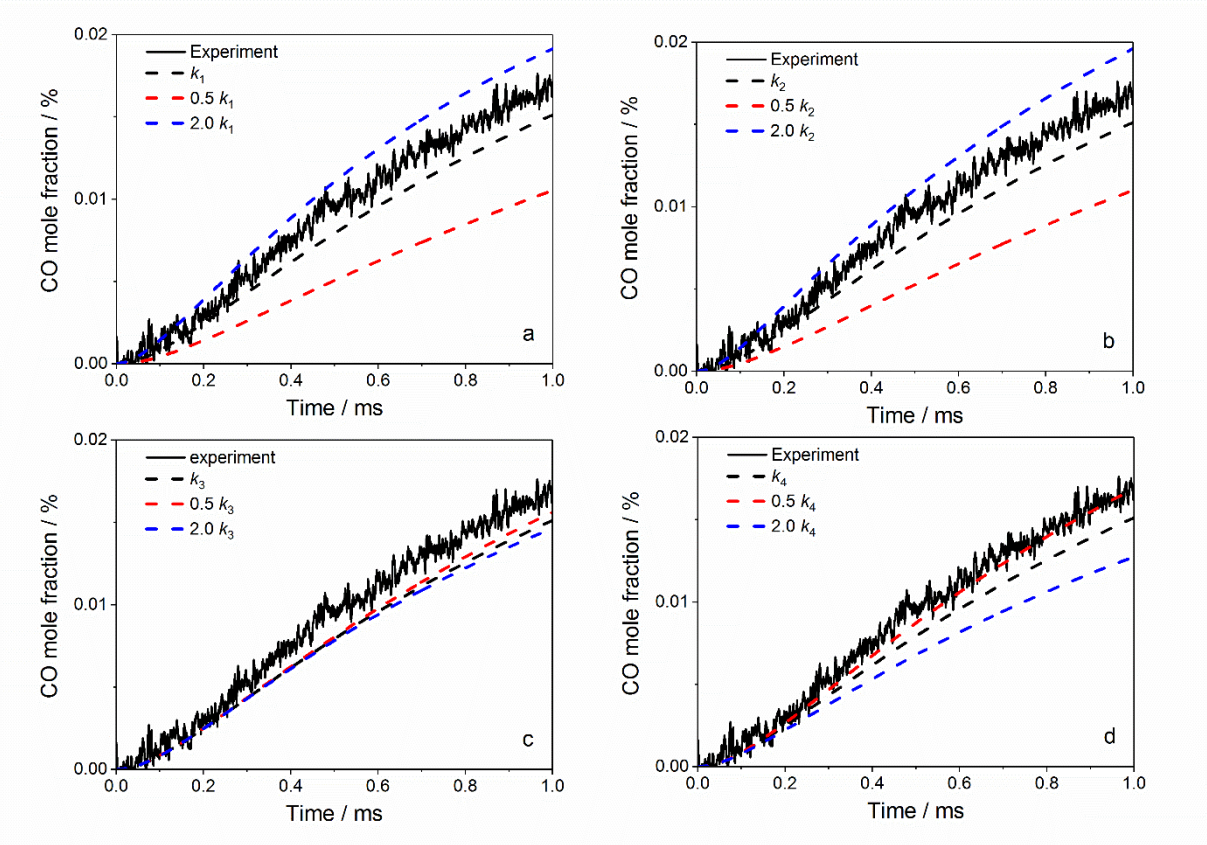

Figure 4.16: Comparison between calculated and measured CO concentration profiles: Brute-force sensitivity analysis to reactions R 4.1–R 4.4 of 500 ppm anisole/Ar mixture at 1103 K and 1.43 bar by varying k_1–k_4 by a factor 0.5 and 2.

4.2.3. Conclusions

Pyrolysis of anisole was investigated behind reflected shock waves at temperatures of 1000–1270 K and pressures of 1.3–1.6 bar. CO mole fractions were measured with quantum cascade laser MIR laser absorption spectroscopy. The CO absorption line pair P(8)/R(21) was selected for direct-absorption concentration measurements and ratiometric temperature measurements. CO concentration–time histories with anisole/Ar mixtures ranging between 200 and 5000 ppm were measured and compared to simulations based on the mechanism of Nowakowska et al. [101]. The mechanism predicts slower formation and lower plateau concentration values of CO compared to the experiments.

Rate constant of unimolecular decomposition of the phenoxy radical with allyl phenyl ether as phenoxy source was measured behind reflected shock waves using CO absorption diagnostics to support the findings of anisole pyrolysis. Measurements were compared to literature data of two experimental investigations from Lin and Lin [99] and Frank et al. [109]. Rate constants

from these two sources were found to be lower than the measurements in this study. The potential energy surface (PES) of C_6H_5O dissociation obtained from Carstensen and Dean [112] has been re-evaluated at the G4 level of theory. The *ab initio*-based $k(p, T)$ values are in very good agreement with the present experimental results.

By integrating the obtained rate constant of phenoxy decomposition of this study into the mechanism of Nowakowska et al. [101], good agreement was achieved for the prediction of CO formation at early stages of anisole pyrolysis although some deviations in the final CO concentrations still persist. According to the brute-force sensitivity analysis based on the modified Nowakowska model, the simulation can predict the final CO concentration excellently for all the measurement conditions in this study by reducing the k_4 by a factor of 2. Further study on k_4 is therefore recommended.

4.3. Soot formation in the pyrolysis of C_2H_2 and C_6H_6

This chapter mainly represents the contents of the peer-reviewed publication 5 (cf. list of own publications), coauthored by Drakon et al. In this work, extinction and temperature measurements were performed to study the temperature dependence of the soot formation in the pyrolysis of acetylene and benzene. Carbon-concentration normalized optical density and induction time were investigated in the extinction measurements. Temperature measurements were performed using CO absorption spectroscopy by adding small amount of CO in the studied mixtures. The measured temperatures were compared to the simulations performed by the co-author A. Drakon. The influence of H_2, O_2, and CH_4 on the soot formation in the pyrolysis of acetylene and benzene was obtained by combining the results from both extinction and temperature measurements.

4.3.1. Motivation

Soot formation during the combustions has been subject of intense scientific interest for several decades. Incomplete combustion of hydrocarbons contributes to the production of carbon monoxide, hydrogen, partially-oxidized hydrocarbons, and soot. As flames have been used for manufacturing carbon black for a long time, soot was identified as combustion pollutant in 1970s due to its negative health effects. Direct investigations of soot formation in the pyrolysis or oxidation of complex hydrocarbons, i.e. commercial fuels are difficult due to their numerous compounds and complex kinetics. Hence, hydrocarbons that contain few carbon atoms such as acetylene (C_2H_2) and ethylene (C_2H_4) that are also products of decomposition of large hydrocarbons are widely applied to investigate the chemical kinetics of the soot formation [124].

Carbon particle formation in pyrolysis of hydrocarbons at elevated temperatures has been studied experimentally and theoretically during the recent decades [125, 126]. Along with the continuous attempts to reduce the soot yield and thus to increase the efficiency and cleanliness of combustion processes, the applications for carbon nanoparticles in manufacturing (rubber, dyes, plastics, etc.) are also subject of increasing interest. Detailed kinetics mechanisms both for pyrolysis initiation and soot growth are developing and require new experimental data.

The carbon particles that are present in soot, have a core forming from polyaromatic hydrocarbons (PAH) [127] that are assumed to form in hydrogen-abstraction acetylene-addition (HACA) reaction paths [128]. Benzene (C_6H_6) represents a first aromatic ring and its formation is con-

sidered as one of the initial steps towards PAH growth, while acetylene (C_2H_2) is a major product of decomposition of several hydrocarbons and plays an important role as a building block towards soot formation. Therefore, C_2H_2 and C_6H_6 are the species of interest in the present investigation.

The influence of H_2 on the carbon-particle growth in C_2H_2 pyrolysis has been studied by several groups [11, 126], decrease of final particle sizes and optical densities as well as C_2H_2 consumption have been reported. However, H-rich methane (CH_4) and oxygen (O_2) are also interesting additives that may influence the soot formation.

Several studies have investigated the temperature dependence of soot formation during the pyrolysis of C_2H_2 and C_6H_6 [133, 134], where no accurate temperature measurements were applied and thus high uncertainties were reported. In the present work, highly accurate time-resolved temperature and extinction measurement were applied, the temperature dependence of the soot yield in C_2H_2 and C_6H_6 pyrolysis doped with H_2, O_2, and CH_4 were studied, which contributes to the understanding of the influence of their species on the early stage of soot formation.

4.3.2. Results and discussion

18 mixtures were applied for this investigation (Table 4.4). Along with the studied soot precursors and doping additives, some mixtures containing CO as a tracer for temperature measurements and helium (He) for the acceleration of CO vibrational relaxation. Helium was not used for mixtures containing H_2 as it provides the required high relaxation efficiency itself.

For the time-dependent observation of carbon-particle formation, laser light extinction measurements were carried out. Beams of a 2 mW conventional HeNe laser and a 2 mW distributed-feedback (DFB) diode laser (Nanoplus) were applied for extinction measurements at 633 nm and 2.7 µm, respectively. A photodiode detector (DET10A, Thorlabs) and a TE-cooled IR photovoltaic detector (VIGO) were used to receive the signal from HeNe laser and DFB laser, respectively. Bandpass filters centered at 632.8 nm (FWHM 10 nm) and at 2.75 µm (FWHM 200 nm) were installed in front of either detector to suppress the detection of unwanted emission and interference of ambient light. Due to the spectral width of the IR filter and the strong emission of the formed soot, an additional detector had to be used for recording emission signal, which was subsequently subtracted during analysis. The signal ratio due to soot emission in the two channels was determined during calibration experiments. The schematic of the extinction measurements is shown in Figure 4.17.

Table 4.4: Gas mixtures for the shock tube measurements and their denotations

Case	Mixture	Case	Mixture
A0	10%C_2H_2+Ar	B0	1%C_6H_6+Ar
A1	10%C_2H_2+2%O_2+Ar	B0’	2%C_6H_6+Ar
A2	10%C_2H_2+5%H_2+Ar	B1	1%C_6H_6+1%O_2+Ar
A2’	10%C_2H_2+10%H_2+Ar	B1’	2%C_6H_6+2%O_2+Ar
A3	10%C_2H_2+5%CH_4+Ar	B2	1%C_6H_6+1%H_2+Ar
A4	10%C_2H_2 +0.8%CO+20%He+Ar	B3	1%C_6H_6+1%CH_4+Ar
A5	10%C_2H_2+2%O_2 +0.8%CO+20%He+Ar	B4	1%C_6H_6 +0.5%CO+20%He+Ar
A6	10%C_2H_2+5%H_2 +0.5%CO+Ar	B4’	2%C_6H_6 +0.8%CO+20%He+Ar
		B5	2%C_6H_6+2%O_2 +0.8%CO+20%He+Ar
T0	0.5%CO+20%He+Ar	B6	1%C_6H_6+1%H_2 +0.8%CO+20%He+Ar

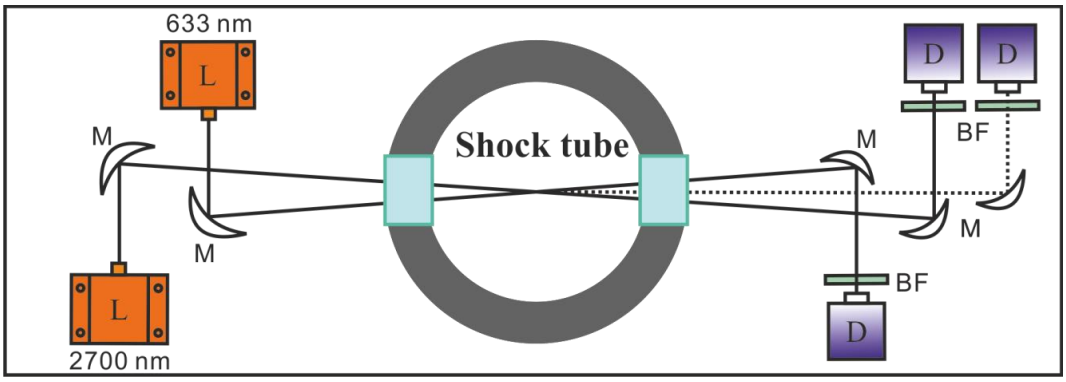

Figure 4.17: Schematics of extinction measurement; L: laser, D: detector, M: mirror, BF: bandpass filter

Figure 4.18a shows a typical extinction signal of 633 nm obtained during pyrolysis of a C_6H_6/Ar mixture at 2200 K and 1.9 bar. The strong peaks in the beginning of the signal indicate the arrival of incident and reflected shock waves in the measurement plane due to the deflection of the laser beam on the density gradients of a shock wave front. The extraction of absolute values

of soot yield from the extinction signals requires the assumption that all particles have identical optical properties. Instead, here we present the [C]-normalized optical density D_λ calculated from the Beer-Lambert law

$$D_\lambda = \frac{\ln(I_0 / I)}{[\mathrm{C}] \cdot l} \quad , \tag{4.1}$$

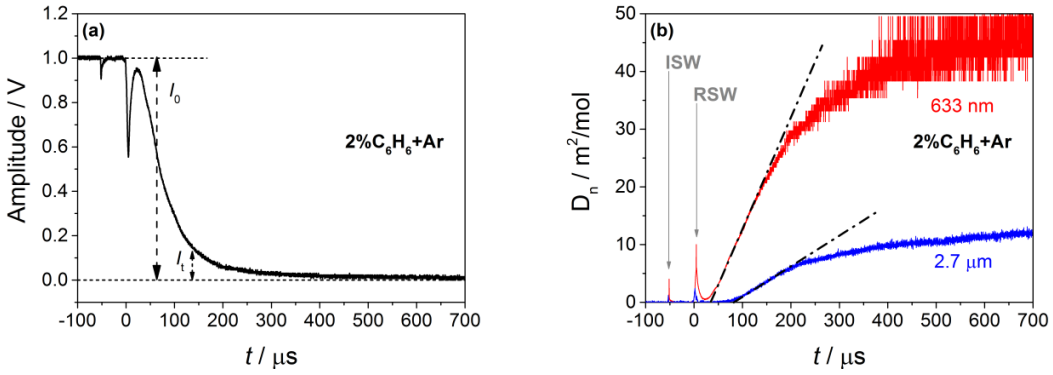

Figure 4.18: Typical signal of the extinction measurement in mixture B0'; a): raw data at 633 nm; b): normalized optical density at 633 nm and 2.7 µm.

where [C] is the total carbon concentration in the system. Figure 4.18b represents typical time-dependent D_λ that allows extracting the induction time τ of particle formation, which is one of the main kinetic characteristics of soot formation. The absolute value of τ was defined as the intersection of the inflectional tangent of the carbon particle optical density profiles with the time axis. The following stage of the process is characterized by the growth of soot yield. Due to the low-pressure range studied in the present work (1.5–2.7 bar), soot growth was slow and the final value of the soot yield was not reached during the test time in the shock tube. Thus, values of the optical density at τ = 700 µs were analyzed. The normalized optical densities measured at the reaction time of 700 µs in pyrolysis of mixtures without seeded CO are plotted as function of temperature in Figure 4.19 and 4.20. The pyrolysis of C_2H_2 mixtures was investigated at 1200–2600 K and 1.5–2.7 bar, optical densities at both 633 nm and 2.7 µm were measured and are presented in Figure 4.19 a and b, respectively. The pyrolysis of C_6H_6 mixtures was studied at 1400–2600 K and 1.5–2.7 bar, optical densities were only measured at 633 nm and are summarized in Figure 4.20.

The well-known bell-shaped temperature dependence of the soot yield demonstrated in Figure 4.19 and 4.20 has been observed in shock-tube pyrolysis of hydrocarbons [129] as well as in flames [130]. It can be seen that in the pyrolysis of C_2H_2, while H_2 and CH_4 affect mainly the maximum value of the optical density, O_2 addition results in a significant shift (~400 K) of the

"bells" towards lower temperatures. IR measurements are sensitive to larger and more mature soot particles than measurements in the VIS due to the longer wavelength. They therefore provide lower optical density values and longer induction times (see Figure 4.18 and 4.19) compared to measurements at 633 nm. Nevertheless, the general feature of the obtained temperature dependences ("bells") seems to not depend on wavelength used for measuring extinction. Due to the complexity in determining accurate optical properties of particles, an analysis of IR extinction measurement results was limited in present work, but these data could be an additional basis for further verifications of the developed kinetics mechanisms.

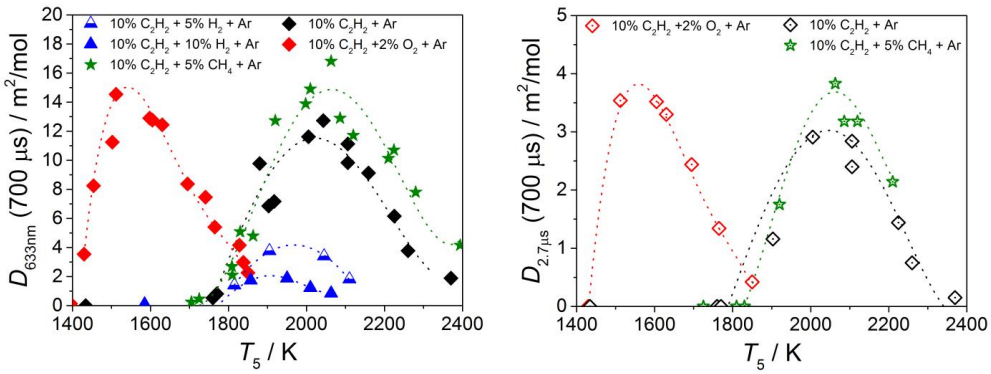

Figure 4.19: [C]-normalized optical density at 633 nm and 2.7 µm measured in the acetylene mixtures A0–A3' at τ = 700 µs.

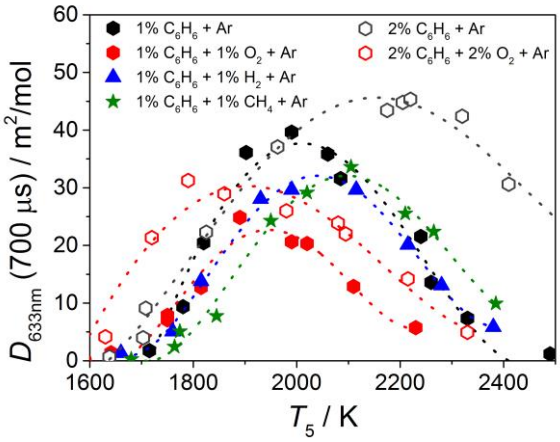

Figure 4.20: [C]-normalized optical density at 633 nm measured in the benzene mixtures B1–B3 at τ = 700 µs.

H_2, O_2, and CH_4 showed similar influences on the optical density in the pyrolysis of C_6H_6 as found in C_2H_2 where the shift of the temperature dependence caused by adding O_2 is about 100 and 300 K towards lower temperatures for mixtures with 1 and 2% C_6H_6, respectively. Moreover, by increasing the C_6H_6 concentration from 1% to 2%, the measured optical densities

showed a higher maximum value and a shift of the dependence towards higher temperatures (~ 200 K).

As another major characteristic of the particle-formation process, the induction time of particle inception in the pyrolysis of C_2H_2 and C_6H_6 were analyzed. The temperature dependence of the induction time τ obeys the Arrhenius-like law[131]

$$\tau = A\exp(E/RT)[\mathrm{C}]^{-n} \quad . \tag{4.2}$$

Therefore, the values of τ at various pressures and precursors (C_2H_2 and C_6H_6) concentration were normalized to the full carbon concentration [C] in investigated mixture as suggested in the recent paper [126] and [130] with n = 1 [126]. The obtained results $\tau \cdot [\mathrm{C}] = f(T)$ of the acetylene mixtures are presented in Figure 4.21 together with the results of literature [126] obtained at higher p_5 pressures (4–7 bar) in the mixtures with different acetylene and oxygen concentrations. One can see that the suggested approach allows normalizing of data obtained in a wide range of pressure and concentrations. As shown in Figure 4.21, H_2 and CH_4 exhibit no effects on the normalized inductions time in both Ref [132] and this study. The presence of O_2 shifts the temperature dependence of τ to the lower temperatures with increase of O_2 concentration but the general behavior of τ is barely affected. Similar effects on the temperature dependence of τ are observed in the benzene pyrolysis, the data obtained in benzene mixtures B0–B1' and B3 are shown in Figure 4.22. One need to note that the temperature dependence of τ of 2% C_6H_6 mixture also shifts towards lower temperatures comparing to the 1% mixture.

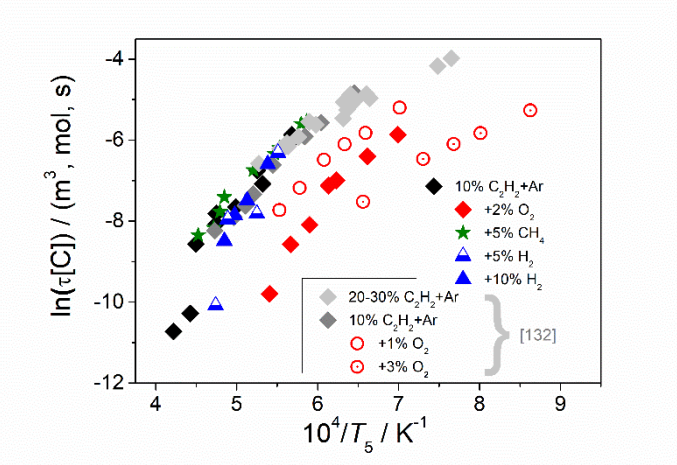

Figure 4.21: Temperature dependence of induction times of soot formation in mixture A0–A3.

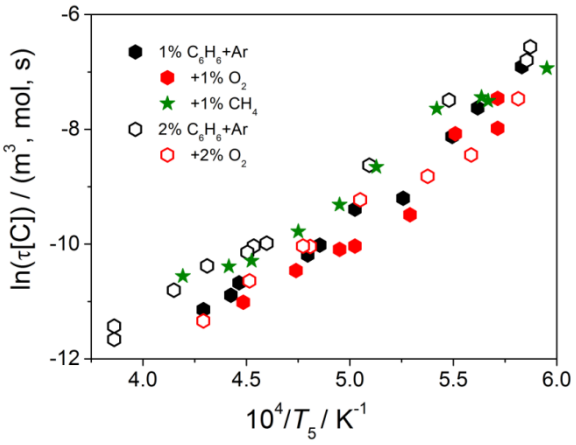

Figure 4.22: Temperature dependence of induction times of soot formation in benzene mixtures B0–B1' and B3.

To rationalize the experimental finding in the extinction measurements, the temperature histories in the pyrolysis of C_2H_2 and C_6H_6 were measured by the method introduced in section 2.3.5. It should be mentioned that the temperature measurements were limited by the induction time of soot particle formation because the setup could not deal with the strong extinction of laser signal in sooty media. A possible approach for the measurements in a sooty media as introduced in section 3.3 is the use of the third reference off-band channel for signal normalization, which was not applied in this study.

Typical absorption–time histories of the two CO-absorption lines (P(8) and R(21)) and the inferred temperature profile of shock-heated gas mixture A5 at 1132 K and 2.1 bar are shown in Figure 4.23. The schlieren spikes at the beginning of the signals indicate the arrival of the incident and reflected shock waves. The absorbances of both lines show first plateau values with 100 µs duration which represent the absorbance during the induction time and then are followed with increasing values which were due to the extinction of the signals during the soot formation. The measured temperature profile shows similar behavior where the measured temperature also has first a plateau value during the induction time which shows very good agreement compared to the T_5 calculated from the shock velocity and the followed temperature increase is attributed to the uncorrected absorbance signals and cannot be used in the later analysis.

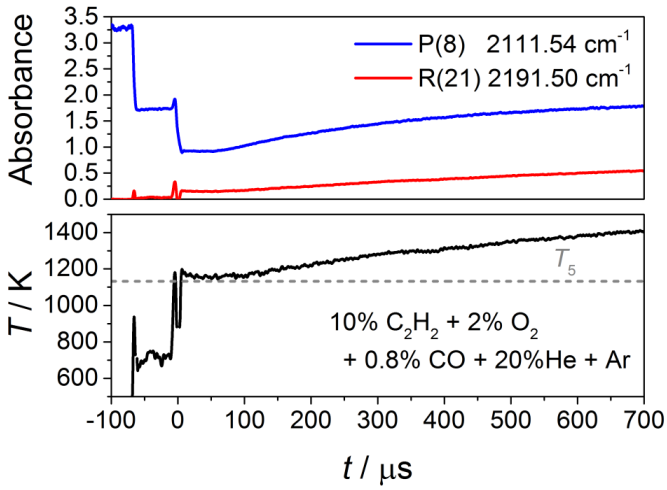

Figure 4.23: Typical absorption profiles for the two CO-absorption lines P(8) and R(21) and the inferred temperature profile in mixture A5. Dotted line represents "frozen" calculated temperature T_5.

To support the experimental finding in the temperature measurements, simulations were attempted to represent the temperature profile. However, detailed kinetics modeling was beyond the scope of the present work due to high complexity of hydrocarbons pyrolysis and oxidation kinetics and carbon particle formation. Only the heat effects of C_2H_2 oxidation were simulated using a modern kinetics mechanism [133] and the ChemKin software package [134]. Calculations were performed with the approximation of constant pressure with a time-step of 0.5 μs resulting in time profiles of the concentrations of the investigated species.

It was previously reported [135] that the given mechanism [132] provided a satisfactory agreement with measured ignition delay times only for highly diluted stoichiometric C_2H_2/O_2 mixtures (i.e. containing ~1% C_2H_2). For less diluted mixtures that are similar to the mixture A1, the measured induction times were noticeably shorter than those obtained in the simulations. One of the possible reasons for this discrepancy is the contribution of bimolecular and trimolecular reactions with the participation of C_2H_2 and its decomposition products increase with their concentration.

Acetylene mixtures A4–A6 and benzene mixtures B4–B6 are investigated at 900–2600 K and 1.5–2.7 bar and the obtained temperature profiles are presented in Figure 4.24 and 4.25 for the mixtures of C_2H_2 and C_6H_6, respectively.

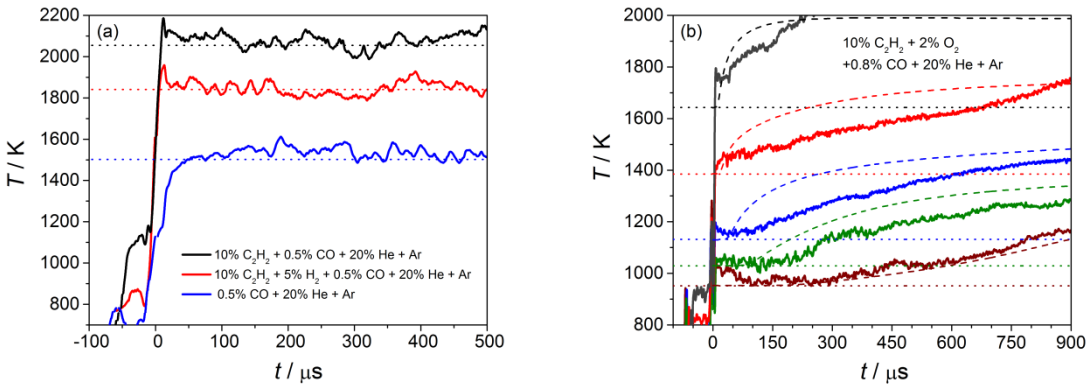

Figure 4.24: Measured temperature profiles; a): in test mixture T0 and mixtures A5 and A6, dotted lines represent initial temperature T_5; b): in mixture A5 at various initial temperatures T_5 (dotted lines), dashed lines represent modeling results.

Figure 4.24a shows the temperature profiles of C_2H_2 pyrolysis with and without the presence of H_2. The measured temperatures show good agreement to the calculated "frozen" temperature T_5 (dotted lines) and demonstrate no heat effects within the observation time. As contrast, with the addition of O_2, the temperatures during the pyrolysis result in a significant heat release (~200 K) and accelerate with increasing T_5. The temperature variations in the pyroysis of C_2H_2 mixture A5 were simulated using the kinetics mechanism from [133] and were plotted together with the measurements in Figure 4.24b. The simulations showed reasonable agreement to the measured data where the model predicts faster temperature increase at the beginning of the reactions but the final temperatures at the end of induction time from simulations and measurments are close to each other.

The measured temperature–time histories of benzene mixtures B4' and B5 are depicted in Figure 4.25 a and b, respectively, and compared only to the calculated T_5 since no suitable kinetics model is available to simulate the temperature variations. In the pyrolysis of the B4' mixture, a drastic drop of the temperature due to decomposition of initial hydrocarbon molecules has been observed from 1857 K. This temperature drop can be only partially followed in the measurement at higher T_5 due to the ultra-fast endothermic process. The plateau value of measured temperature is 400 K lower than the calculated initial T_5 for the measurement at 2600 K.

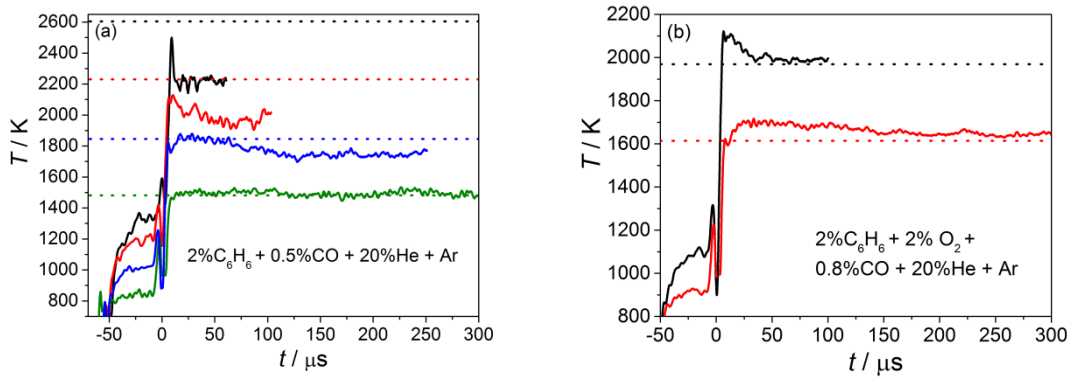

Figure 4.25: Temperature profiles measured in mixture B4 and B5 at various initial temperatures T_5 (dotted lines).

In the study of the B5 mixture, the measured temperatures show first a significantly higher value than T_5 and then decrease over time. In the measurement at T_5 = 1620 K, the plateau values of the temperature are still higher than T_5 and the temperature drops strongly after reaching its peak value. For the measurement at higher T_5 (1967 K), a stronger temperature drop was detected that is similar to the finding for mixture B4', the plateau value of measured T at the end of the induction time is close to the T_5. This behavior of the temperatures can be explained due to the presence of O_2 in mixture B5 that introduced a fast exothermic process that was then followed by a strong endothermic process when all the O_2 was consumed.

Figure 4.24 and 4.25 show that due to the heat release or the endothermic process or a combination of both processes, the actual temperatures at the end of the induction time can differ notably from the calculated "frozen" temperatures T_5. Note that in presence of O_2, temperature rises much earlier than the end of induction time of soot particle formation. That means that the soot formation proceeds at temperatures significantly different from T_5. In Figure 4.26 the value of temperature differences $\Delta T = T_{meas} - T_5$ were plotted as function of T_5 where T_{meas} is the measured temperature value just before the end of induction time (or at τ = 700 µs in case τ was longer) and then interpolated providing a calibration curve for recalculating given T_5 to expected T_{meas}. The grey points represent data of a recent work [136] which show a larger uncertainty because they are based on temperature measurements using emission–absorption thermometry with a generalize line-reversal scheme at 589 nm. The model of [133] was used to calculate the temperature difference for C_2H_2 mixture A1 and the simulated data are plotted together (dashed line) with the measurements for comparison. The simulated ΔT reasonably agrees with experimental data, particularly reproducing the feature of non-linear increase of ΔT, though the observed rate of temperature rise seems to be lower than predicted one.

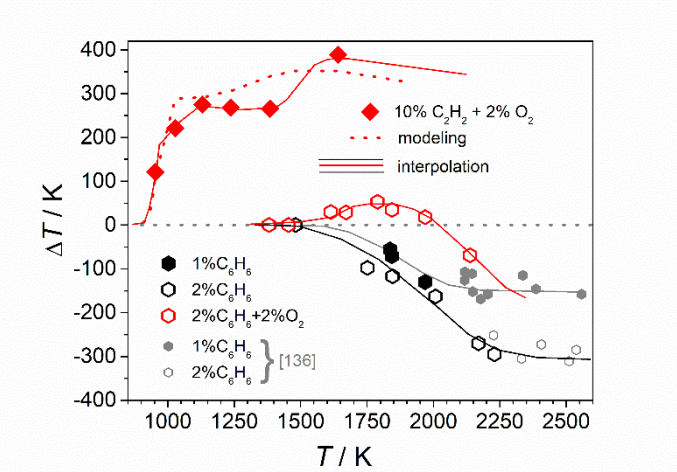

Figure 4.26: Dependence of the measured temperature at the end of the induction time for soot formation on calculated "frozen" temperature.

The temperature dependence of the optical density and the induction time were then re-evaluated using the obtained calibration curves. In Figure 4.27 the values of normalized optical density for mixtures A0, A1, B0, B0', and B1 are presented as function of measured temperature T_{meas} and Figure 4.28 presents the dependence of induction time on T_{meas}. It can be seen that such an approach eliminates the observed temperature shift almost completely. Thus, it can be concluded that the observed shifts are not related to major changes in soot formation kinetics but rather to heat effects of pyrolysis and oxidation of the studied hydrocarbons. The shift of the temperature dependence of the induction time determined by the fast oxidation processes is described quite satisfactory. Small residual shifts of the dependence of the soot yield can be attributed to the heat release of oxidation processes occurring after the induction time, which could be neither detected by the used diagnostics nor predicted by the mechanism [133] as it lacks reactions related to the formation of complex PAH and soot.

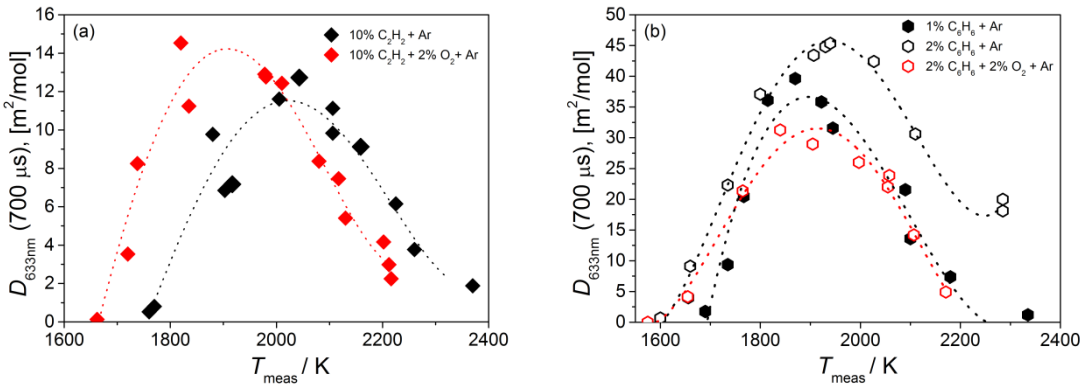

Figure 4.27: Soot yield in acetylene and benzene mixtures as a function of measured temperatures; a): mixtures A0 and A1; b): mixtures B0, B0', and B1'.

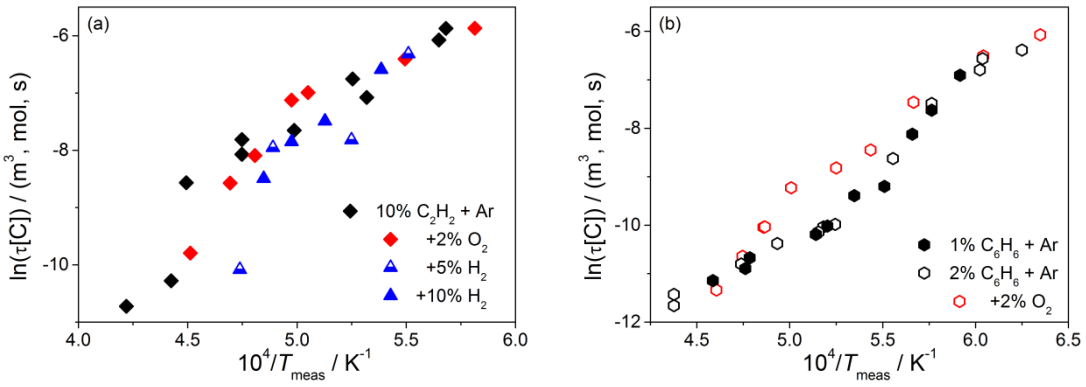

Figure 4.28: Induction time of soot formation in acetylene and benzene mixtures;
a): mixtures A0–A2; b): mixtures B0, B0', and B1'.

As demonstrated in Figure 4.19 and 4.20, in the presence of 1–10% H_2, the measured optical densities in both acetylene and benzene mixtures decreased, i.e. the soot yield was suppressed, while no notable shift of the temperature of maximum soot yield was observed. Presumably, the elevated H_2 concentration leads to the consumption of radicals necessary for soot build-up [132]. It should be noted that the addition of methane as a hydrogen-rich compound, while expectedly decreases the soot yield during benzene pyrolysis, leads to its increase in acetylene pyrolysis. One possible explanation suggests that methane provides additional channels (e.g., acetylene + methylene radical towards propargyl radical and further towards phenyl radical) of forming products where acetylene attachment could occur thus accelerating the HACA mechanism [128]. Contrary to acetylene, benzene is itself an aromatic compound and these channels are not important, thus the soot-inhibiting effect of hydrogen dominates. Similar opposite influence of O_2 addition on the soot yield in acetylene and benzene was also observed and may have similar nature.

4.3.3. Conclusions

The influences of H_2, O_2, and CH_4 additives on soot formation during the pyrolysis of C_2H_2 and C_6H_6 was experimentally studied at 1400–2600 K and 1.5–2.7 bar behind reflected shock waves. The temperature dependence of the soot yield and the induction time was investigated using extinction measurement and two-line absorption thermometry. An essential temperature change during the induction time of soot formation was observed in most of the mixtures. This phenomenon is attributed to the thermochemistry of hydrocarbon oxidation and pyrolysis. Simulations of the temperature behavior in C_2H_2/O_2 mixtures based on the modern kinetics mechanism confirm the experimental observations. An effect of contrary influences of CH_4 and O_2 admixture compared to H_2 on the soot yield in acetylene and benzene is notable.

5. Outlook

In this thesis, direct absorption method with fixed-wavelength spectroscopy has been applied for accessing mid-IR absorption of CO. The accuracy of this method strongly depends on the line strength of the selected lines, i.e. when the concentration of the target species is very low or the ambient interference is strong, the uncertainty of the measured absorbance increases, which leads to large error on subsequently obtained temperature and concentration information. Wavelength-modulation spectroscopy (WMS) is considered as an alternative diagnostic technique [137-139] that was demonstrated as being free from the background signal and therefore can achieve higher sensitive detection by providing high signal-to-noise ratio (SNR). For WMS, the wavelength of the laser is not fixed but modulated rapidly. The WMS-*nf* method uses *n* times of frequencies for comparison and *n* is recommended between 2 to 6 [138]. The first and second harmonics of the transmitted laser intensities are called WMS-1*f* and -2*f* signals, respectively. By normalizing the 2*f* signal over the 1*f* signal, the detection is more sensitive to the absorption line strength and insensitive to low-frequency noise. Higher harmonic signals can also be detected and help in further reducing interference and resolving overlapping gaseous species, thus providing more accurate information of the trace gas species. Normally, 2*f* detection is the best selection because it induces lower residual amplitude modulate noise than the 1*f* detection and its peak signal level is much higher than higher harmonic signals [139]. Therefore, the WMS-2*f*/1*f* signals yield high SNR and allow measurement of small values of absorption with high sensitivity and selectivity [139].

In this work, CO and temperature are the main targets during the kinetics experiments. As introduced in section 3.3, TDLAS can provide sensitive detection of single species but the setup is limited by the space and optical accesses, the setup of fiber-based multi-line spectrometry solves the limitation and extends the possibility of TDLAS to multi-species detection or in harsh environments such as sooting environment. For the combustion studies, besides CO, other primary products like H_2O and CO_2 are also attractive targets and their concentrations indicate the overall performance of the combustion systems. H_2O and CO_2 have strong absorption near 1.5 and 4.2 μm [57, 140], respectively, and lasers accessing these wavelengths are commercially available. Moreover, studies of the neat hydrocarbons or fuel blends need inputs of their concentration–time histories. Several hydrocarbons such as methane, ethylene, propane, and multi-component fuels like JP-10 and jet-A have strong absorption near 3.39 μm [141]. Furthermore, sufficient absorptions of nitrogen oxide (NO) and methanol (CH_3OH) have been found near 5.2 and 9.6 μm, respectively [142, 143]. By coupling these single absorption transitions into the

fiber-based multi-line spectrometry, multi-species and temperature sensing can be achieved and those measured species–time histories and rate data provide additional opportunity to test and validate large reaction mechanisms and refine their component sub-mechanisms.

Additionally, the TDLAS used in this thesis was applied at relative low pressures (< 3 bar). In practical applications, pressures can be much higher (e.g., 20–50 bar) and the absorption measurements may be affected by more interferences due to line-broadening. To rule out the interferences and obtain reliable data, fiber-based multi-line spectrometry must be applied. Depending on different conditions, combinations of CO–H_2O, CO–CO_2, or CO–H_2O–CO_2 absorption bands should be the basic setup in the fiber-based multi-line spectrometry.

6. Conclusions

Combustion systems are widely applied in modern industry. The optimization and improvement of the efficiency and reduction of pollutants are very important to increase energy efficiency and sustainability. This requires in-depth understanding of the underlying fundamental chemical processes. Temperature is one key parameter during combustion which relates to interpretation of important phenomena such as ignition and soot yield. Carbon monoxide as a primary product of hydrocarbon oxidation is an attractive target in combustion studies since its concentration can be interpreted to indicate the completeness of combustion or to control the operation of many combustion systems. Therefore, measurements of carbon monoxide and temperature are useful inputs for developing and validating chemical reaction mechanisms that are used for the development and optimization of practical combustion systems.

Tunable diode-laser absorption spectroscopy (TDLAS) is highly attractive for combustion and propulsion applications due to its non-intrusive nature, fast-time response, and *in situ* measurement capability. Shock tubes are versatile tool for studying the kinetics of high-temperature reaction are well established to study the chemistry and physical research by providing a uniform environment covering a wide range of temperatures and pressures. Therefore, shock tubes coupled with TDLAS are powerful tools for studying the gas-phase kinetics by offering well-controlled reaction conditions and time-resolved measurements of species concentration and temperature.

In this thesis, TDLAS for CO and temperature measurements using rotational transitions in the fundamental vibrational band of CO near 4.7 μm was set up and applied in gas-phase kinetics investigations for pyrolysis and oxidation of hydrocarbons behind reflected shock waves. Two well-studied candidate lines centered at 2059.91 cm^{-1} (P(20)) and 2191.50 cm^{-1} (R(21)) and a new candidate line centered at 2111.54 cm^{-1} (P(8)) were selected and accessed by three quantum cascade lasers. The spectroscopic parameters of the selected lines including line strengths and broadening coefficients $2\gamma_{Ar\text{-}CO}$ were measured in the temperature range between 900–2000 K behind reflected shock waves using $CO/H_2/Ar$ mixtures. The measured data show very good agreement compared to the literature values.

The temperature sensitivity of the new proposed line pair P(8)/R(21) was analyzed and validated first in a shock tube using a non-reactive $CO/H_2/Ar$ mixture at temperatures between 900 and 1800 K. The measured temperatures showed very good agreement with the calculated values using a 1 D shock-tube mechanism with a maximum deviation of 1.8%. The line pair was

then validated in the pyrolysis and oxidation of 3-pentanone and demonstrated accurate sensing of temperature and CO concentration.

The validated line pairs were then applied in the investigated reacting systems in this work that involve: (i) the polygeneration processes of methane (CH_4) / oxygen (O_2) under a fuel-rich conditions enhanced with additives of dimethyl ether (DME) and *n*-heptane; (ii) the thermal decomposition of anisole ($C_6H_5OCH_3$) that is a surrogate for kinetics studies of biomass combustion and was recently identified as a fluorescence tracer for fuel/air mixing studies based on laser-induced fluorescence (LIF); (iii) influence of hydrogen (H_2), CH_4, and oxygen (O_2) additives on soot formation during the pyrolysis of acetylene (C_2H_2) and benzene (C_6H_6).

The CO absorption line pair P(20)/R(21) was applied to investigate partial oxidation of CH_4 under fuel-rich condition (ϕ = 2) with DME and *n*-heptane as additives at 1600–2000 K and 1.3–1.6 bar behind reflected shock waves. CO mole fractions and temperatures were measured and compared with simulations based on mechanisms of Yasunaga et al. [85], Zhao et al. [87], and Burke et al. [86] for CH_4/DME mixtures and Mehl et al. [90] for CH_4/*n*-heptane mixtures. Good agreement was found between all simulations and measurements. However, none of the mechanisms is optimized for chemical conversion reactions and even small deviations in the kinetic schemes influence the predicted formation of potential product species. Moreover, DME as additive activates the reactions earlier which is attributed to the enhanced OH production. CH_4 conversion proceeds mainly through the reaction $CH_4 + OH = CH_3 + H_2O$ which consumes OH radicals. Our results show that additives can enable reactions at reduced temperatures if they produce additional OH radicals. When testing alternative additives their propensity to form OH radicals needs to be considered.

The CO absorption line pair P(8)/R(21) was applied in the study of thermal decomposition of anisole at 1000–1270 K and 1.3–1.6 bar. CO-concentration time histories in reacting systems with anisole mixtures ranging between 200 and 5000 ppm were measured and compared to simulations based on the mechanism of Nowakowska et al. [101]. The mechanism predicted slower formation and lower plateau concentrations of CO in comparison to the experiments which is attributed to incorrect rate constants of the unimolecular decomposition of the phenoxy radical towards CO and cyclopentadienyl radical (k_2). As large discrepancies were found between the previous experimental and theoretical studies of k_2, k_2 was measured in this study using allyl phenyl ether as phenoxy radical precursor at 970–1170 K and 1.4 bar. The obtained rate $k_2 = 9.1\times10^{13} \exp(-220.3 \text{ kJ mol}^{-1}/RT)\text{s}^{-1}$ is significantly higher than that reported by Lin and Lin [99], Frank et al. [109], and Carstensen and Dean [112]. Moreover, the potential-energy

surface of phenoxy radical was re-evaluated at the G4 level of theory and the rate constants determined from unimolecular rate theory showed very good agreement with the present experiments. By integrating the obtained k_2 in this work into the mechanism of Nowakowska et al., good agreement is achieved for the prediction of CO formation at early stages of anisole pyrolysis although some deviations in the final CO concentration persist. The deviations are attributed mainly to the bimolecular reaction of phenoxy and methyl radical toward cresol.

The CO absorption line pair P(8)/R(21) was further applied to monitor temperature–time histories during the pyrolysis of acetylene and benzene with H_2, O_2, and CH_4 as additives at 1400–2600 K and 1.5–2.7 bar. Extinction measurements at 633 and 2700 nm were conducted to obtain the optical densities and the induction times of soot formation during pyrolysis. An essential temperature change during the induction time was observed in most of the studied mixtures. This phenomenon is attributed to the thermochemistry of hydrocarbon oxidation and pyrolysis. Simulations of the temperature behavior in C_2H_2/O_2 mixtures based on kinetics mechanism [133] confirm the experimental findings. Addition of H_2, O_2, and CH_4 showed no effect on the temperature dependences of the optical density and the induction times. H_2 strongly suppressed the soot yield in both acetylene and benzene pyrolysis. In presence of CH_4, particle formation in acetylene mixtures was increased whereas in benzene were decreased. These contrary effects are attributed to the fact that CH_4 molecules provide additional channels (e.g., acetylene + methylene radical towards propargyl radical and further towards phenyl radical) for forming products where acetylene attachment could occur thus accelerating the HACA mechanism while these channels are not important for benzene.

The present research work developed and utilized the laser absorption spectroscopy of CO and provides highly accurate experimental data of CO concentration and temperature during the pyrolysis and oxidation of various hydrocarbon systems that are essential for the optimization of their combustion processes. In combination with the respective kinetics modeling studies, an improved understanding of the gas-phase kinetics of the investigated hydrocarbon systems was obtained.

7. List of own publications

Peer-reviewed publications:

1. F. Sen, B. Shu, T. Kasper, J. Herzler, O. Welz, M. Fikri, B. Atakan, C. Schulz, Shock-tube and plug-flow reactor study of the oxidation of fuel-rich CH_4/O_2 mixtures enhanced with additives, *Combust. Flame* 169 (2016) 307-320.
2. P. Sela, B. Shu, M. Aghsaee, J. Herzler, O. Welz, M. Fikri, C. Schulz, A single-pulse shock tube coupled with high-repetition-rate time-of-flight mass spectrometry and gas chromatography for high-temperature gas-phase kinetic studies, *Rev. Sci. Instrum.* 87 (2016) 105103
3. B. Shu, J. Herzler, S. Peukert, M. Fikri, C. Schulz, A shock tube and modeling study about anisole pyrolysis using time-resolved CO absorption measurements, *Int. J. Chem. Kinet*. 49 (2017) 656-667
4. D. Nativel, B. Shu, J. Herzler, M. Fikri, C. Schulz, Shock-tube study of methane pyrolysis in the context of energy-storage processes, *Proc*. *Combust*. *Inst*. 37, submitted
5. A. Drakon, B. Shu, A. Eremin, M. Fikri, C. Schulz, Soot formation in shock-wave-induced pyrolysis of acetylene and benzene with H_2, O_2, and CH_4 addition, *Proc*. *Combust*. *Inst*. 37, submitted

Conference contributions:

1. A. Drakon, B. Shu, A. Eremin, M. Fikri, C. Schulz, Influence of hydrogen, oxygen and methane additives on soot formations in shock wave pyrolysis of acetylene and bezene, 8th European Combustion Meeting, 18th – 21st April, 2017, Dubrovnik, Croatia, Poster.
2. M. Aghsasee, B. Shu, O. Welz, M. Fikri, C. Schulz, Experimental study of 3-pentanone pyrolysis and oxidation, 9th international Conference on Chemical Kinetics, 28th June – 2nd July, 2015, Ghent, Belgium, Talk.
3. P. Sela, M. Aghsaee, J. Birkmann, B. Shu, J. Herzler, M. Fikri, C. Schulz, O. Welz, A single-pulse shock tube coupled with high-repetition-rate time-of-flight mass spectrometry and gas chromatography for high-temperature kinetic studies, 9th international Conference on Chemical Kinetics, 28th June – 2nd July, 2015, Ghent, Belgium, Poster.
4. B. Shu, J. Herzler, O. Welz, M. Fikri, C. Schulz, Mid-IR quantum cascade laser absorption CO concentration measurements of fuel-rich CH_4/O_2-mixtures doped with dimethyl ether and *n*-heptane behind reflected shock waves, 7th European Combustion Meeting, 30th March – 2nd April, 2015, Budapest, Hungary, Poster
5. B. Shu, M. Aghsaee, M. Fikri, C. Schulz, Shock tube investigation of the decomposition of

cyclohexene at high temperature, 6th European Combustion Meeting, 25th – 28th June, 2013, Lund, Sweden, Poster

6. M. Aghsaee, B. Shu, M. Fikri, C. Schulz, A high-repetition-rate time-of-flight mass-spectrometry study of 3-pentanone pyrolysis and oxidation behind reflected shock waves, 6th European Combustion Meeting, 25th – 28th June, 2013, Lund, Sweden, Poster

8. Appendix

8.1. Temperature measurement using the CO absorption line pair P(8)/R(21) at *T* = 980–1710 K

Mixture: 0.5% CO/2% H_2/Ar

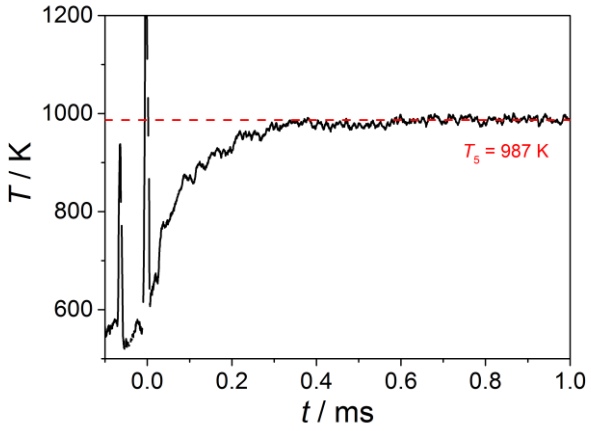

Figure A1: Temperature measurement with the CO absorption line pair P(8)/R(21) at 987 K and 0.81 bar.

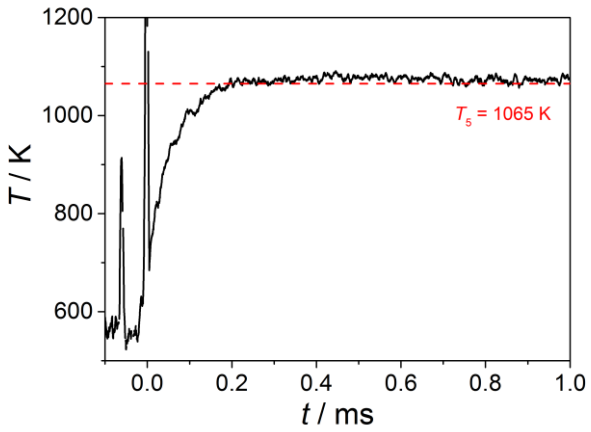

Figure A2: Temperature measurement with the CO absorption line pair P(8)/R(21) at 1065 K and 0.67 bar.

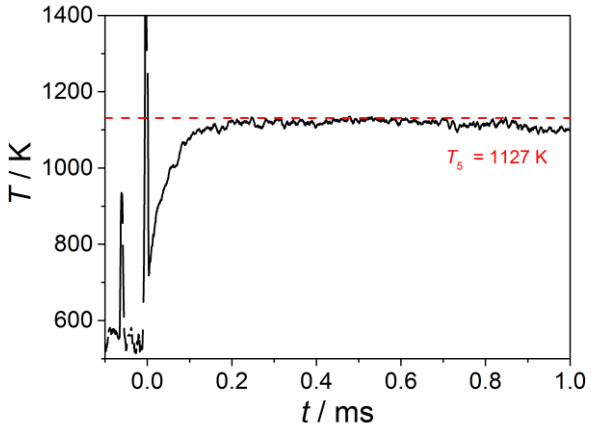

Figure A3: Temperature measurement with the CO absorption line pair P(8)/R(21) at 1127 K and 1.11 bar.

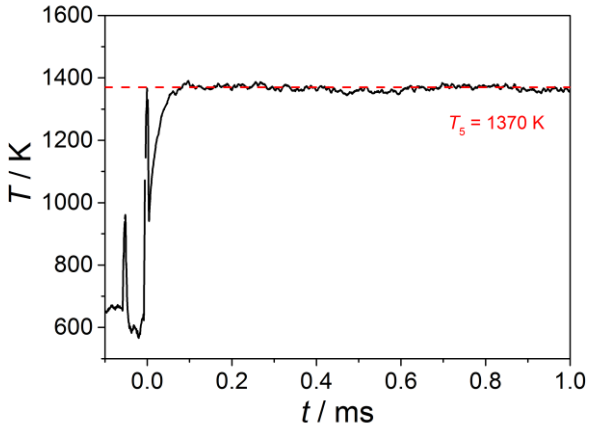

Figure A4: Temperature measurement with the CO absorption line pair P(8)/R(21) at 1370 K and 1.86 bar.

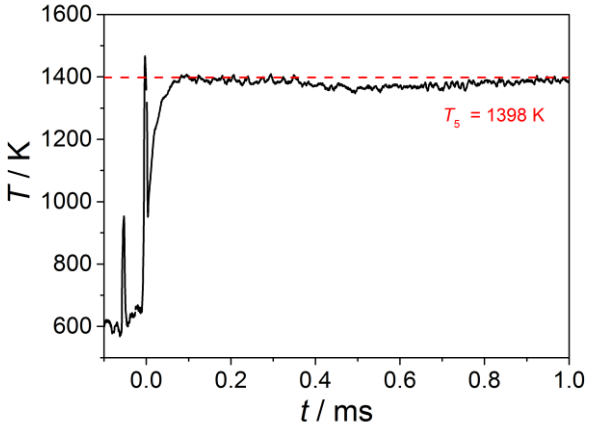

Figure A5: Temperature measurement with the CO absorption line pair P(8)/R(21) at 1398 K and 1.66 bar.

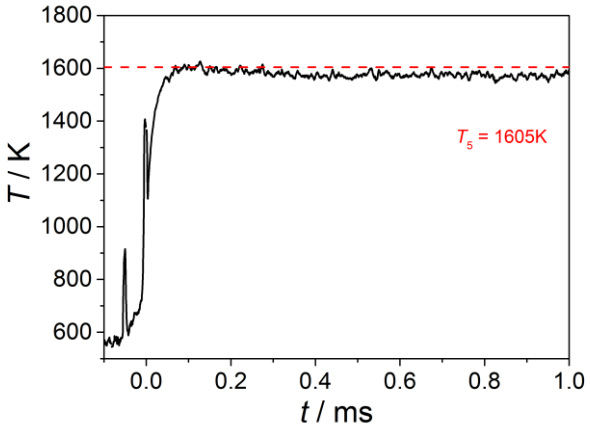

Figure A6: Temperature measurement with the CO absorption line pair P(8)/R(21) at 1605 K and 1.73 bar.

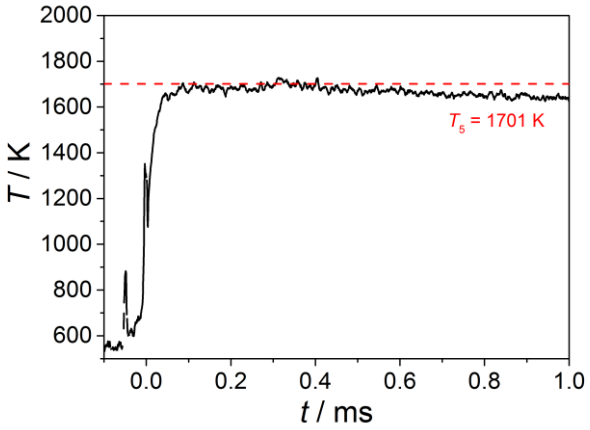

Figure A7: Temperature measurement with the CO absorption line pair P(8)/R(21) at 1701K and 1.64 bar.

8.2. Measured CO-concentration profiles for anisole decomposition

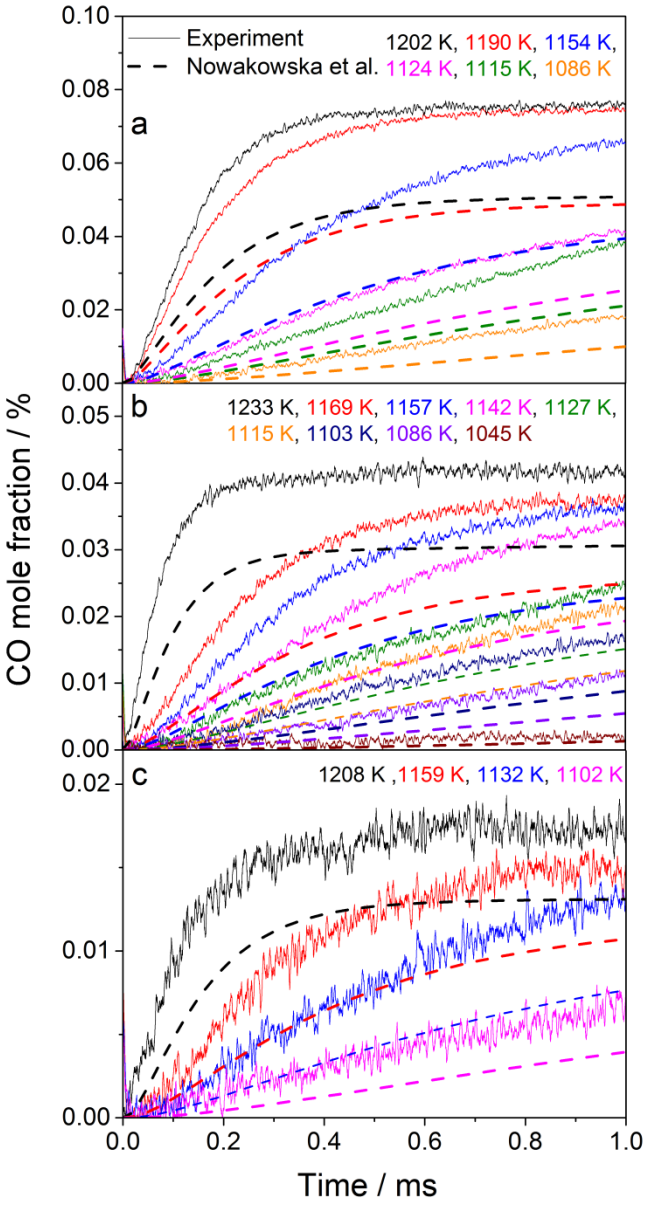

Figure A8: CO concentration–time histories during anisole pyrolysis in comparison of the simulation using the mechanism of Nowakowska et al. [102] at T = 1040–1240 K and $p \approx 1.3$ bar; mixture: (a) 1000 ppm ansisole/ Ar; (b) 500 ppm ansisole/ Ar (c) 200 ppm ansisole/ Ar.

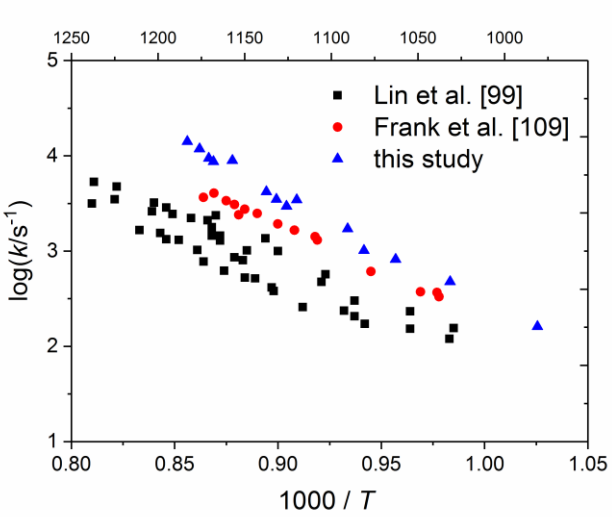

Figure A9: Comparison of experimental data sets (k of $C_6H_5O \rightarrow CO + C_5H_5$) of Lin and Lin [99], Frank et al. [109] and this study at temperature between 950 and 1250 K.

8.3. Phenoxy radical decomposition: Rate constants

Calculated pressure-dependent rate constants for phenoxy radical decomposition: $C_6H_5O \rightarrow CO + C_5H_5$ in the T-range 900–1600 K with Ar as bath gas.

p / bar	A / s^{-1}	n	(E_a/R) / K
0.01	1.106×10^{92}	–23.7533	43629
0.5	5.857×10^{89}	–22.4073	46256
1.0	1.781×10^{87}	–21.5651	46125
10.0	2.406×10^{71}	–16.6578	43201
100.0	6.547×10^{41}	–7.9577	35179
1000.0	2.742×10^{19}	–1.4598	28561

9. References

[1] B. Atakan, "Gas Turbines for Polygeneration? : A Thermodynamic Investigation of a Fuel Rich Gas Turbine Cycle", *Int. J. Thermodyn.* 14 (2011) 185-192.

[2] H. Li, A. Farooq, J. Jeffries, R. Hanson, "Near-infrared diode laser absorption sensor for rapid measurements of temperature and water vapor in a shock tube", *Appl. Phys. B* 89 (2007) 407-416.

[3] M. Frenklach, T. Yuan, M.K. Ramachandra, "Soot formation in binary hydrocarbon mixtures", *Energ. Fuel* 2 (1988) 462-480.

[4] A. Farooq, J.B. Jeffries, R.K. Hanson, "Sensitive detection of temperature behind reflected shock waves using wavelength modulation spectroscopy of CO_2 near 2.7 μm", *Appl. Phys. B* 96 (2009) 161-173.

[5] A.E. Klingbeil, J.B. Jeffries, R.K. Hanson, "Two-wavelength mid-IR diagnostic for temperature and n-dodecane concentration in an aerosol shock tube", *Appl. Phys. B* 93 (2008) 627-638.

[6] L.R. Cancino, M. Fikri, A.A.M. Oliveira, C. Schulz, "Ignition delay times of ethanol-containing multi-component gasoline surrogates: Shock-tube experiments and detailed modeling", *Fuel* 90 (2011) 1238-1244.

[7] M. Fikri, M. Bozkurt, H. Somnitz, C. Schulz, "High temperature shock-tube study of the reaction of gallium with ammonia", *Phy. Chem. Chem. Phys.* 13 (2011) 4149-4154.

[8] M. Fikri, J. Herzler, R. Starke, C. Schulz, P. Roth, G.T. Kalghatgi, "Autoignition of gasoline surrogates mixtures at intermediate temperatures and high pressures", *Combust. Flame* 152 (2008) 276-281.

[9] M. Aghsaee, D. Nativel, M. Bozkurt, M. Fikri, N. Chaumeix, C. Schulz, "Experimental study of the kinetics of ethanol pyrolysis and oxidation behind reflected shock waves and in laminar flames", *Proc. Combust. Inst.* 35 (2015) 393-400.

[10] A. Farooq, J.B. Jeffries, R.K. Hanson, "In situ combustion measurements of H_2O and temperature near 2.5 μm using tunable diode laser absorption", *Meas. Sci. Technol.* 19 (2008) 1-11.

[11] M. Aghsaee, S. Dürrstein, J. Herzler, H. Böhm, M. Fikri, C. Schulz, "Influence of molecular hydrogen on acetylene pyrolysis: Experiment and modeling", *Combust. Flame* 161 (2014) 2263-2269.

[12] P. Sela, B. Shu, M. Aghsaee, J. Herzler, O. Welz, M. Fikir, C. Schulz, "A single-pulse shock tube coupled with high-repetition-rate time-of-flight mass spectrometry and gas

chromatography for high-temperature gas-phase kinetics studies", *Rew. Sci. Instrum.* 87 (2016) 105103.

[13] M.G. Allen, "Diode laser absorption sensors for gas-dynamic and combustion flows", *Meas. Sci. Technol.* 9 (1998) 545-562.

[14] H. Teichert, T. Fernholz, V. Ebert, "Simultaneous in situ measurement of CO, H_2O, and gas temperatures in a full-sized coal-fired power plant by near-infrared diode lasers", *Appl. Opt.* 42 (2003) 2043-2051.

[15] K. Kohse-Höinghaus, R.S. Barlow, M. Aldén, J. Wolfrum, "Combustion at the focus: laser diagnostics and control", *Proc. Combust. Inst.* 30 (2005) 89-123.

[16] G.B. Rieker, H. Li, X. Liu, J.T.C. Liu, J.B. Jeffries, R.K. Hanson, M.G. Allen, S.D. Wehe, P.A. Mulhall, H.S. Kindle, K.R. Kakuho, K.R. Sholes, T. Mastsuura, S. Takatani, "Rapid measurements of temperature and H_2O concentration in IC engines with a spark plug-mounted diode laser sensor", *Proc. Combust. Inst.* 31 (2007) 3041-3049.

[17] X. Liu, J.B. Jeffries, R.K. Hanson, K.M. Hinckley, M.A. Woodmansee, "Development of a tunable diode laser sensor for measurements of gas turbine exhaust temperature", *Appl. Phys. B* 82 (2006) 469-478.

[18] D.T. Cassidy, L.J. Bonnell, "Trace gas detection with short-external-cavity InGaAsP diode laser transmitter modules operating at 1.58 μm" *Appl. Opt.* 27 (1988) 2688-2693.

[19] D.M. Sonnenfroh, M.G. Allen, "Observation of CO and CO_2 absorption near 1.57 μm with an external-cavity diode laser", *Appl. Opt.* 36 (1997) 3298-3300.

[20] A. Farooq, J.B. Jeffries, R.K. Hanson, "CO_2 concentration and temperature sensor for combustion gases using diode-laser absorption near 2.7 μm", *Appl. Phys. B* 90 (2008) 619-628.

[21] J. Wang, M. Maiorov, J.B. Jeffries, D.Z. Garbuzov, J.C. Connolly, R.K. Hanson, "A Potential Remot Sensor of CO in Vehicle Exhausts using 2.3 μm Diode Lasers", *Meas. Sci. Technol.* 11 (2000) 1576-1584.

[22] A. Kosterev, G. Wysocki, Y. Bakhirkin, S. So, R. Lewicki, M. Fraser, F. Tittel, R.F. Curl, "Application of quantum cascade lasers to trace gas analysis", *Appl. Phys. B* 90 (2008) 165-176.

[23] R.F. Curl, F. Capasso, C. Gmachl, A.A. Kosterev, B. McManus, R. Lewicki, M. Pusharsky, G. Wysocki, F.K. Tittel, *Chem. Phys. Lett.* 487 (2010) 1-18.

[24] W. Ren, A. Farooq, D.F. Davidson, R.K. Hanson, "CO concentration and temperature sensor for combustion gases using quantum-cascade laser absorption near 4.7 μm", *Appl. Phys. B* 107 (2012) 849-860.

[25] W. Ren, K.-Y. Lam, D.F. Davidson, R.K. Hanson, "Pyrolysis and oxidation of methyl acetate in a shock tube: A multi-species time-history study", *Proc. Combust. Inst.* 36 (2017) 255-264.

[26] K. Sun, S. Wang, R. Sur, X. Chao, J.B. Jeffries, R.K. Hanson, "Sensitive and rapid laser diagnostic for shock tube kinetics studies using cavity-enhanced absorption spectroscopy", *Opt. Express* 20 (2014) 24559-24565.

[27] J. Jortner, "Temperature dependent activation energy for electron transfer between biological molecules", *J. Chem. Phys.* 64 (1976) 4860-4867.

[28] O. Levenspiel, *Chemical Reacion Engineering*, John Wiley & Son, New York, 1999.

[29] F.A. Lindemann, "Discussion on "the radiation theory of chemical action"", *Trans. Faraday Soc.* 17 (1922) 598-606.

[30] M. Quack, J. Troe, "Specific Rate Constants of Unimolecular Processes II. Adiabatic Channel Model", *Ber. Bunsenges. Phys. Chem.* 78 (1974) 240-252.

[31] S.K. Upadhyay, *Chemical Kinetics and Reaction Dynamics*, Springer, New York, 2006.

[32] J. Warnatz, U. Maas, R.W. Dibble, *Verbrennung*, Springer, Heidelberg, 2001.

[33] O.K. Rice, H.C. Ramsperger, "Theories of Unimolecular Gas Reactions at low Pressure", *J. Am. Chem. Soc.* 49 (1927) 1617-1629.

[34] L.S. Kassel, "Studies in Homogeneous Gas Reactions I", *J. Phys. Chem.* 32 (1928) 225-242.

[35] H. Eyring, "The Activated Complex in Chemical Reactions", *J. Chem. Kinet.* 3 (1935) 107-115.

[36] Kintech Lab, Chemical Workbench 4.1, http://www.kintechlab.com.

[37] P. Vieille, "Sur les discontinuités produites par la détente brusque de gaz comprimés", *Comptes Rendus de l'Academie des Sciences de Paris* 129 (1899) 1228-1230.

[38] R.M. Spearrin, C.S. Goldenstein, I.A. Schultz, J.B. Jeffries, R.K. Hanson, "Simultaneous sensing of temperature, CO, and CO_2 in a scramjet combustor using quantum cascade laser absorption spectroscopy", *Appl. Phys. B* 117 (2014) 689-698.

[39] A. Ben-Yakar, M.G. Mungal, R.K. Hanson, "Time evolution and mixing characteristics of hydrogen and ethylene transverse jets in supersonic crossflows", *Phy. Fluids* 18 (2006) 1-16.

[40] E. Rathakrishnan, *Applied Gas Dynamics*, John Wiley & Son, Singapore, 2010.

[41] A. Gaydon, I.R. Hurle, *The shock tube in high-temperature chemical physics*, Chapman and Hall Ltd,, London, 1969.

[42] W.J.M. Rankine, "XV. On the thermodynamic theory of waves of finite longitudinal disturbance", *Phil. Trans. R. Soc. Lond.* 160 (1870) 277-288.

[43] P.H. Hugoniot, "Memoire sur la propagation du mouvement dans les corps et spécialement dans les gaz parfaits, 2e Patie", *J. Ecole Polytech.* 57 (1887) 3-97.

[44] T. Dreier, C. Schulz, "Laser-based diagnostics in the gas-phase synthesis of inorganic nanoparticles", *Powd. Technol.* 287 (2016) 226-238.

[45] R. Pan, K.J. Daun, T. Dreier, C. Schulz, "Uncertainty quantification and design-of-experiment in absorption-based aqueous film parameter measurements using Bayesian inference", *Appl. Opt.* 56 (2017) E1-E7.

[46] R.K. Hanson, *Introduction of Spectroscopic Diagnostics for Gases*, Stanford University, Stanford, USA, 2011.

[47] P. Aktins, J.D. Paula, *Physical Chemistry*, Oxford University Press Inc., New York, 2002.

[48] HITRAN Online, http://www.caf.harvard.edu/HITRAN/.

[49] R.R. Gamache, S. Kennedy, R. Hawkins, L.S. Rothman, "Total internal partition sums of molecules in the terrestrial atmosphere", *J. Mol. Struc.* 517-518 (2000) 407-425.

[50] A.N.K. Reddy, D.K. Sagar, "Half-Width at half-maximum, full-Width at half-maximum analysis for resolution of asymmetrically apodised optical systems with slit apertures", *J. Phys.* 84 (2015) 117-126.

[51] P.M. Sinclair, P. Duggan, R. Berman, J.R. Drummond, A.D. May, "Line broadening in the fundamental band of CO in CO-He and CO-Ar mixtures", *J. Mol. Spectrosc.* 191 (1998) 258-264.

[52] W. Heisenberg, "Über den anschaulichen Inhalt der quantentheoretischen Kinematik und Mechanik", *Z. Physik* 43 (1927) 172-198.

[53] W.Demtröder, *Laser Spectroscopy: Basic Concepts and Instrumentation*, Springer, Berlin, 1996.

[54] R.S.M. Chrysite, E.F. Nasir, A. Farooq, "Ultra-fast and calibration-free temperature sensing in the intrapulse mode", *Opt. Lett.* 39 (2014) 6620-6623.

[55] H. Sakurai, N. Kawahara, M. Itou, E. Tomita, K. Suzuki, Y. Skurai, "Densitometry and temperature measurement of combustion gas by X-ray Compton scattering", *J. Synchrotron Radiat.* 23 (2016) 617-621.

[56] C. Gessenhardt, C. Schulz, S. Kaiser, "Endoscopic temperature imaging in a four-cylinder IC engine via two-color toluene fluorescence", *Proc. Combust. Inst.* 35 (2015) 3697-3705.

[57] H. Yang, D. Greszik, I. Wolkas, T. Dreier, C. Schulz, "Tunable diode laser absorption sensor for the simultaneous measurement of water film thickness, liquid-and vapor-phase temperature", *Appl. Phys. B* 104 (2011) 21-27.

[58] M.F. Heidmann, "A Modified Sodium-Line Reversal Technique for the Measurement of Combustion Temperatures in Rocket Engines", *J. Am. Rock. Soci.* 23 (1953) 248-253.

[59] R. Devillers, G. Bruneaux, C. Schulz, "Development of a two-line OH-laser-induced fluorescence thermometry diagnostics strategy for gas-phase temperature measurements in engines", *Appl. Opt.* 47 (2008) 5871-5885.

[60] J.T.C. Liu, J.B. Jeffries, R.K. Hanson, "Wavelength modulation absorption spectroscopy with 2*f* detection using multiplexed diode lasers for rapid temperature measurements in gaseous flows", *Appl. Phys. B* 78 (2004) 503-511.

[61] X. Zhou, X. Liu, J.B. Jeffries, R.K. Hanson, "Development of a sensor for temperature and water concentration in combustion gases using a single tunable diode laser", *Meas. Sci. Technol.* 14 (2003) 1459-1468.

[62] L.S. Rothman, I.E. Gordon, A. Barbe, D.C. Benner, P.F. Bernath, M. Birk, V. Boudon, L.R. Brown, A. Campargue, J.-P. Champion, K. Chance, L.H. Coudert, V. Dana, V.M. Devi, S. Fally, J.-M. Flaud, R.R. Gamache, A. Goldman, D. Jacquemart, I. Kleiner, N. Lacome, W.J. Lafferty, O.V. Naumenko, A.V. Nikitin, J. Orphal, V.I. Perevalov, A. Perrin, A. Predoi-Cross, C.P. Rinsland, M. Rotger, M. Simeckova, M.A.H. Smith, K. Sung, S.A. Tashkun, J. Tennyson, R.A. Toth, A.C. Vandaele, J.V. Auwera, "HITRAN 2008 database", *J. Quant. Spectrosc. Radiat. Transfer* 110 (2009) 553-572.

[63] R.M. Mihalcea, D.S. Baer, R.K. Hanson, "Diode laser sensor for measurements of CO, CO_2, and CH_4 in combustion flows", *Appl. Opt.* 36 (1997) 8745-8752.

[64] F. Capasso, R. Paiella, R. Martini, R. Colombelli, C. Gmachl, T.L. Myers, M.S. Taubman, R.M. Williams, C.G. Bethea, K. Unterrainer, H.Y. Hwang, D.L. Sivco, A.Y. Cho, A.M. Sergent, H.C. Liu, E.A. Whittaker, "Quantum cascade lasers: ultrahigh-speed operation, optical wireless communication, narrow linewidth, and far-infrared emission", *IEEE J. Quantum Electron.* 38 (2002) 511-532.

[65] L.S. Rothman, I.E. Gordon, Y. Babikov, A. Barbe, D.C. Benner, P.F. Bernath, M. Birk, L. Bizzocchi, V. Boudon, L.R. Brown, A. Campargue, K. Chance, E.A. Cohen, L.H. Couder, V.M. Devi, B.J. Drouin, A. Fayt, J.-M. Flaud, R.R. Gamache, J.J. Harrison, J.-M. Hartmann, C. Hill, J.T. Hodges, D. Jacquemart, A. Jolly, J. Lamouroux, R.J.L. Roy, G. Li, D.A. Long, O.M. Lyulin, C.J. Mackie, S.T. Massie, S. Mikhailenko, H.S.P. Müller, O.V. Naumenko, A.V. Nikitin, J. Orphal, V. Perevalov, A. Perrin, E.R. Polovtseva, C. Richard, M.A.H. Smith, E. Starikova, K. Sung, S. Tashkun, J. Tennyson, G.C. Toon, V.G. Tyuterev, G. Wagner, "The HITRAN2012 molecular spectroscopic database", *J. Quant. Spectrosc. Radiat. Transfer* 130 (2013) 4-50.

[66] L.R. Rothman, I.E. Gordon, R.J. Barber, H. Dothe, R.R. Gamache, A. Goldman, V. Perevalov, S.A. Tashkun, J. Tennyson, "HITEMP, the high-temperature molecular spectroscopic database", *J. Quant. Spectrosc. Radiat. Transfer* 111 (2010) 2139-2150.

[67] L.S. Rothman, D. Jacquemart, A. Barbe, D.C. Benner, M. Birk, L.R. Brown, M.R. Carleer, K.C. C. C. Jr., L.H. Coudert, V. Dana, V.M. Devi, J.-M. Flaud, R.R. Gamache, A. Goldman, J.-M. Hartmann, K.W. Jucks, A.G. Maki, J.-Y. Mandin, S.T. Massie, J. Orphal, A. Perrin, C.P. Rinsland, M.A.H. Smith, J. Tennyson, R.N. Tolchenov, R.A. Toth, J.V. Auwera, P. Varanasi, G. Wagner, "The HITRAN 2004 molecular spectrocopic database", *J. Quant. Spectrosc. Radiat. Transfer* 96 (2005) 139-204.

[68] R.C. Millikan, J.D.R. White, "Systematics of vibrational relaxation", *Chem. Phys.* 39 (1963) 3209-3213.

[69] J.U. White, "Very long optical paths in air", *J. Opt. Soc. Am.* 66 (1976) 411-416.

[70] V. Modica, C. Morin, P. Guibert, "3-Pentanone LIF at elevated temperatures and pressures: measurements and modeling", *Appl. Phys. B* 87 (2007) 193-204.

[71] K.-Y. Lam, W. Ren, Z. Hong, D.F. Davidson, R.K. Hanson, "Shock tube measurements of 3-pentanone pyrolysis and oxidation", *Combust. Flame* 11 (2012) 3251-3263.

[72] E.E. Dames, K.Y. Lam, D.F. Davidson, R.K. Hanson, "An improved kinetic mechanism for 3-pentanone pyrolysis and oxidation developed using multispecies time histories in shock-tubes", *Combust. Flame* 161 (2014) 1135-1145.

[73] Z. Serinyel, N. Chaumeix, G. Black, J.M. Simmie, H.J. Curran, "Experimental and chemical kinetic modeling study of 3-Pentanone oxidation", *J. Phys. Chem. A* 114 (2010) 12176-12186.

[74] H. Gossler, O. Deutschmann, "Numerical optimization and reaction flow analysis of syngas production via partial oxidation of natural gas in internal combustion engines", *Int. J. Hydrog. Energy* 40 (2015) 11046-11058.

[75] S. Jahangirian, S. Dooley, F.M. Haas, F.L. Dryer, "A detailed experimental and kinetic modeling study of n-decane oxidation at elevated pressures", *Combust. Flame* 159 (2012) 30-43.

[76] C.L. Rasmussen, P. Glarborg, "Direct partial oxidation of natural gas to liquid chemicals: chemical kinetic modeling and global optimization", *Ind. Eng. Chem. Res.*, (2008) 6579-6588.

[77] S. Gersen, A.V. Mokhov, J.H. Darmeveil, H.B. Levinsky, P. Glarborg, "Ignition-promoting effect of NO_2 on methane, ethane, and methane/ethane mixtures in a rapid compression machine", *Proc. Combust. Inst.* 33 (2011) 433-440.

[78] P. Glarborg, L.L.B. Bentzen, "Chemical effects of a high CO_2 concentration in oxy-fuel combustion of methane", *Energy Fuels* 22 (2008) 291-296.

[79] C.L. Rasmussen, J.G. Jakobsen, P. Glarborg, "Experimental measurements and kinetic modeling of CH_4/O_2 and $CH_4/C_2H_6/O_2$ conversion at high pressure", *Int. J. Chem. Kinet.* 40 (2008) 778-807.

[80] D.W. Rytz, A. Baiker, "Partial oxidation of methane to methanol in a flow reactor at elevated pressure", *Ind. Eng. Chem. Res.* 30 (1991) 2287-2292.

[81] C.L. Rasmussen, J. Hansen, P. Marshall, P. Glarborg, "Experimental measurements and kinetic modeling of $CO/H_2/O_2/NO_x$ conversion at high pressure", *Int. J. Chem. Kinet.* 40 (2008) 4554-4480.

[82] S. Sato, D. Yamshita, N. Lida, "Influence of the fuel compositions on the homogeneous charge compression ignition combustion", *Int. J. Engine Res.* 9 (2008) 123-148.

[83] J. Herzler, M. Fikri, O. Welz, C. Schulz, "High-pressure shock-tube study of the ignition of fuel-rich CH_4/air and CH_4/additive/air mixtures over a wide temperature range", *7th European Combustion Meeting, ECM 2015*, Budapest, Ungarn, 2015.

[84] F. Sen, B. Shu, T. Kasper, J. Herzler, O. Welz, M. Fikri, B. Atakan, C. Schulz, "Shock-tube and plug-flow reactor study of the oxidation of fuel-rich CH_4/O_2 mixtures enhanced with additives", *Combust. Flame* 169 (2016) 307-320.

[85] K. Yasunaga, J.M. Simmie, H.J. Curran, T. Koike, O. Takahashi, Y. Kuraguchi, Y. Hidaka, "Detailed chemical kinetic mechanisms of ethyl methyl, methyl *tert*-butyl and ethyl *tert*-butyl ethers: The importance of uni-molecular elimination reactions", *Combust. Flame* 158 (2011) 1032-1036.

[86] U. Burke, K.P. Sommer, P. O'Toole, C.M. Zinner, N. Marquet, G. Bourque, E.L. Petersen, W.K. Metcalfe, Z. Serinyel, H.J. Curran, "An ignition delay and kinetic modeling study of methane, dimethyl ether, and their mixtures at high pressures", *Combust. Flame* 162 (2015) 315-330.

[87] Z. Zhao, M. Chaos, A. Kazakov, F.L. Dryer, "Thermal decomposition reaction and a comprehensive kinetic model of dimethyl ether", *Int. J. Chem. Kinet.* 40 (2008) 1-18.

[88] K. Yasunaga, F. Gillespie, J.M. Simmie, H.J. Curran, Y. Kuraguchhi, H. Hoshikawa, M. Yamane, Y. Hidaka, "A multiple shock tube and chemical kinetic modeling study of diethyl ether pyrolysis and oxidation", *J. Phys. Chem. A* 114 (2010) 9098-9109.

[89] S.L. Fischer, F.L. Dryer, H.J. Curran, "The reaction kinetics of dimethyl ether. I: High-temperature pyrolysis and oxidation in flow reactors", *Int. J. Chem. Kinet.* 32 (2000) 713-740.

[90] M. Mehl, W.J. Pitz, C.K. Westbrook, H.J. Curran, "Kinetic Modeling of Gasoline Surrogate Components and Mixtures Under Engine Conditions", *Proc. Combust. Inst.* 22 (2011) 193-200.

[91] M. Mehl, T. Faravelli, E. Ranzi, D. Miller, N. Cernansky, "Experimental and kinetic modeling study of the effect of fuel composition in HCCI engines", *Proc. Combust. Inst.* 32 (2009) 2843-2850.

[92] T. Fleisch, C. McCarthy, A. Basu, C. Udovich, P. Charbonneau, W. Slodowske, S.-E. Mikkelsen, J. McCandless, " A new clean diesel technology: Demonstration of ULEV emissions on a Navistar diesel engine fueled with dimethyl ether", *SAE Trans.* 104 (1995) 42-53.

[93] C.J. Green, N.A. Cockshutt, L. King, "Dimethyl ether as a methanol ignition improver: substitution requirements and exhaust emissions impact", *SAE Technical Paper Series 902155*, (1990).

[94] M.E. Karpuk, J.D. Wright, J.L. Dippo, D.E. Jantzen, "Dimethyl ether as an ignition enhancer for methanol-fueled diesel engines", *SAE Technical Paper Series 912420*, (1991).

[95] T. Hirasawa, T. Kaneba, Y. Kamata, K. Muraoka, Y. Nakamura, "Temperature dependence of intensities of laser-induced fluorescences of ethylbenzene and naphthalene seeded in gas flow at atmospheric pressure", *J. Vis.* 10 (2007) 197-206.

[96] S. Faust, T. Dreier, C. Schulz, "Photo-physical properties of anisole: temperature, pressure, and bath gas composition dependence of fluorescence spectra and lifetimes", *Appl. Phys. B* 112 (2013) 751-759.

[97] S. Zabeti, M. Aghsaee, M. Fikri, O. Welz, C. Schulz, "Optica properties and pyrolysis of shock-heated gas-phase anisole", *Proc. Combust. Inst.*, (2016).

[98] N. Pasquier, B. Lecordier, M. Trinite, A. Cessou, "An experimental investigation of flame propagation through a turbulent stratified mixture", *Proc. Combust. Inst.* 31 (2007) 1567-1574.

[99] C.-Y. Lin, M.C. Lin, "Thermal decomposition of methyl phenyl ether in shock waves: the kinetics of phenoxy reactions", *J. Phys. Chem.* 90 (1986) 425-431.

[100] J.C. Mackie, K.R. Doolan, P.F. Nelson, "Kinetics of the thermal decomposition of methoxybenzene (anisole)", *J. Phys. Chem.* 93 (1989) 664-670.

[101] M. Nowakowska, O. Herbinet, A. Dufour, P.-A. Glaude, "Detailed kinetic study of anisole pyrolysis and oxidation to understand tar formation during biomass combustion and gasification", *Combust. Flame* 161 (2014) 1474-1488.

[102] C. Muller, V. Michel, G. Scacchi, G.M. Come, "THERGAS: a computer program for the evaluation of thermochemical data of molecules and free radicals in the gas phase", *J. Chim. Phys.* 92 (1995) 1154 - 1178.

[103] A.V. Friderichsen, E.-J. Shin, R.J. Evans, M.R. Nimlos, D.C. Dayton, G.B. Ellison, "The pyrolysis of anisole ($C_6H_5OCH_3$) using a hyperthermal nozzle", *Fuel* 80 (2001) 1747-1755.

[104] S. Paul, M.H. Back, A kinetic determination of the dissociation energz of the C–O Bond in anisole, *Can. J. Chem.* 53 (1975) 3330.

[105] M.M. Suryan, S.A. Kafafi, S.E. Stein, "The thermal decomposition of hydroxy- and methoxy-substituted anisoles", *J. Am. Chem. Soc.* 111 (1989) 1423-1429.

[106] I.W.C.E. Arends, R. Louw, P. Mulder, "Kinetic study of the thermolysis of anisole in a hydrogen atmosphere", *J. Phys. Chem.* 97 (1993) 7914-7925.

[107] A.M. Scheer, C. Mukarakate, D.J. Robichaud, G.B. Ellison, M.R. Nimlos, "Radical chemistry in the thermal decomposition of anisole and deuterated anisoles: an investigation of aromatic growth", *J. Phys. Chem. A* 114 (2010) 9043-9056.

[108] A.J. Colussi, F. Zabel, S.W. Benson, "The very low-pressure pyrolysis of phenyl ethyl ether, phenyl allyl ether, and benzyl methyl ether and the enthalpy of formation of the phenoxy radical", *Int. J. Chem. Kinet.* 9 (1977) 161-178.

[109] P. Frank, J. Herzler, T. Just, C. Wahl, "High-temperature reactions of phenyl oxidation", *Proc. Combust. Inst.* 25 (1994) 833-840.

[110] S. Olivella, A. Sol, A. Garcia-Raso, "*Ab initio* calculation of the potential surface for the thermal decomposition of the phenoxy radical", *J. Phys. Chem.* 99 (1995) 10549-10556.

[111] R. Liu, K. Morokuma, A.M. Mebel, M.C. Lin, "*Ab initio* study of the mechanism for the thermal decomposition of the phenoxy radical", *J. Phys. Chem.* 100 (1996) 9314-9322.

[112] H.-H. Carstensen, A.M. Dean, "A quantitative kinetic analysis of CO elimination from phenoxy radicals", *Int. J. Chem. Kinet.* 44 (2012) 75-89.

[113] Y.Z. He, W.G. Mallard, W. Tsang, "Kinetics of hydrogen and hydroxyl radical attack on phenol at high temperatures", *J. Phys. Chem.* 92 (1988) 2196-2201.

[114] M. Pecullan, K. Brezinsky, I. Glassman, "Pyrolysis and oxidation of anisole near 1000 K", *J. Phys. Chem. A* 101 (1997) 3305-3316.

[115] M.J. Frisch, G.W. Trucks, H.B. Schlegel, G. E.Scuseria, M. A.Robb, J.R. Cheeseman, G. Scalmani, V. Barone, B. Mennucci, G.A. Petersson, H. Nakatsuji, M. Caricato, X. Li, H.P. Hratchian, A.F. Izmaylov, J. Bloino, G. Zheng, J.L. Sonnenberg, M. Hada, M. Ehara, K. Toyota, R. Fukuda, J. Hasegawa, M. Ishida, T. Nakajima, Y. Honda, O. Kitao, H.Nakai, T. Vreven, J.A.J. Montgomery, J.E. Peralta, F. Ogliaro, M. Bearpark, J.J. Heyd, E. Brothers, K.N. Kudin,

V.N. Staroverov, R. Kobayashi, J. Normand, K. Raghavachari, A. Rendell, J.C. Burant, S.S. Iyengar, J. Tomasi, M. Cossi, N. Rega, J.M. Millam, M. Klene, J. Knox, J.B. Cross, V. Bakken, C. Adamo, J. Jaramillo, R. Gomperts, R.E. Stratmann, O. Yazyev, A.J. Austin, R. Cammi, C. Pomelli, J.W. Ochterski, R.L. Martin, K. Morokuma, V.G. Zakrzewski, G.A. Voth, P. Salvador, J.J. Dannenberg, S. Dapprich, A.D. Daniels, O. Farkas, J.B. Foresman, J.V. Ortiz, J. J. Cioslowski, D.J. Fox, *Gaussian 09, Revision A.02*, Gaussian Inc, Wallingford, CT, 2009.

[116] R.G. Gilbert, S.C. Smith, M.J.T. Jordan, G.P. Knight, *Unimol program suite (calculation of fall-off curves for unimolecular and recombination reactions)*, School of Chemistry, Sydney University, Australia, 1994.

[117] J.R. Barker, T.L. Nguyen, J.F. Stanton, C. Aieta, M. Ceotto, F. Gabas, T.J.D. Kumar, C.G.L. Li, L.L. Lohr, A. Maranzana, N.F. Ortiz, J.M. Preses, P.J. Stimac, *Multiwell-2016 Software Suite*, University of Michigan, Michigan, USA, 2016.

[118] B. Shu, J. Herzler, S. Peukert, M. Fikri, C. Schulz, "A shock tube and modeling study about anisole pyrolysis using time-resolved CO absorption measurements", *Int. J. Chem. Kinet.* 49 (2017) 656-667.

[119] C.Y. Lin, J.L. Hodgson, M. Namzian, M.L. Coote, "Comparison of G3 and G4 theories for radical addition and abstraction reactions", *J. Phys. Chem.* 113 (2009) 3690-3697.

[120] R.K. Robinson, R.P. Lindstedt, "On the chemical kinetics of cyclopentadiene oxidation", *Combust. Flame* 158 (2011) 666-686.

[121] R.K. Robinson, R.P. Lindstedt, "A comparative *ab initio* study of hydrogen abstraction from n-propyl benzene", *Combust. Flame* 160 (2013) 2642-2653.

[122] J.M. Simmie, J.N. Sheahan, "Validation of a database of formation enthalpies and of mid-level model chemistries", *J. Phys. Chem. A* 120 (2016) 7370 - 7384.

[123] B. Sirjean, R. Fournet, P.-A. Glaude, F. battin-Leclerc, W. Wang, M.A. Oehlschlaeger, "Shock tube and chemical kinetic modeling study of the oxidation of 2,5-dimethylfuran", *J. Phys. Chem.* 92 (2013) 1371-1392.

[124] M.P. Ruiz, A. Callejas, A. Millera, M.U. Alzueta, R. Bilbao, "Soot formation from C_2H_2 and C_2H_4 pyrolysis at different temperatures", *J. Anal. Appl. Pyrolysis* 79 (2007) 244-251.

[125] H. Richter, J.B. Howard, "Formation of polycyclic aromatic hydrocarbons and their growth to soot—a review of chemical reaction pathways", *Prog. Energy Combust. Sci.* 26 (2000) 565-608.

[126] A. Eremin, "Formation of carbon nanoparticles from the gas phase in shock wave pyrolysis processes", *Prog. Energy Combust. Sci.* 38 (2012) 1-40.

[127] H. Wang, "Formation of nascent soot and other condensed-phase materials in flames", *Proc. Combust. Inst.* 33 (2011) 41-67.

[128] M. Frenklach, H. Wang, "Detailed modeling of soot particle nucleation and growth", *Proc. Combust. Inst.* 23 (1991) 1559-1566.

[129] A. Emelianov, A. Eremin, H. Jander, H.G. Wagner, "Carbon condensation wave in C_3O_2 and C_2H_2 initiated by a shock wave", *Proc. Combust. Inst.* 33 (2011) 525-532.

[130] H. Böhm, D. Hesse, H. Jander, B. Lüers, J. Pietscher, H.G. Wagner, M. Weiss, "The influence of pressure and temperature on soot formation in premixed flames", *Proc. Combust. Inst.* 22 (1989) 403-411.

[131] D.E. Fussey, A.J. Gosling, D. Lampard, "A shock-tube study of induction times in the formation of carbon particles by pyrolysis of the C_2", *Combust. Flame* 32 (1978) 181-192.

[132] A. Eremin, E. Gurentsov, E. Mikheyeva, "Experimental study of molecular hydrogen influence on carbon particle growth in acetylene pyrolysis behind shock waves", *Combust. Flame* 159 (2012) 3606-3615.

[133] H. Wang, L. Laskin, *Comprehensive kinetic model of ethylene and acetylene oxidation at high temperature*, http://ignis.usc.edu/Mechanisms/C2-C4/c2.pdf.

[134] R.J. Kee, F.M. Rupley, J.A. Miller, *Chemkin tutorials manual*, in: R. Design (Ed.), San Diego, CA, 2009.

[135] A. Drakon, A. Eremin, N. Matveeva, E. Mikheyeva, "The opposite influences of flame suppressants on the ignition of combustible mixtures behind shock waves", *Combust. Flame* 176 (2017) 592-598.

[136] A. Eremin, E. Gurentsov, E. Mikheyeva, "Experimental study of temperature influence on carbon particle formation in shock wave pyrolysis of bezene and benzene-ethanol mixtures", *Combust. Flame* 162 (2015) 207-215.

[137] A. Farooq, J.B. Jeffries, R.K. Hanson, "Measurements of CO_2 concentration and temperature at high pressures using 1*f*-normalized wavelength modulation spectroscopy with second harmonic detection near 2.7 μm", *Appl. Opt.* 48 (2009) 6740-6753.

[138] H. Li, G.B. Richer, X. Liu, J.B. Jeffries, R.K. Hanson, "Extension of wavelength-modulation spectroscopy to large modulation depth for diode laser absorption measurements in high-pressure gases", *Appl. Opt.* 45 (2006) 1052-1061.

[139] L.C. Philippe, R.K. Hanson, "Laser diode wavelength-modulation spectroscopy for simultaneous measurement of temperature, pressure, and velocity in shock-heated oxygen flows ", *Appl. Opt.* 32 (1993) 6090-6103.

[140] J.J. Girard, R.M. Spearrin, C.S. Goldenstein, R.K. Hanson, "Compact optical probe for flame temperature and carbon dioxide using interband cascade laser absorption near 4.2 μm", *Combust. Flame* 178 (2017) 158-167.

[141] A.E. Klingbeil, J.B. Jeffries, R.K. Hanson, "Temperature- and pressure-dependent absorption cross sections of gaseous hydrocarbons at 3.39 μm", *Meas. Sci. Technol.* 17 (2006) 1950-1957.

[142] W. Ren, E. Dames, D. Hyland, D.F. Davidson, R.K. Hanson, "Shock tube study of methanol, methyl formate pyrolysis: CH_3OH and CO time-history measurements", *Combust. Flame* 160 (2013) 2669-2679.

[143] X. Chao, J.B. Jeffries, R.K. Hanson, "Wavelength-modulation spectroscopy for real-time, *in situ* NO detection in combustion gases with a 5.2 μm quantum cascade laser", *Appl. Phys. B* 106 (2012) 987-997.